Investigation Of Baryons With Strangeness And Search For Weakly Decaying Exotics With ALICE At The LHC

Vom Fachbereich Physik
der Technischen Universität Darmstadt

zur Erlangung des Grades
eines Doktors der Naturwissenschaften
(Dr. rer. nat.)

genehmigte Dissertation von

Dipl.-Phys. Benjamin Dönigus

aus Groß-Umstadt

Darmstadt 2013
D17

Referent:	Prof. Dr. P. Braun-Munzinger
Korreferent:	Prof. Dr. J. Wambach

Tag der Einreichung:	23. Januar 2013
Tag der Prüfung:	06. Mai 2013

Im Gedenken an meinen Vater

Deine Wissenschaft sei Menschlich!

David Hume, Eine Untersuchung über den menschlichen Verstand

Es führt zu nichts, die Ersten Prinzipen "durchschauen" zu wollen. Wenn man durch alles hindurchschaut, dann ist alles durchsichtig. Aber eine völlig durchsichtige Welt ist unsichtbar geworden. Wer alles duchschaut, sieht nichts mehr.

C. S. Lewis, Die Abschaffung des Menschen

ZUSAMMENFASSUNG

In dieser Arbeit werden Daten analysiert, die mit dem ALICE-Detektor (A Large Ion Collider Experiment) am Large Hadron Collider (LHC) genommen wurden. Die Eigenschaften und die äußerst gute Leistungsfähigkeit des LHC haben es ermöglicht, Daten von Proton-Proton (pp) Kollisionen in den letzten drei Jahren bei verschiedenen Schwerpunktsenergien (0.9 TeV, 2.36 TeV, 2.76 TeV, 7 TeV und 8 TeV) zu gewinnen. Dazu wurden in zwei der drei Jahre auch Blei–Blei (Pb–Pb) Kollisionen bei $\sqrt{s_{\rm NN}} = 2.76\,$TeV durchgeführt und vor kurzem ein Pilot-Lauf mit Proton-Blei (pPb) Kollisionen bei $\sqrt{s_{\rm NN}} = 5.01\,$TeV, der im Januar/Februar diesen Jahres durch einen vollen Lauf vervollständigt wird.

Die hohen Energien bei gleichzeitig geringem baryochemischen Potential ($\mu_{\rm B} \approx 0$) der Pb–Pb Kollisionen am LHC erlauben die Produktion von Strangeness, Charm und Bottom Quarks in bisher unerreichter Anzahl. Die entweder in der ursprünglichen harten Kollision (Charm und Bottom) oder im Quark-Gluon Plasma entstandenen Quarks werden beim Abkühlen des Feuerballs in Hadronen oder auch leichten Kernen (bis zu A=5) eingebaut. Die Produktionswahrscheinlichkeit nimmt mit der Masse des produzierten Teilchens ab. Aber die hohe Zahl der Strangeness Quarks erlaubt Studien von (Anti-)Hyperkernen wie etwa dem (Anti-)Hypertriton ${}^{3}_{\Lambda}\mathrm{H}$ (${}^{3}_{\overline{\Lambda}}\overline{\mathrm{H}}$). Da solche Kerne in Schwerionenkollisionen nachweislich produziert werden, sollte auch das 1977 postulierte H-Dibaryon nachweisbar sein. Das H-Dibaryon ist ein hypothetischer gebundener Zustand von sechs Quarks (*uuddss*). Die Suche nach dem H-Dibaryon am LHC mit dem ALICE Apparat bildet den zentralen Teil dieser Arbeit. Das Teilchen wurde nicht gefunden und eine obere Grenze wurde gesetzt. Genauso wurde nach einem gebundenen Zustand des Λ-Teilchens mit einem Neutron gesucht. Auch dieses Teilchen wurde nicht gefunden und eine obere Grenze für die Produktion bestimmt.

Das thermische Modell beschreibt die Teilchenproduktion von allen gemessenen Teilchensorten an vorhergegangenen Experimenten, bei verschiedenen Energien, ziemlich gut. Dieses Modell und das Koaleszenz-Modell machen Vorhersagen für die Produktion am LHC. Der Vergleich zwischen dem Experiment und den Modellen führt zu einer Diskrepanz von einem Faktor von 10, den die obere Grenze niedriger liegt als die Modelle.

Dieses Resultat stellt die Existenz dieser beiden Teilchen in Frage.

Ein anderer Teil dieser Arbeit beschäftigt sich mit der Produktion von seltsamen Baryonen, insbesondere der Resonanz $\Lambda(1520)$ in pp Daten, die bei 7 TeV genommen wurden. Dabei wird die Masse, die Breite und die Häufigkeit $p_{\rm t}$ abhängig analysiert. Das so gewonnene Spektrum muss bezüglich der Akzeptanz und Effizienz des Detektors korrigiert werden, um die Produktionshäufigkeit dN/dy des $\Lambda(1520)$ Teilchens zu bestimmen. Diese wird mit der Produktionshäufigkeit des Λ-Hyperons verglichen. Daraus folgt eine gute Übereinstimmung der $\Lambda(1520)$ Produktion relativ zur Produktion des Λ-Hyperons in vorausgegangenen Experimenten NA49 und STAR.

ABSTRACT

Within this work data are analysed which have been taken with the ALICE apparatus (A Large Ion Collider Experiment) at the Large Hadron Collider (LHC). The unique properties and the excellent performance of the LHC made it possible to take data for proton-proton collisions (pp) in the last three years at several center-of-mass energies (0.9 TeV, 2.36 TeV, 2.76 TeV, 7 TeV and 8 TeV). It was further possible to aquire data in two of the three years of lead–lead collisions (Pb–Pb) at $\sqrt{s_{\mathrm{NN}}} = 2.76\,\mathrm{TeV}$ and recently a short pilot run of proton–lead collisions (pPb) at $\sqrt{s_{\mathrm{NN}}} = 5.01\,\mathrm{TeV}$ was recorded. It will be continued as a full run in January/February this year.

The high energies and at the same time low baryo-chemical potential ($\mu_{\mathrm{B}} \approx 0$) in Pb–Pb collisions at the LHC allow the production of strangeness, charm and bottom quarks in up to now unseen quantities. The particles created, either in the initial hard collision (charm and bottom) or in the quark-gluon plasma, end up in hadrons or light nuclei (up to A=5) in the cool-down phase of the fireball. The production probability of particles decreases while its mass is increasing. But the huge amount of strange quarks produced allows the study of (anti-)hypernuclei, like the (anti-)hypertriton ${}^{3}_{\Lambda}\mathrm{H}$ (${}^{3}_{\overline{\Lambda}}\overline{\mathrm{H}}$). Since such particles are measured in heavy-ion collisions it should be possible to also measure particles like the H-Dibaryon, predicted in 1977. The H-Dibaryon is a hypothetical bound state of six quarks (*uuddss*). The search for the H-Dibaryon at the LHC with the ALICE apparatus is the main content of this work. The particle was not observed and an upper limit has been set. Another search for a bound state of a Λ particle and a neutron was also performed. This particle was also not observed and an upper limit for the production yield was estimated.

The thermal model describes the production of all particle species in previously performed experiments, at different energies, quite reasonably. This model and the coalescence model make predictions for the particle production at LHC energies. The comparison between experimental result and these model predictions lead to a factor of around 10 which the upper limit is below the expected yields.

This result questions the existence of these particles.

Another part of this thesis is dealing with the production of strange baryons, especially the baryonic resonance $\Lambda(1520)$ in pp collisions at 7 TeV. Here the focus was to measure mass, width and yield p_{t} dependent. The p_{t} spectrum has to be corrected for the acceptance and efficiency of the detector, to measure the yield per rapidity unit $\mathrm{d}N/\mathrm{d}y$ of the $\Lambda(1520)$. This is compared to the yield of the Λ hyperon. This shows good agreement with the values measured in the previous experiments NA49 at SPS and STAR at RHIC.

Contents

List of Figures

List of Tables

Chapter 1

Introduction

1.1 Quantum Chromodynamics

The current understanding of the strong interaction is described in terms of a gauge theory called Quantum ChromoDynamics (QCD). It is a non-Abelian gauge theory where the gauge quanta are massless but self interacting gluons. The gauge group is SU(3) which incorporates 3 colours, 3 anti-colours and 8 gluons. The Lagrangian density can be written as [ESW03]

$$\mathscr{L}_{QCD} = -\frac{1}{4} F^{A}_{\alpha\beta} F^{\alpha\beta}_{A} + \sum_{\text{flavours}} \overline{q}_a (i\not{D} - m)_{ab} q_b$$

where $F^{A}_{\alpha\beta} = \partial_\alpha A^{A}_{\beta} - \partial_\beta A^{A}_{\alpha} - g f^{\text{ABC}} A^{B}_{\alpha} A^{C}_{\beta}$ is the field strength tensor for spin-1 gluon field A^{A}_{α} [YND06]. g is the QCD coupling constant which is the same for all strong interactions. The capital indices A, B and C run over 8 colour degrees of freedom of the gluon field. The third term of $F^{A}_{\alpha\beta}$ distinguishes QCD from QED, giving rise to triplet and quartic gluon self-interactions and ultimately to asymptotic freedom. There are three main features of QCD which will be discussed here briefly:

- asymptotic freedom
- confinement
- chiral symmetry

Asymptotic freedom

Since t'Hooft prooved that non-Abelian gauge theories are renormalisable [THO71] it is possible to get a handle on infrared safety issues, i.e. divergencies of objects with energies approaching zero, which is equivalent to physical phenomena at very long distances.

But at the same time this leads to a broken scale invariance by the renormalisation. This is cured by the absorption of the physical scale dependence by the running coupling of $g = \frac{(\alpha_s(Q^2))^2}{4\pi}$.

It can be shown that the renormalisation scale dependence cancels order-by-order and for a meaningful prediction at least next-to-leading order (NLO) calculations are needed. This is done using the so-called beta-function of QCD [YND06]:

$$Q^2 \frac{\partial \alpha_s(Q^2)}{\partial Q^2} = \beta\left(\alpha_s(Q^2)\right) .$$

Using this beta-function in lowest order (β_0) one can derive

$$\alpha_s(Q^2) = \frac{\alpha_0}{1+\alpha_0\frac{33-2n_f}{12\pi}\ln(\frac{Q^2}{\mu^2})},$$

with Q being the momentum transfer, α_0 the coupling constant at the momentum transfer μ and n_f the number of flavours.
The noble prize in physics was awarded in 2004 to Gross, Wilczek and Politzer who showed in 1973 [GRO73, POL73] that

$$\alpha_S(Q^2) \to 0 \text{ for } Q \to \infty,$$

which means that QCD is an asymptotically free theory. The effective coupling vanishes at large momenta, respectively short distances. This is due to the colour charge anti-screening.
A typical scale to test QCD is the mass of the neutral gauge boson of the electroweak interaction Z^0. Currently all data is consistent for $\alpha_S(M_Z) = 0.1184 \pm 0.0007$, see Fig. 1.1.

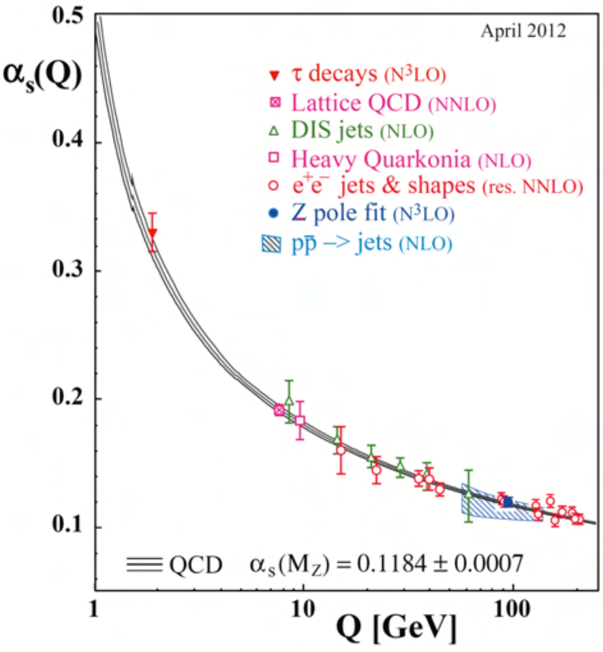

Figure 1.1: Summary of measurements of α_s as a function of the energy scale Q. Figure taken from [PDG12].

Figure 1.1 also shows good agreement between perturbative QCD and the experiment for α_s. At the same time lattice QCD also agrees with both.

Confinement

The increase of $\alpha_S(Q)$ at low scales is often called infrared slavery and leads to confinement and hadronisation. Already from the Fig. 1.1 one can see, that α_s rises for small values of Q. Calculations in this region of interest must use non-perturbative techniques, such as lattice QCD or QCD sum rules [NAR04], or QCD inspired models [ALV86], like bag models.
This behaviour of QCD at low Q leads to the statement that quarks are never observed as free quarks, but

are only observed inside hadrons.
One can convert this and the previously discussed observations into a phenomenological potential of QCD. The potential of quarks decreases with short distances r as $1/r$, this part of the potential is Coulomb like. At larger distances, the potential increases linearly and therefore leads to the confinement of quarks to hadrons. Thus, the potential V for $q\bar{q}$ pairs becomes [YAG05]

$$V(r) = -\frac{4}{3}\frac{\alpha_s}{r} + k\,r\,,$$

it has the asymptotic behaviour $V(r \to \infty) \to \infty$ and $V(r \to 0) \propto 1/r$.

Chiral symmetry

The QCD Lagrangian can be re-written as

$$\mathscr{L}_{QCD} = \mathscr{L}_0 - \sum_{\text{flavours}} \overline{q}_a (m)_{ab} q_b\,.$$

Then the term $\mathscr{L}_0$, shows one symmetry of QCD named chiral symmetry.
This means that if one neglegts the mass term, chiral unitary transformations do not change the properties of $\mathscr{L}_0$ [KOC97, QUI83], i.e. the Lagrangian of QCD with massless fermions is invariant under separate unitary global transformations of the left- and right-handed quark fields.
It was even observed before the advent of QCD that such symmetry might exist. The spontaneous breaking of chiral symmetry was studied to explain the huge mass difference between the pion and the nucleon. This behaviour is known as Partial Conservation of Axial Currents (PCAC) [NAM60], which is closely related to the Goldberger-Treiman relation

$$g f_\pi = g_A m_N\,,$$

with f_π the pion decay constant, g_A the weak axial coupling constant and m_N the mass of the nucleon [QUI83]. Thus the Goldberger-Treiman relation gives a connection between the strong interaction coupling of the pions to the nucleons and the axial vector current coefficient of the nucleon which determines the weak decay rate of the neutron.

Chiral symmetry is spontaneously broken in nature, thus the symmetry does not manifest itself in parity multiplets of hadrons [MOS99, KOC97]. These chiral partners show a mass splitting, which shows the spontaneous breaking of chiral symmetry due to a non-vanishing vacuum expectation value of the chiral quark condensate $\langle 0|\overline{q}q|0\rangle \neq 0$.

The two phases of chiral symmetry are separated by the so called quark condensate $\langle 0|\overline{q}q|0\rangle$. It is the order parameter of the chiral phase transition and should be 0 if the symmetry is restored (Wigner phase). As long as $\langle 0|\overline{q}q|0\rangle \neq 0$ the chiral symmetry is broken and the world exists in a Goldstone phase. The approximate Goldstone modes are represented by the pions, but also η and K mesons are very often counted as Goldstone bosons. A pure Goldstone mode would be massless, but since chiral symmetry is not completely correct the masses of the Goldstone modes are quite low, especially when compared with the mass of the nucleon.

Chiral symmetry restoration

One possible phase transition of QCD is connected to chiral symmetry.
It is expected from calculations connected to the Nambu–Jona-Lasino (NJL) model [BUB05] (or the σ

model [KOC97]) that at a critical temperature the QCD contribution of the quark masses vanish and thus the chiral symmetry is restored, i.e. we switch from the Goldstone phase to the Wigner phase.

This could lead to changes of the properties of the known particle zoo of hadrons, i.e. mesons and baryons.

It should manifest itself even more for resonances when chiral symmetry is restored. Their lifetimes could change (broadening) and/or the mass of the resonances is shifted. Currently a main focus of this subfield of research is laid on low-mass vector mesons, i.e. $\rho(770)$, $\omega(782)$ and $\phi(1020)$ in their dilepton decay channels. The main idea here is that the dileptons would not be affected by passing trough the strongly interacting matter which was created and would exist in a chiral symmetry restored phase, see for instance [RAW00]. While for the hadronic decays of these resonances there is also interaction with the medium from its decay daughters.

1.1.1 Lattice QCD

Lattice QCD has developed to a very useful non-perturbative tool to calculate observables of QCD. It is based on the assumption that the QCD action can be placed on a lattice formulated in discretised space-time [WIL74]. The determination of the aimed QCD observables makes use of Monte Carlo simulations [CRE80, ROT05].

Main issues in this field are the proper choice of the action, which has to obey the symmetries of QCD and all other properties of the gauge, and of the fermions, to describe the quarks.

Depending on these choices one is able to answer different QCD questions on the lattice. Nearly all issues raised in non-perturbative QCD are worked on from the spectrum of hadrons (see for instance [DÜR08]) to the ab-initio calculation of the strong coupling constant (see Fig. 1.1).

The next currently ongoing test for lattice QCD is the calculation of light nuclei properties from first principles. One outcome on the way to this goal are the calculations for the H-Dibaryon which will be discussed later in Chapter 2.

Lattice QCD is also used as a prediction tool for the two previously discussed QCD phase transitions, i.e. chiral and deconfinement phase transition.

It was shown through calculations from lattice QCD that chiral and deconfinement transition happen nearly at the same temperature and that the deconfinement transition is of an analytical crossover type [AOK06]. The pseudo-critical temperature T_c (it is called pseudo-critical because of the crossover type of the phase transition, where no phase boundary exists, whereas for first and second order phase transitions it exists and therefore T_c there is called critical temperature) derived in the most recent calculation is $T_c = (154 \pm 9)$ MeV [HOT12].

1.1.2 Baryon-baryon interaction

The calculations from lattice QCD for particles like the deuteron and other light nuclei can be used to study the baryon-baryon interaction which is responsible for the binding or not binding of baryons to form light nuclei [NPL12, NPL12a, SAV12]. It is not obvious that a proton and a neutron form deuterons and on the other hand two neutrons are unbound. In this scope it is interesting that no stable nucleus exists which contains 5 nucleons (superheavy hydrogen ^{5}H has been observed in 2001 [KOR01] and it decays strongly), but if already one of the nucleons is replaced by a hyperon it is possible to form a hypernucleus ($^5_\Lambda$He was already observed in 1956 [FRY56]) which is stable against strong decays. Thus it only decays weakly.

Effective field theories, like the chiral perturbation theory (ChPT, often also χPT), also allow calculations in the low-energy regime of QCD. The nucleon-nucleon and also the nucleon-hyperon interaction are studied with the help of ChPT to study properties of nuclei and hyper-nuclei [HAI07]. Earlier, ChPT has proven to be quite useful in the description of meson-meson interactions [BIJ07], e.g. $\pi\pi$ scattering. Recently, ChPT also is used for calculations of the hyperon-hyperon interaction [HAI10, HAI13].
It should also be noted here that typically ChPT is used to extrapolate lattice QCD calculations to the physical pion mass, whereas the lattice QCD calculations are usually done at much higher pion masses. Also potential models based on symmetry relations and one-meson-exchange [STO99] can be used to study baryon-baryon interactions.

It is crucial for the understanding of nuclei and hyper-nuclei to get a theoretical handle on the baryon-baryon interaction. Connected to this it is still not fully understood why the deuteron is only bound by 2.2 MeV, whereas nuclei containing more nucleons have typical binding energies of 8 MeV per nucleon. Especially on the experimental sector only limited data on the nucleon-hyperon and the hyperon-hyperon interaction is available. The experimental situation clearly has to be improved [GAL13]. This can be done like it is done in this thesis as search for bound states via invariant mass analysis. Another possibilty, especially if the interactions are too weak to form bound states or if they are even repulsive, is to measure the correlations of the different baryons with each other and extract the potentials from this. ALICE allows both types of measurements, even for multi-strange baryons which are abundantly produced at the LHC.

1.2 Quark-Gluon Plasma

The experimentally well proven confinement does not allow quarks and gluons to be observed freely. They are always bound in hadrons under normal conditions. But they were freed from their hadronic imprisonment, until a few microseconds after the big bang. The quarks and gluons started to form hadrons when the pseudo-critical temperature was passed from higher to lower temperatures. Collisions of nuclei at very high energies also allow to reach such high temperatures, thus it is possible to create the so called Quark-Gluon Plasma (QGP) [PBM07, PBM09].

To say it more general, quarks and gluons are freed from confinement at temperatures which are high enough and/or at high enough densities. In 1975 Collins and Perry [COL75] thought that a new state of strongly interacting matter might be created. In the same year also Cabibbo and Parisi [CAP75] had the idea that in the asymptotically free regime only weakly interacting quark matter would exist.

One can get a rough estimate of a limiting scale in QCD from Heisenberg's uncertainty principle ($\Delta p \Delta x \geq \hbar$) assuming the size of a hadron ($\approx$ 1 fm) as limiting length:

$$\Lambda_{QCD} = \frac{\hbar c}{1\,\mathrm{fm}} = \frac{197\,\mathrm{MeVfm}}{1\,\mathrm{fm}} \approx 200\,\mathrm{MeV}$$

An interesting observation connected to the transition temperature was already made in 1965. R. Hagedorn argued that there is a maximum temperature for hadronic matter based on the increasing density of hadronic states with increasing energy [HAG65]. He assumed for the density of states as function of mass an exponential behaviour

$$\rho(m) \propto \left(m_0^2 + m^2\right)^{-\frac{5}{4}} \exp(m/T_H),$$

with his calculation he observed a limiting temperature T_H of around 158 MeV. But since then the number of known resonances increased.
The Hagedorn temperature T_H was revisited lately by Cleymans and Worku. They used all known resonance states from the PDG (Particle Data Group, the collaboration which collects and summarises the field of particle physics and connected areas - this summary is published every second year and known in the field also as PDG) of 2008 and performed a fit to the hagedorn spectrum. With this they observed a value for $T_H = 177.1\,\text{MeV}$ [CLE11]. Which means that the limiting temperature of the hadron gas is of the same order as the deconfinement temperature estimated from lattice QCD.

Hadrochemistry and thermal model

It is a remarkable fact that the measured yields of different particle species produced in heavy-ion collisions can be described by a statistical model. The simplest model has only three free parameters T, V and μ_b [PBM04, PBM07]. The volume V cancels when particle yield ratios are investigated, for this typically the particle to pion ratio is used.
To test this model properly as many states (resonances and stable particles) as possible have to be measured and compared with the thermal model value, this is done in a fit to all measured particle yields at a given collider energy.

Such fits have been performed for various energies and different collision systems. The RHIC (Relativistic Heavy-Ion Collider at the Brookhaven National Laboratory) data are very well described by the thermal model, see left panel of Fig. 1.2. From this global fit combining measurements of Au–Au collisions at $\sqrt{s_{\text{NN}}} = 200\,\text{GeV}$ a chemical freeze-out temperature $T = 162 \pm 4\,\text{MeV}$ can be evaluated.
Chemical freeze-out here means the time of the fireball evolution, when the hadron yields are frozen and only change through decays. These hadrons are created when the fireball is cooled down such that the QGP can no longer exist, but hadrons are produced, i.e. the deconfinement starts. There is another freeze-out in the fireball evolution which comes later than the chemical freeze-out, which is called thermal or kinetic freeze-out, where the produced hadrons stop to undergo elastic collisions. The thermal freeze-out is extracted for example from the single particle spectra and is typically in the range of 120-140 MeV.

A similar fit to the yet available particles at the LHC measured with the ALICE setup in Pb–Pb collisions at $\sqrt{s_{\text{NN}}} = 2.76\,\text{TeV}$ has been performed and leads to a chemical freeze-out temperature $T = 164 \pm 8\,\text{MeV}$, shown in Fig. 1.2. But shows a nice agreement for most measured particle species except the protons which are left out for this fit.
Investigations have shown that the multi-particle collisions are strongly enhanced at high density and lead to chemical equilibrium very near to T_c [PSW04]. This makes it possible to study the phase boundary of the QCD phase transition via the fits for the different collision enegies and collision systems which define T and μ_B.

Radiative energy-loss as QGP signature

The necessary energy density and temperature, to form a QGP experimentally, can only be reached in heavy-ion collisions. But the real question which comes up is how can we distinguish the confined phase from the created QGP. Several possible signatures have been proposed since the first estimates of the limiting temperature were done. In this section we will highlight the currently most prominent signature, known as jet quenching, and in the following section the proposed signature directly connected with the

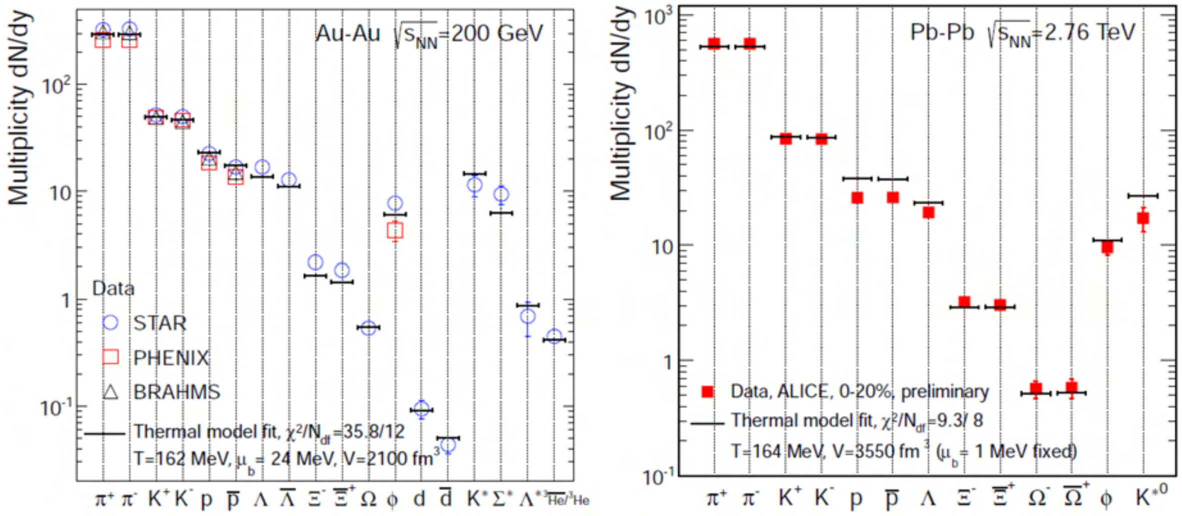

Figure 1.2: Thermal fit for all measured particle species at RHIC (left) and for the currently available ALICE data at LHC (right), from [AND12].

analyses presented in this thesis, called strangeness enhancement. Both signatures date back to the year 1982.

One possible observable, predicted in 1982 by Bjorken [BJO82] is the suppression of particle production at high transverse momentum (p_t). This suppression is often called jet quenching, this name was introduced by M. Gyulassy and M. Plümer in 1990 [GYU90]. High-p_t hadrons originate from partons which are produced predominantly in hard scattering processes. Suppression of these high-p_t hadrons can occur due to energy loss while the corresponding partons traverse the created QGP. A possible measure for the connected energy loss is the nuclear modification factor R_AA, defined as

$$R_\mathrm{AA} = \frac{\sigma_\mathrm{AA}(p_\mathrm{t})}{\langle N_\mathrm{binary}\rangle \sigma_\mathrm{pp}(p_\mathrm{t})} .$$

Here σ_AA is the cross-section for AA (nucleus-nucleus) collisions, σ_pp is the cross-section in pp (nucleon-nucleon) collisions and $\langle N_\mathrm{binary}\rangle$ is the number of binary nucleon-nucleon collisions in the AA collision. $\langle N_\mathrm{binary}\rangle$ is obtained from the inelastic nucleon-nucleon cross section and the nuclear overlap function based on the Glauber model [YAG05].

R_AA measures the influence of the medium produced in AA collisions on particle yields compared the particle yields produced in pp collisions. For this the yield in pp collision has to be scaled with the number of binary nucleon collisions in the corresponding AA collision in a given centrality class. Thus R_AA would yield unity if there would be no medium effect. If the value would go below unity a suppression is observed and in case of an enhancement the value would be above unity.

Of particular interest is the energy loss of heavy quarks since those are produced already in the initial hard collision of partons. Thus the heavy quarks undergo the whole QGP phase, whereas lighter quarks can also be produced inside the QGP. The R_AA spectrum for charged hadrons [ABE12a], an average of D mesons [ABE12b], both measured by ALICE, and the non-prompt J/ψ done by the CMS collaboration [CHA12], measurements are shown in Figure 1.3.

From the theory side an ordering of R_AA for the different quark flavours is expected following $R^B_\mathrm{AA} > R^D_\mathrm{AA} > R^\pi_\mathrm{AA}$ [DOK01], which means that bottomed mesons should loose less energy than light flavoured mesons.

High-p_t suppression was observed first at RHIC (Relativistic Heavy Ion Collider) at the Brookhaven National Laboratory in Au–Au collisions at $\sqrt{s_{NN}} = 130\,\text{GeV}$ [ADC02] and later confirmed at $\sqrt{s_{NN}} = 200\,\text{GeV}$ [ADC05, ADA05]. There a strong suppression (R_{AA} between 0.2 and 0.25) was measured for light-flavour hadrons in central collisions. At the LHC the value goes even further down to a $R_{AA} \approx 0.14$ at $p_t \approx 6-8\,\text{GeV}/c$ in central Pb–Pb collisions at $\sqrt{s_{NN}} = 2.76\,\text{TeV}$. This leads to the conclusion that the medium created at the LHC is denser than the one created at RHIC. So far the suppression of heavy-flavour hadrons at RHIC was only measured indirectly from their inclusive decay electrons [ADL06, ABE07, ADA11]. It is close to the measured R_{AA} of π mesons and not as high as expected based on radiative energy loss [ARM06, ARM10]. The analysis of heavy-flavour electrons is also done in ALICE at the LHC and shows good agreement with the averaged D mesons shown in Fig. 1.3.

The CMS Collaboration measured also a strong suppression ($R_{AA} \approx 0.35$) for non-prompt J/ψ particles from B meson decays at the LHC [CHA12], shown in Fig. 1.3.

Comparing these different measurements it is currently not totally clear if the ordering for radiative energy loss of the different flavours is valid. It seems that further improvement is needed on both sides: experiment and theory. But it is clear from the observation of such a high suppression that a special kind of matter has formed in Pb–Pb collsions at the LHC.

1.2.1 Strangeness

Historically, the study of strangeness in heavy-ion collisions was proposed in 1982, by Rafelski and Müller [RAF82], where they suggested the so-called strangeness enhancement as a signature for the formation of a QGP. This idea was then enlarged in [KMR86]. It will be discussed here shortly, even if

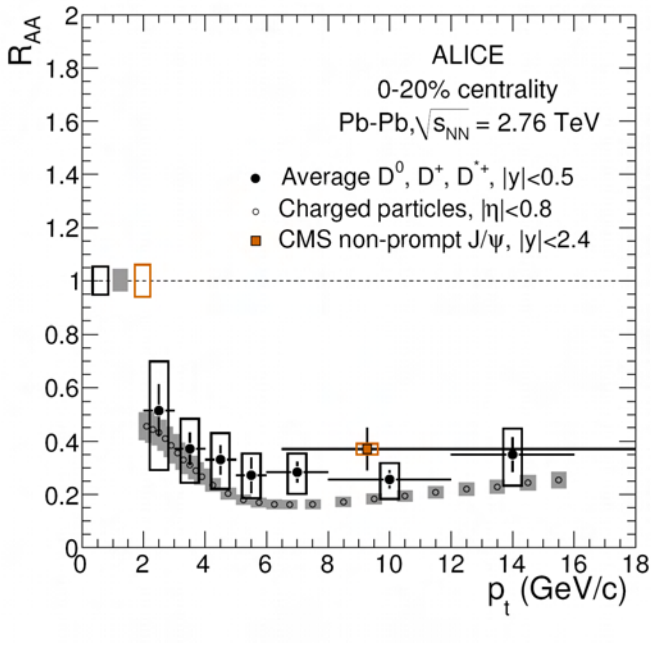

Figure 1.3: Average R_{AA} of D mesons in the 0-20 % centrality class compared to the nuclear modification factors of charged particles [ABE12a] and non-prompt J/ψ from B decays [CHA12] in the same centrality class. Taken from [ABE12b].

the collected experimental observations favour a different explanation.

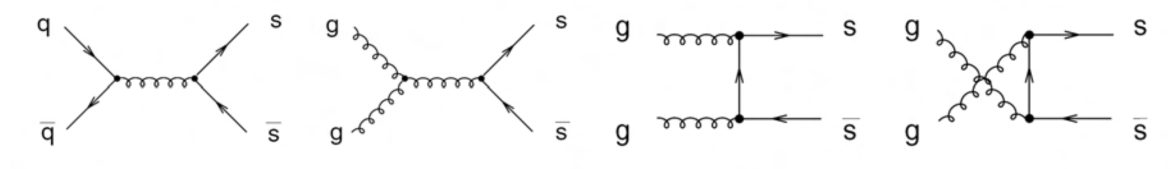

Figure 1.4: Leading order Feynman diagrams for strangeness production.

In their article they follow mainly two lines of argumentation:

- The production threshold for the production of strangeness via $\overline{s}s$ pairs is considerably lower than the one for hadrons. For this argument they compare the energy needed to produce strange particles for a gas of quarks and gluons to those for a hadron gas. The associated $\overline{s}s$ pair production can proceed by the fusion of two gluons $g+g \to s+\overline{s}$ or two (massless) light quarks ($q = u,d$), $q+\overline{q} \to s+\overline{s}$, which involves only $Q_{QCD} = 2m_s \approx 200\,\mathrm{MeV}$. But in the processes connected to a hadron gas like $NN \leftrightarrow N\Lambda K$ the involved scale Q_{HG} is larger: $Q_{HG} = m_\Lambda + m_K - m_N \approx 670\,\mathrm{MeV}$. This should lead to larger production of strangeness in the QGP compared to a hadron gas.

- The timescale for the equilibration of the production of strange particles in a QGP is significantly smaller than that for a hadron gas. Which means that the number of particles produced in a QGP should be close to the equilibrium value and not be suppressed by any dynamical effects which would occur from hadronic interactions.
  The production via gluons has three possible Feynman diagrams at lowest order, whereas the light quark mechanism only has one. All lowest order diagrams are shown in Fig. 1.4. Rafelski and Müller calculate the rate of $\overline{s}s$ production and show that the dominating production process is $g+g \to s+\overline{s}$. This would allow the enhanced production of (multi-)strange hadrons in a heavy-ion collison if a QGP was formed. But this would not be true in a pure hadronic world.

Experimental collaborations have studied (multi-)strange particle production since then. A recent compilation of the ratios is shown in Fig. 1.5. It shows the yield measured in AA collisions compared to the scaled pp (and pBe for the NA57 results) versus the average number of participants. Debates are ongoing on the interpretation since data of WA97 appeared, the data shown as comparison in Fig. 1.5 are from its successing experiment NA57 [BLM11]. The figure also shows data from STAR (an experiment at RHIC) and the comparison of these different experimental results indicate that the observed enhancement decreases when the center-of-mass energy of the collision is increasing. The increase of the yield, relative to the scaled reference, of particles containing more strangeness, shown on the left panel of Fig. 1.5 was predicted in [RAF82]. Where they expect an ordering of the enhancement E of the particles of $E(\Omega) > E(\Xi) > E(\Lambda)$.

Todays interpretation is that the visible enhancement is not due to an enhancement in AA collisions but a suppression in pp [BLM11]. This suppression is called canonical suppression, since it can be explained using a thermal model with a canonical formulation of strangeness conservation [HAM00]. In the canonical formulation of the thermal model the conservation of quantum numbers is done exactly on an event-by-event basis. Whereas the grand canonical formulation (used in heavy-ion collisions) implements the conservation of quantum numbers only on average by using the corresponding chemical potential, e.g. baryochemical potential or the chemical potential of strangeness. The canonical

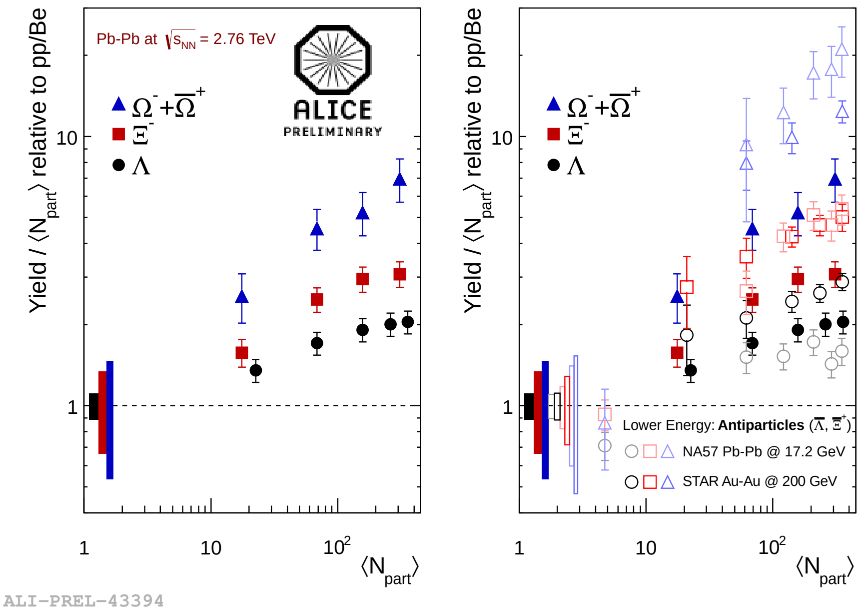

Figure 1.5: Yields of strange particles (Λ, Ξ^- and Ω^-) compared to the yields measured in pp, respectively in pBe; the correponding antiparticles are only shown for experiments at lower energies.

formulation can also very well describe the decrease of the enhancement with increasing collision energy [RED02] and the observed ordering connected to the strangeness content [TOU03].

But nevertheless strangeness remains an interesting probe for the medium created in heavy-ion collisions. Since the thermal model is able to describe yields in heavy-ion collisions quite well it is interesting to note that they show some deviation looking at strange resonances at RHIC [ABE05]. In Fig. 1.6 the STAR collaboration compares the resonance to stable particle ratios from their measurement with the thermal model and a transport model, called Ultrarelativistic Quantum Molecular Dynamics (UrQMD). Both show deviations for the $\Lambda(1520)$ (in the figure named $\Lambda^{\star}$) in more central collisions where they agree better at more peripheral collisions.

Even if the strangeness enhancement is not a good signature of the QGP, strangeness itself remains an interesting probe of the medium created in heavy-ion collisions. The strange quark plays an important role in QCD itself. Its mass is nicely seperated from the light quarks (u, d) and the heavy quarks (c, b) which makes it produceable thermally inside the hot fireball, whereas b and c quarks are produced in the initial hard collision. But strange quarks also have a certain influence on the thermodynamic properties of QCD. The mass m_s of the strange quark controls the properties of the chiral and the deconfinement transition [BRO90], this is visible from the so-called Columbia plot 1.7. Where the possible transition order is plotted depending on the mass of the light quarks versus the mass of the strange quark. The plot itself is extracted from lattice QCD calculations.

The LHC gives the further advantage that strangeness is abundantly produced, both in pp and Pb–Pb collisions. ALICE has measured that around 30 Lambda, around 4 Xi and close to one Omega is produced per central event and rapidity unit. This shows that enough strangeness is produced per event, to start looking into the production of rather rarely produced exotics containing strangeness which are studied in this thesis.

The main part of this work is the search for the H-Dibaryon, followed by the search for the Λn bound state, both in Pb–Pb collisions at $\sqrt{s_{\mathrm{NN}}} = 2.76\,\mathrm{TeV}$. The first particle is a six-quark state and the latter a particle which was observed by the HypHI experiment at GSI [HYP11, HYP12]. Both will be discussed a bit more in the next chapter about exotica.
Another part of this thesis is connected with strange baryons produced in pp collisions at $\sqrt{s} = 7\,\mathrm{TeV}$. We discuss the Λ a bit more general in chapter 4, since it is also a necessary part of the H-Dibaryon

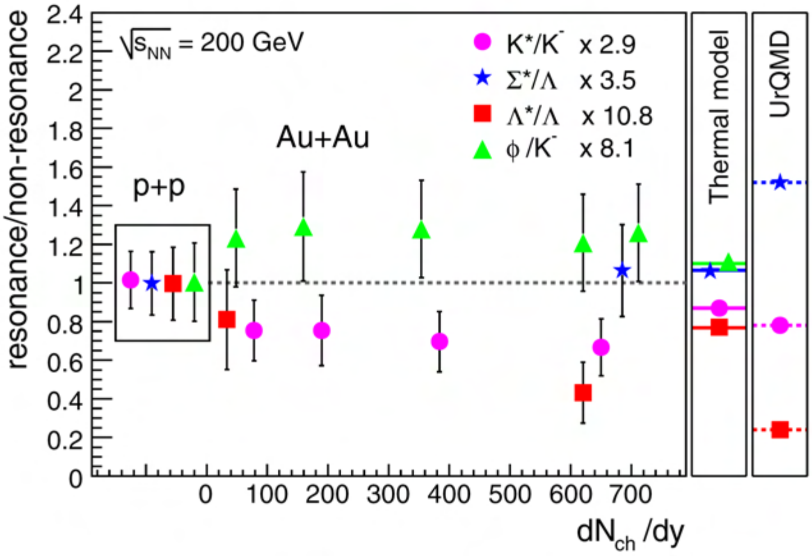

Figure 1.6: Ratios of resonances to stable particles measured by the STAR Collaboration versus charged particles per rapidity unit (dN_{ch}/dy) and predictions from the thermal model and UrQMD. Figure taken from [ABE05].

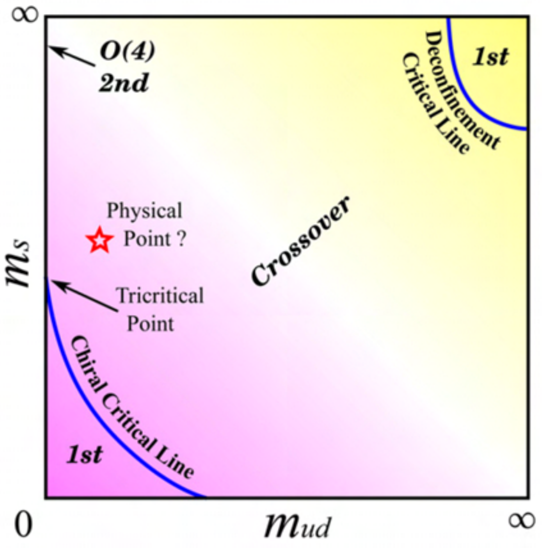

Figure 1.7: "Columbia plot": landscape of the possible phase transition order depending on the light quark masses (u, d) on the x-axis and the strange quark mass on the y-axis, taken from [FUK11].

search, and then use the Λs in pp collisions to show the capabilities of a possible analysis of Σ^0, Ξ^- and $\Sigma(1385)$ connected with the Λ. But we concentrate our investigations on the $\Lambda(1520)$, a baryonic resonance decaying into pK^-. We focus here only on pp collisions for the $\Lambda(1520)$, they provide a baseline for Pb–Pb collisions. These investigations are described in chapter 5.

Chapter 2

Exotica

2.1 Overview

In principle QCD does not prevent particles to not be ”normal” experimentally observed hadrons, i.e. baryons (containing 3 quarks) or mesons (consisting of a quark and an anti-quark), respectively their anti-particles [GEL64]. In other words QCD might allow for states which are not made from either three quarks or a quark-anti-quark pair.

Such objects are usually called exotics or exotica. Several states have been predicted by theoretical models, some of them have been claimed to be found already. But final conclusions have not been made. Of particular interest are particles either consisting completely of gluons (so-called glueballs) and quark composites of different types, for example pentaquarks [KLE07], consisting of 4 quarks and one anti-quark. Often also bound states of hadrons which do not occur in every-day matter are called exotica. A good example are hypernuclei, where at least one hyperon (a baryon containing at least one strange quark) is bound in the nucleus. The lightest possible hypernucleus is a bound state of a proton, a neutron and a Λ. It is called hypertriton ${}^{3}_{\Lambda}$H. It should be noted that the anti-hypertriton was discovered recently in heavy-ion collisions at RHIC by the STAR collaboration [ABE10]. Another class of exotica are so-called kaonic clusters, where a charged kaon could bind two protons to form a ppK cluster. There are also heavier versions of these clusters predicted [YAM02]. In connection to these clusters the $\Lambda(1405)$ resonance is seen as a pK^- bound state [YAM04].

Other possible exotica would be built from two anti-quarks and two quarks (tetraquark) or consist of six quarks. The latter would be a so-called hexaquark.

One example for such a particle was postulated by Jaffe in the year 1977, it is supposed to consist of 6 quarks ($uuddss$) [JAF77]. This hexaquark or so-called H-Dibaryon has a total angular momentum and isospin zero with positive parity ($J^P = 0^+$, $S = -2$). It would be a flavour as well as a colour singlet. In the context of strange quark matter the H-Dibaryon is seen as the smallest strangelet candidate [GRE99].

2.2 H-Dibaryon

2.2.1 Models for the description of the H-Dibaryon

The strength of the interaction between quarks increases with the distance between themselves. Low-energy processes can only be described analytically by using simplified models. These try to capture the dominant parts within the interaction of quarks and gluons within low energy surroundings. Usually they have a couple of free parameters, which according to measured characteristics (mass, spin etc.) of well known particles (e.g. π, p or Λ) can be distinguished. These models can be utilised to describe the

H-Dibaryon. Common to all these models is the assumption that the chromo-magnetic hyperfine structure provides the necessary energy to bind the H-Dibaryon. The chromo-magnetic hyperfine structure is analogue to the quantum electrodynamics, but caused by a one-gluon exchange. So it is similar to the electromagnetic hyperfine structure, which can be observed for example in the hydrogen atom. Since it is significantly stronger than the electromagnetic analogon it is responsible for the mass difference for particles with spin 0 and their partners with spin 1. The mass difference from, e.g. K and $K(890)$ (often only called $K^\star$), mesons or from N and Δ is more than 300 MeV/c^2. In the following part we will take a closer look at a couple of models for the ascertainment of the mass of the H-Dibaryon. A review showing the large range of predictions for the mass of the H-Dibaryon can be found in [SAK00]. Several different models are discussed there but we will only highlight some of them.

2.2.2 Theoretical statements about the H-Dibaryon mass

Bag model

The bag model, we focus here on the MIT bag model, since it was the method used to calculate the hexaquark state of *uuddss* which is called H-Dibaryon. A first bag model was introduced by Bogolioubov [BOG68] in 1968, where he limited the freedom of the quarks by a boundary condition. This was found to violate energy-momentum conservation at the bag surface by the MIT group. This led them to develop their own model which is still widely used to get a rough estimate of QCD observables.

MIT bag model

The MIT bag model was developed by a group hosted at Massachusets Institute of Technology in the early seventies [CHO74, CHO74a]. It is a QCD-inspired model which can describe basic properties of hadrons and incorporates the confinement of quarks inside the hadron. This is fullfilled as a spatial confinement caused by an external pressure which restricts the quarks to move only inside the region of spatial confinement, called bag. These boundary conditions do not allow the quarks to leave the bag. The Hamiltonian of the model can be written as

$$H_{\text{bag}} = H_{\text{kinetic}} + H_{\text{spin-spin}} + H_{\text{volume}} + H_0 \,,$$

where the volume term is simply given by BV. Here B is the bag constant and V the bag volume, which is in the easiest case only the volume of a sphere $V = \frac{4}{3}\pi R^3$. The bag constant B represents the external pressure and is scalar since Lorentz invariance has to be conserved.
Each quark occupies a single particle orbital and if all quarks are in their ground state the bag becomes spherical. As long as the quarks are inside the bag, they can move quasi-free.

With these assumptions it is possible to describe the masses of light hadrons quite reasonably [DEG76]. If R of the bag is set to the radius of the nucleon ($\approx$ 1 fm), the bag model predicts a nucleon mass that is within 30% of the actual mass. Even though the model is not able to describe the pion mass or any pion-mediated interaction.

One has to admit that chiral symmetry is explicitly broken on the bag surface, i.e. the boundary conditions. This can be cured by extending the MIT bag model by introducing for instance pion fields which couple the quarks to the surface [ALV86]. This model is then called cloudy bag model [ALV86]. Another possibility to solve this problem is to introduce skyrmions into the model which leads to the chiral bag model [ALV86].

H-Dibaryon from the MIT bag model

The contribution of the chromo-magnetic one-gluon exchange to the binding energy in the MIT bag model (pointed out by Jaffe [JAF77]) is given by

$$E_{hfs} = -\sum_{i>j} \lambda_i^a \lambda_i^a \sigma_i \sigma_j M(m_i R, m_j R),$$

where σ_i (λ_i) is the spin (colour) vector of the ith quark normalised to 3 (2) and $M(m_i R, m_j R)$ measures the interaction strength.

In the absence of antiquarks the previous equation can be transformed to [JAF77]

$$E_{hfs} = (8N - \frac{1}{2}C_6 + \frac{4}{3}J(J+1))\overline{M},$$

Where N stands for the total number of quarks, J for the total angular momentum and C_6 for the eigen-value of the Casimir operator for the colour-spin SU(6).

This interaction depends on the orientation of the spins and leads to an attraction for anti-parallel spins and to repulsion for parallel spins. It can explain the energy splitting between octet and decuplet of baryons and for the nonets of pseudoscalars and vector mesons. The contribution given by this interaction is the main reason for a possible bound state as pointed out in [JAF77]. But Jaffe assumes here the mass of the strange quark to be zero. At the same time he suggests regions of masses where the H could lie. Since Jaffe's publication in the year 1977 there were several corrections done to this model. For example the influence of the movement of the quark within the barycenter system [LIU82] or treat with pionic corrections [MUL83]. These corrections switch the possible mass of the H-Dibaryon partially close to the ΛΛ threshold sometimes even beyond that [LIU82, MUL83, ROS86, GOL92].

Lattice QCD calculations

As mentioned in the introduction, lattice QCD has become a useful method to describe low energy QCD processes. In the framework of (hyper-)nuclear physics calculations to describe complete nuclei have been started and use the H-Dibaryon as a six quark state as an interesting object of study.

Lattice calculations have been performed since the 1980s. The precision of their predictions is limited by the possible lattice spacings and the implemented actions and fermions. While most of the older calculations tended to the unbound or resonant H-Dibaryon [WET03], some results indicated a possible mass range between 1.88 GeV/c^2 [IWA88] up until an unbound hexaquark.

Recently, lattice calculations have been performed with higher accuracy (improved fermions and smaller lattice spacings) showing evidence for a bound H-Dibaryon. These calculations have been performed by two lattice QCD groups: the HAL QCD [HAL11] collaboration and the NPLQCD [NPL11] collaboration. The lattice results are summarised in Fig. 2.1. This led also to a new interest from the experimental side.
Although these calculations have been done at an unphysical pion mass ($m_\pi \approx 390\,\mathrm{GeV}/c^2$). When those results are extrapolated chiraly [SHA11, HAI11] towards the physical point the H is rather unbound: either by $13 \pm 14\,\mathrm{MeV}$ (so it could still be bound by 1 MeV) above the ΛΛ (2.231 GeV/c^2) threshold or even close to the Ξp threshold (2.26 GeV/c^2). A binding energy of around 1 MeV is also favoured from the observed double Λ hypernuclei, which gives the current constraints on the ΛΛ interaction, for a recent discussion see 2.2.4 and [BOT12].

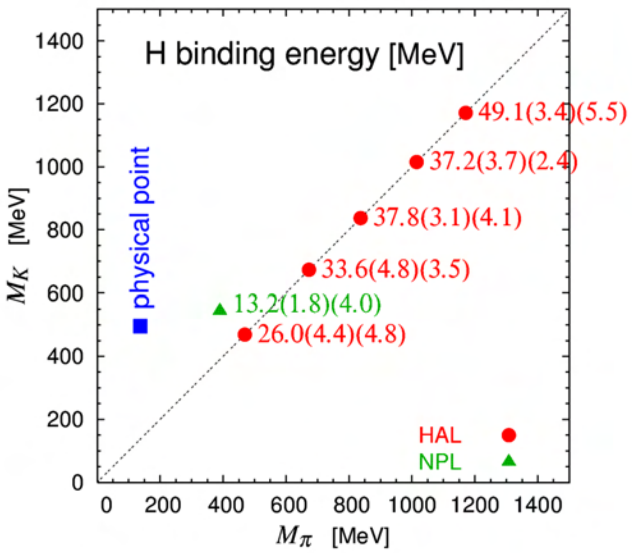

Figure 2.1: Lattice QCD results for the binding energy of the H-Dibaryon depending on the kaon and the pion mass from the HAL (red dots) and the NPL (green triangles) collaborations. Figure from [INO12], based on [HAL11].

Other models

Apart from the already mentioned models to calculate the mass of the H-Dibaryon there are other possible ways. Scoccola and Thomas [SCO94] use the Skyrme model and get a binding energy of 34 MeV for the H-Dibaryon. But after the application of necessary corrections, which are needed to better describe the deuterons, the H is found to be an unbound state. Other authors get a binding energy of about 90 MeV [KLE96]. Other models utilised to describe the H-Dibaryon are reviewed in [ALV86], i.e. QCD sum rules, instanton interaction and static quark models. According to [SAK00] the values scatter around the $\Lambda\Lambda$ threshold within ranges of the order of 100 MeV/c^2.
A final verdict about the correct description of the one or the other model can only be facilitated through an experimental analysis about the existence or the non-exsistence of the H-Dibaryon. This means the models have to be tested and verified or falsified.

2.2.3 Expected branching ratios of the H-Dibaryon and the connected lifetimes

The only definitively assured six-quark system is the deuteron. In analogy to this it is possible that also bound states of two Λs or a Λ and a neutron exist. The latter might have been observed by the HypHI collaboration at GSI [HYP11] and will be also investigated experimentally later on.

Donoghue, Golowich and Holstein calculated the possible lifetime and branching ratios for the mass range from 1.88 GeV/c^2 up to the $\Lambda\Lambda$ threshold for the H-Dibaryon [DON86]. This was done because at that time discussions were ongoing if the cosmic rays reaching earth are made of H-Dibaryons coming from a pulsar and could be responsible for the observation of unusal large numbers of muons in an underground experiment [MAR85, BAY85]. The results for the lifetime of the H-Dibaryon is shown in Fig. 2.2 and led them to the conclusion that the possible lifetimes of the H-Dibaryon can not be the cause of the so-called Cygnus X-3 events. The dashed line in Fig. 2.2 corresponds to the possible lifetimes for

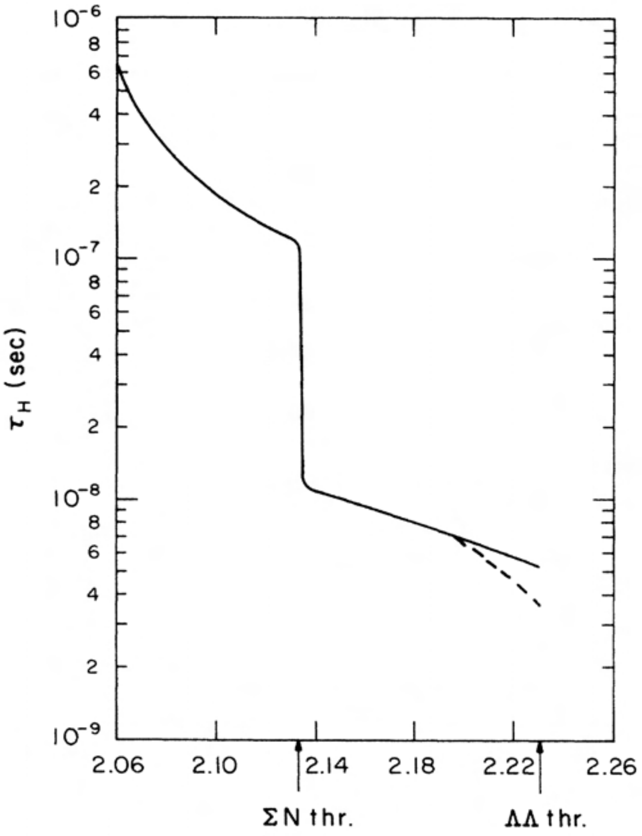

Figure 2.2: Possible H-Dibaryon lifetimes depending on their mass, taken from [DON86].

the H$\rightarrow \Lambda p\pi^-$ decay channel.

The lifetimes are strongly depending on the mass of the H and thus are also the branching ratios. The branching ratios, depending on mass and the corresponding average lifetime, are summarised in Fig. 2.3.

These calculations are using a P-Matrix formalism which *represents a rigorous way to connect this artificially confined six-quark state with the real strongly interacting final state*, according to the authors [DON86]. But the only experimentally easy accessible decay channel is the H$\rightarrow \Lambda p\pi^-$ which causes them some troubles. They argue that from a simple perspective one would have thought that the pionic mode, which becomes allowed above the $\Lambda p\pi$ threshold, should only give small corrections. But they found that p-waves become important for the calculation of the branching ratio, whereas they have only used s-waves for the decays into only baryons. They further state: *The overall transition amplitude for the H$\rightarrow \Lambda N\pi$ is beyond the technical capabilities of present quark -model methods due to number of particles in the final state. Likewise the strong pion vertex is not presently calculable* [DON86].

The lightest two baryon system with a quark content equivalent to the H-Dibaryon (*uuddss*), is the ΛΛ system. This ΛΛ system could also be bound and this bound state would have the same quantum numbers. It was first studied in [KRI82]. Thus it is natural to also have a look at this bound state. Several dibaryons with different strangeness content have been studied theoretically in [JSB00] and at the same time suggestions are given how to measure them in relativistic heavy-ion collisions. The authors provide

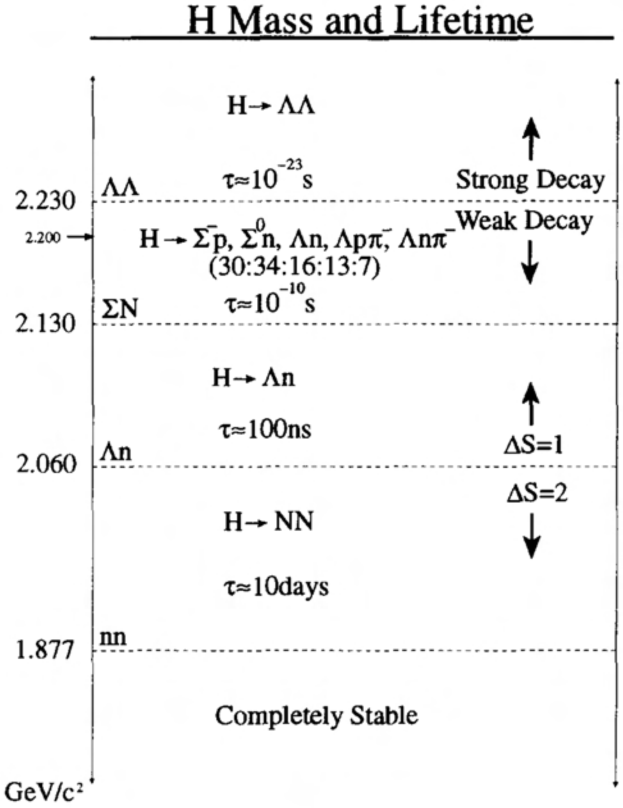

Figure 2.3: Possible mass regions of the H-Dibaryon and the connected lifetimes, branching ratios respectively. The different thresholds are indicated by the dashed lines. Figure taken from [CRA98].

in this article the branching ratios for the $\Lambda\Lambda$ bound state depending on the binding energies. This is shown in 2.4 and it leads to a value of around 10 % at a binding energy of 15 MeV and a value of 64 % close to the $\Lambda\Lambda$ threshold for the $\Lambda\Lambda$ bound state decaying into $\Lambda p\pi^-$. Recent calculations show even a better agreement for the branching ratios between H-Dibaryon and the $\Lambda\Lambda$ bound state [JSB12] which makes it feasible to treat them equally.

2.2.4 Experimental constraints on the H-Dibaryon mass

A valid experimental constraint on the possible binding energy of the H-Dibaryon or the $\Lambda\Lambda$ bound state is the existence and observation of double Λ hypernuclei. These have been discovered in 1963, were a first event of a decay of a double Λ hypernucleus was observed in a nuclear emulsion experiment [DAN63]. Since then 6 further events have been detected. Their interpretation is not always unambiguous since they decay sequentially. The most prominent example is the ”NAGARA” event [TAK01] where the following sequence is visible: $\Xi^- + ^{12}\mathrm{C} \rightarrow ^{6}_{\Lambda\Lambda}\mathrm{He} + ^{3}\mathrm{H} + ^{4}\mathrm{He}$ which lead to the decay $^{6}_{\Lambda\Lambda}\mathrm{He} \rightarrow ^{5}_{\Lambda}\mathrm{He} + \mathrm{p} + \pi^-$ where the $^{5}_{\Lambda}\mathrm{He}$ further decays through $^{5}_{\Lambda}\mathrm{He} \rightarrow ^{3}\mathrm{H} + \mathrm{p} + \mathrm{n}$. This sequence shows also the main production mechanism of those events via a Ξ^- capture since the transfer of $S = 2$ is needed to create a double Λ hypernucleus. The 7 identified double Λ hypernuclei events are summarised in Tab. 2.1. They all have been observed in emulsion experiments and have been re-analysed

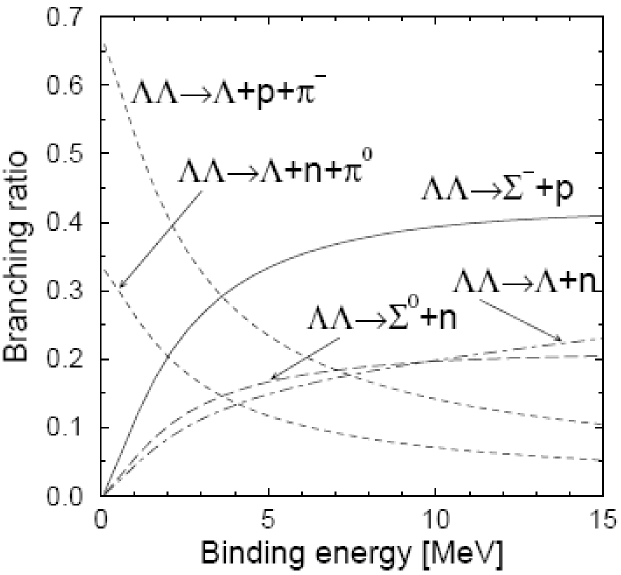

Figure 2.4: Theoretical calculation of the branching ratios depending on the binding energy of the $\Lambda\Lambda$ bound state for different decay channels, taken from [JSB00].

recently [GAL11, GAL12].

The binding energies of the double $\Lambda\Lambda$ hypernuclei ($B_{\Lambda\Lambda}$) provide upper limits for that of the H-Dibaryon ($B_H \leq B_{\Lambda\Lambda}$). For the binding energy $B_{\Lambda\Lambda}$ of a hypernucleus with the order number Z and the nucleon number A (${}^{A}_{\Lambda\Lambda}Z$) the following applies: $B_{\Lambda\Lambda} = M({}^{A-2}Z) + 2M_\Lambda - M({}^{A}_{\Lambda\Lambda}Z)$. If this relation also applies for an H-Dibaryon of a mass M_H, then a transition through the strong interactions with ${}^{A}_{\Lambda\Lambda}Z \rightarrow {}^{A-2}Z + \mathrm{H}$ is energetically supported:

$$M_H < 2M_\Lambda - B_{\Lambda\Lambda}\,.$$

Aoki and colleagues [AOK91] provide for the interpretation of a ${}^{10}_{\Lambda\Lambda}$Be double hypernucleus an extreme value of (2222.8 ± 0.7) MeV/c^2 and for a ${}^{13}_{\Lambda\Lambda}$B a lower value of (2203.7 ± 0.7) MeV/c^2. From the re-analysis of the double Λ hypernuclei data by Gal and Millener [GAL11, GAL12] (compiled in Table 2.1) one can say that the maximal binding energy is about 20 MeV. A recent discussion of these results in the view of the chiral constituent quark model can be found in [CAR12].
The so-called "NAGARA" event reported in 2001 is interpreted uniquely as the sequential decay of ${}^{6}_{\Lambda\Lambda}$He. The mass and the values of $B_{\Lambda\Lambda}$ and of the $\Lambda\Lambda$ interaction energy $\Delta B_{\Lambda\Lambda}$ were determined without ambiguities. The small value of $\Delta B_{\Lambda\Lambda}$ suggested an attraction weaker than the one previously estimated. It also gave the most stringent constraint to the mass of the H-Dibaryon to date (i.e., $M_H \geq 2223.7$ MeV/c^2 at a 90% confidence level [BOT12, TAK01]).

2.2.5 Previous searches for the H-Dibaryon

Since Jaffe's prediction in 1977 experiments started to look for the predicted state. A lot of experimental effort has been put into it. It turned out to be a challenging measurement especially accounting the large span of possible mass of the H-Dibaryon, from 1.88 GeV/c^2 till around 2.6 GeV/c^2, combined with the

Event	Nuclide	$B_{\Lambda\Lambda}$ (MeV/c^2)	$\Delta B_{\Lambda\Lambda}$ (MeV/c^2)	Reference	$B_{\Lambda\Lambda}$ (MeV/c^2) [GAL11]
Danysz et al.	$^{10}_{\Lambda\Lambda}$Be	17.7 ± 0.4	4.3 ± 0.4	[DAN63]	14.94 ± 0.13
Prowse	$^{6}_{\Lambda\Lambda}$He	10.9 ± 0.5	4.7 ± 1.0	[PRO66]	discarded
Aoki et al.	$^{13}_{\Lambda\Lambda}$B	27.5 ± 0.7	4.8 ± 0.7	[AOK91]	23.21 ± 0.21
	$^{13}_{\Lambda\Lambda}$Be	23.3 ± 0.7	0.6 ± 0.8	[NAK10]	20.72 ± 0.20
NAGARA	$^{6}_{\Lambda\Lambda}$He	7.13 ± 0.87	1.0 ± 0.2	[TAK01]	6.91 ± 0.16
DEMACHIYANAGI	$^{10}_{\Lambda\Lambda}$Be*	11.90 ± 0.13	-1.52 ± 0.15	[AHN01]	14.97 ± 0.22
MIKAGE	$^{6}_{\Lambda\Lambda}$He	10.06 ± 1.72	3.82 ± 1.72	[TAK03]	discarded
	$^{11}_{\Lambda\Lambda}$Be	22.12 ± 2.67	3.90 ± 2.71	[NAK10a]	18.40 ± 0.28
HIDA	$^{11}_{\Lambda\Lambda}$Be	20.49 ± 1.15	2.27 ± 1.23	[NAK10]	18.40 ± 0.28
	$^{12}_{\Lambda\Lambda}$Be	22.23 ± 1.15		[NAK10]	20.85 ± 0.20

Table 2.1: Summary of observed double Λ hypernuclei. The event observed by Aoki et al. has two possible interpretations as well as the "HIDA" event and the "MIKAGE" event.

huge possible lifetime estimates, from totally stable downwards to 10^{-23} s for a resonant state. This makes the experimental searches quite difficult.

Nevertheless many tries have been carried out following mainly two strategies:

- Experiments trying to create the H-Dibaryon through strangeness exchange, similar to the hypernuclei production experiments.
- Heavy-ion collisions where quasi all possible states are generated in the cool down of the created fireball. Either described by a thermal model or a coalescence picture. Both will be discussed later in section 2.3 when predictions are summarised.

Except some observations of single candidates, which could not survive a deeper analysis, none of the experiments was so far successful and upper limits in the different mass regions have been given. The current only existing candidate would point to a resonant H-Dibaryon in the $\Lambda p \pi^-$ decay channel [YOO07] by the KEK-PS E522 collaboration. Since this experiment was stopped some members of this collaboration handed in a letter of intent for a "Large Acceptance Hyperon Spectrometer" at the 50 GeV proton synchrotron at J-PARC in Japan [AHN11].

2.3 Production Models

We describe here shortly the two currently preferred models for production of hadrons in relativistic particle collisions which also made predictions for the H-Dibaryon (and the Λn bound state) at the LHC.

2.3.1 Thermal model

The thermal model assumes a thermally and chemically equilibrated system of non-interacting hadrons and resonances with the particle density

$$n_i = \frac{g_i}{2\pi^2} \int_0^\infty \frac{p^2 dp}{e^{(E_i(p)-\mu_i)/T} \pm 1},$$

with $E_i = \sqrt{p^2 + m_i^2}$. The chemical freeze-out temperature T_{ch} and the baryo-chemical potential μ_{B} are usually determined from the fit of experimental data. To make this fit properly, feed-down of particles decaying weakly has to be taken into account. Feed-down from resonances are more problematic since they are hard to subtract experimentally, whereas weak decays into charged hadrons like V0s are possible to correct for. The model has proven to be very useful from the AGS up to RHIC energies [PBM04]. It was even able to describe hadron production at e^+e^- colliders [AND09] and in pp/p$\bar{\text{p}}$ collisions [AND09a]. The first available preliminary yields from the ALICE Collaboration have been fitted and give currently a best fit for $T_c \approx 152\,\text{MeV}$, $V = 5300\,\text{fm}^3$, whereas μ_B is fixed to be 1 MeV. If the protons are left out of the fit, the following values are retrieved: for $T_c \approx 164\,\text{MeV}$, $V = 3550\,\text{fm}^3$ and μ_B is fixed to be 1 MeV. This fit is shown in Fig. 1.2.

Also several predictions have been made using $T_c = 164\,\text{MeV}$. We show here predictions for the Λ, several hypernuclei systems (${}^{3}_{\Lambda}\text{H}$, ${}^{4}_{\Lambda}\text{H}$, ${}^{4}_{\Lambda}\text{He}$ and ${}^{4}_{\Lambda\Lambda}\text{H}$), the anti-alpha and the two objects of interest, i.e. H-Dibaryon and Λn bound state, in Fig. 2.5. These predictions span eight orders of magnitude. Whereas the H-Dibaryon and the Λn bound state lie in the upper third of these span of predictions.

From the statistical hadronization model one gets a value for the possible yield per rapidity unit in central collisions which is for the H-Dibaryon $\text{d}N/\text{d}y = 1.016 \times 10^{-2}$. This has to be divided by 4 to get the value for 0-80 % centrality which is analysed here, which leads to $\text{d}N/\text{d}y|_{0-80\%} = 3.1 \times 10^{-3}$.
For the Λn bound state this is $\text{d}N/\text{d}y = 6.5 \times 10^{-2}$. This has to be adjusted to the 0-80 % centrality which is analysed here, which leads to $\text{d}N/\text{d}y|_{0-80\%} = 1.625 \times 10^{-2}$.

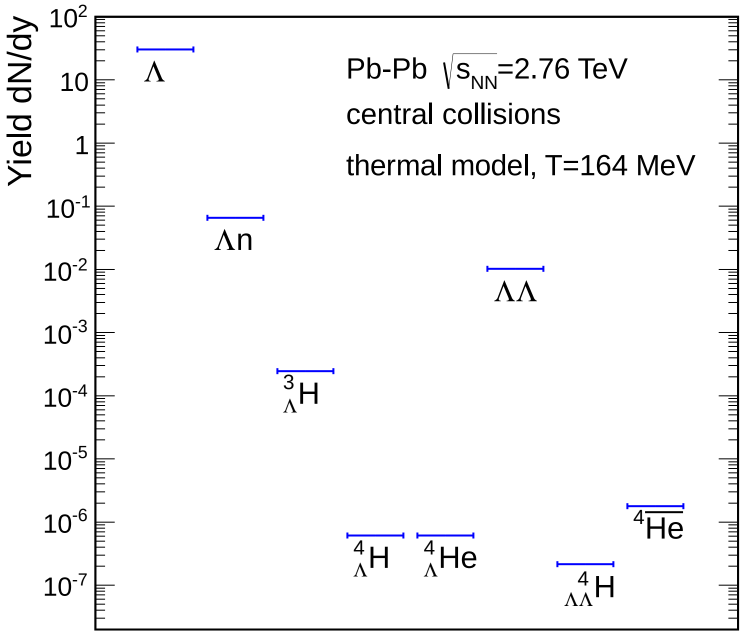

Figure 2.5: $\text{d}N/\text{d}y$ prediction for most central events from the statistical hadronization model for Pb–Pb collisions at $\sqrt{s_{\text{NN}}} = 2.76\,\text{TeV}$, from [AND12a].

Model	Yield (0-10% central)	Yield (0-80% central)
Quark coalescence	8.2×10^{-3}	2.05×10^{-3}
Hadron coalescence	3.8×10^{-2}	9.5×10^{-3}
Statistical model	3.2×10^{-2}	8.0×10^{-3}

Table 2.2: Comparison of results from the ExHIC Collaboration [EXP11] for different models for the H-Dibaryon of central Pb–Pb collisions at top LHC energy of $\sqrt{s_{\mathrm{NN}}} = 5.5\,\mathrm{TeV}$. The last column shows the value divided by 4 to have the value for the later comparison.

2.3.2 Coalescence model

Another model to describe the production probabilities of particles is the coalescence model. Particles can form by coalescence from passing quarks (quark coalescence model) or hadrons of a similar momentum in the collision region or the cool down from the fireball. It is not obvious that such an idea can be used, especially if one compares the chemical freeze-out temperature and the binding energies of particles, e.g. the deuteron has a binding energy of 2 MeV and a freeze-out temperature of 164 MeV. But the dominating thermodynamic variable is the entropy, to be more precise it is the entropy per baryon for this process, see for instance [AND11, STE12] and references therein.

Carl Dover [DOV91] introduced an easy way to estimate the production of the H-dibaryon at AGS, where its search was also of particular interest. In this ”conservative” estimation method other production processes, except the hadronic coalescence mechanism are neglected. The model works very well for non-strange nuclei, i.e. the production of deuterons, tritons and helium at the AGS [KAH96, ARM00]. The produced number of clusters $N(A,S)$ of baryon number A and strangeness S is given by

$$N(A,S) = \frac{N(A,S)}{N(A,0)}\frac{N(A,0)}{N_\alpha}N_\alpha\,.$$

This can now be translated into a penalty factor P for adding baryons

$$\frac{N(A,0)}{N_\alpha} \approx P^{A-3}\,,$$

and a strangeness suppression factor λ for added strangeness content

$$\frac{N(A,S)}{N(A,0)} \approx \lambda^{|S|}\,.$$

The strangeness suppression factor λ can be obtained from the Λ/p ratio, which is $\lambda = \frac{30.0|_{0-5\%}}{36.3|_{0-5\%}} \approx 0.83$ measured at Pb–Pb collisions at 2.76 TeV at the LHC.

The penalty factor P can be estimated from the ratio d/p measured in ALICE to be around 0.0035 for 0-5%, since the deuteron yield in the this centrality class is 0.127 and the proton yield 36.2873±1.988. Using the formula of Carl Dover we expect a yield of

$$\frac{\mathrm{d}N}{\mathrm{d}y}_{\text{H-Dibaryon}} = \left(\frac{\Lambda}{p}\right)^2 \frac{d}{p}\frac{\mathrm{d}N}{\mathrm{d}y}_p = 0.83^2 \times 0.0035 \times 36.3 = 0.0875 \approx 8.8\times10^{-2}\,.$$

$$\frac{\mathrm{d}N}{\mathrm{d}y}_{\Lambda\mathrm{n\ bound\ state}} = \left(\frac{\Lambda}{p}\right)\left(\frac{d}{p}\right)\frac{\mathrm{d}N}{\mathrm{d}y}_d = 0.83 \times 0.0035 \times 36.3 = 0.105 \approx 1.1\times10^{-1}\,.$$

The hadronic coalescence picture can also be extended to a quark coalescence picture. One active group in this area is the ExHIC Collaboration [EXH11], which made predictions for a numerous set of exotic states. They calculated expected yields for hadron and quark coalescence, but for the expected top LHC energy of $\sqrt{s_{\mathrm{NN}}}$ =5.5 TeV [EXP11]. The expected H-Dibaryon yields are compiled in Table 2.2, where all values are calculated by them inclusive the statistical model prediction. Their statistical model calculations are based on [AND06], namely they use the assumptions discussed in 2.3.1. But one has to admit that they assume a quite low freeze-out temperature T_F of 125 MeV and a critical temperature T_c of 175 MeV. Whereas the hadron coalscence takes place at T_F and the statistical and the quark coalscence are connected to T_c in their model.

Chapter 3

ALICE

3.1 ALICE apparatus

The Large Hadron Collider (LHC) [LHC08] is currently the largest collider in the world located at CERN, Geneva, with a circumference of 27 km. Lead ions and protons are pre-accelerated in the accelerator complex at CERN before being injected into the LHC with an energy of up to 450 GeV. A schematic view of the acceleration complex is shown in figure 3.1. Protons are first accelerated in LINAC2 and then injected into the Proton Synchrotron (PS) to gain more energy. From the PS the protons are injected into the Super Proton Synchrotron (SPS) and finally into the LHC. For the Pb–Pb runs in 2010 and 2011 the lead was accelerated in the LINAC3 accelerator and then in the Low Energy Ion Ring (LEIR) before entering the PS. The LHC provided different collision energies over the last years of running with $\sqrt{s}$: 900 GeV, 2.36 TeV, 2.76 TeV and 7 TeV for protons. Pb–Pb collisions happened at $\sqrt{s_{\mathrm{NN}}} = 2.76\,\mathrm{TeV}$ and recently a pilot run with proton on lead collisions was done at a center-of-mass energy of 5.01 TeV.

ALICE (A Large Ion Collider Experiment) [AAM08] is one of the four big experiments hosted at the LHC, its layout is shown in the schematic view of Fig. 3.2. It has a size of $26 \times 16 \times 16\,\mathrm{m}^3$ and a weight of about 10000 t. The magnetic field of up to 0.5 T, in the so-called central barrel, is provided by the L3 magnet. This allows the momentum measurement from the curvature of the charged tracks in the magnetic field. The geometric acceptance window of the central barrel is $|\eta| \leq 0.9$ while in the muon spectrometer the geometric acceptance is in the range $-4 < \eta < -2.5$.

ALICE is a general purpose detector with the ability to track and identify particles with transverse momenta down to 100 MeV/c. The analyses described in the following make only use of the central barrel, therefore only this is discussed here. In the central barrel a wide range of detectors, utilising all known particle identification techniques, are available to allow a very good particle identification in a wide momentum range. They are discussed going from close to the beam-pipe towards the magnet.

3.1.1 Inner Tracking System (ITS)

The ITS [AAM08] is a silicon detector setup consisting of two layers of silicon pixel detectors (SPD), two layers of silicon drift detectors (SDD) and two layers of silicon strip detectors (SSD). The ITS is optimized for efficient track finding and high vertex and impact-parameter resolution. The high resolution vertex determination is crucial for charm and beauty physics. The resolution of about 60 μm allows the determination of secondary vertices from weak decays of those. The main aim of the ITS is vertexing and tracking but it also provides particle identification for the low-p_{t} region starting at $\approx 100\,\mathrm{MeV}/c$ via

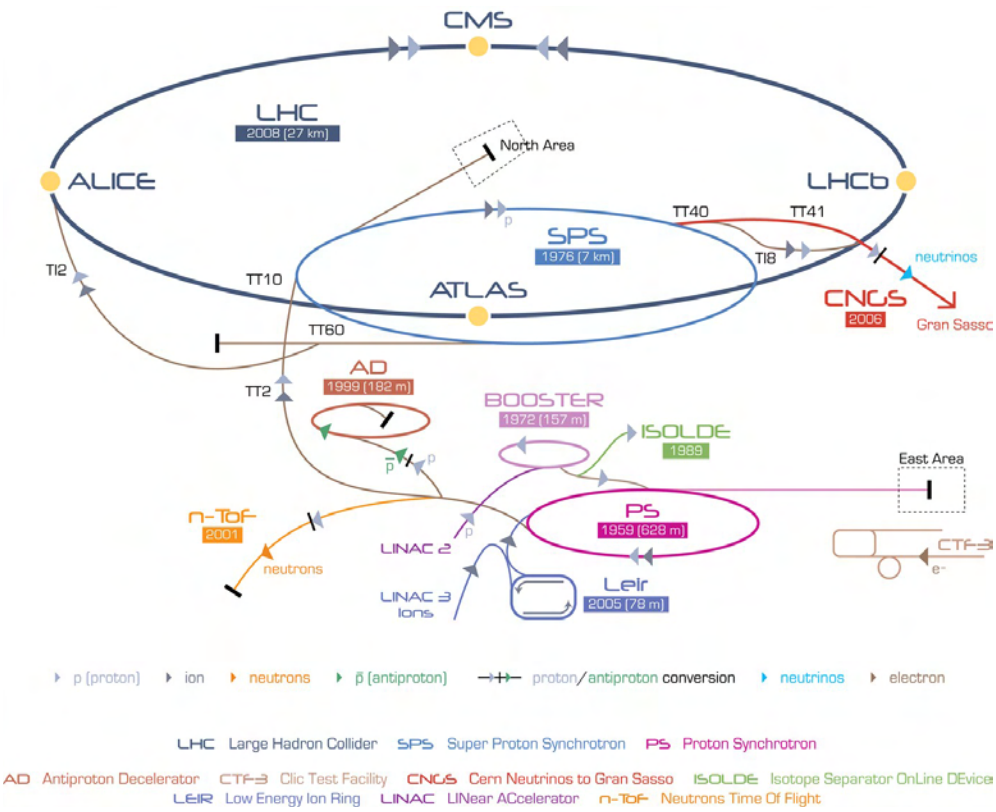

Figure 3.1: LHC accelerator complex [LHC08].

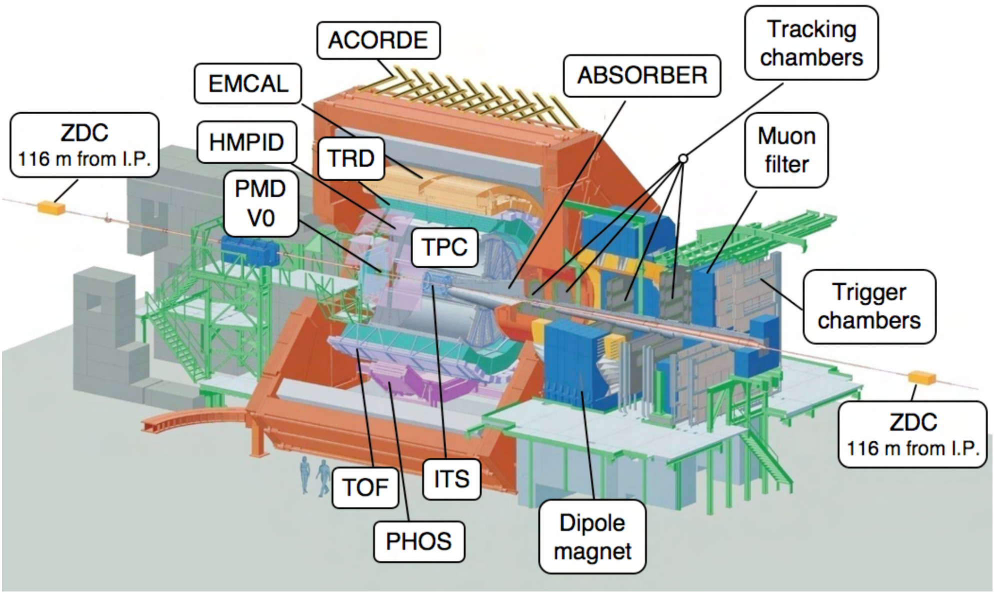

Figure 3.2: Schematic view of the ALICE setup [AAM08].

specific energy loss dE/dx (described by the Bethe-Bloch formula). The ITS performance is shown in Fig. 3.3 and a clear seperation of protons from pions is possible for momenta up to nearly 1 GeV/c.

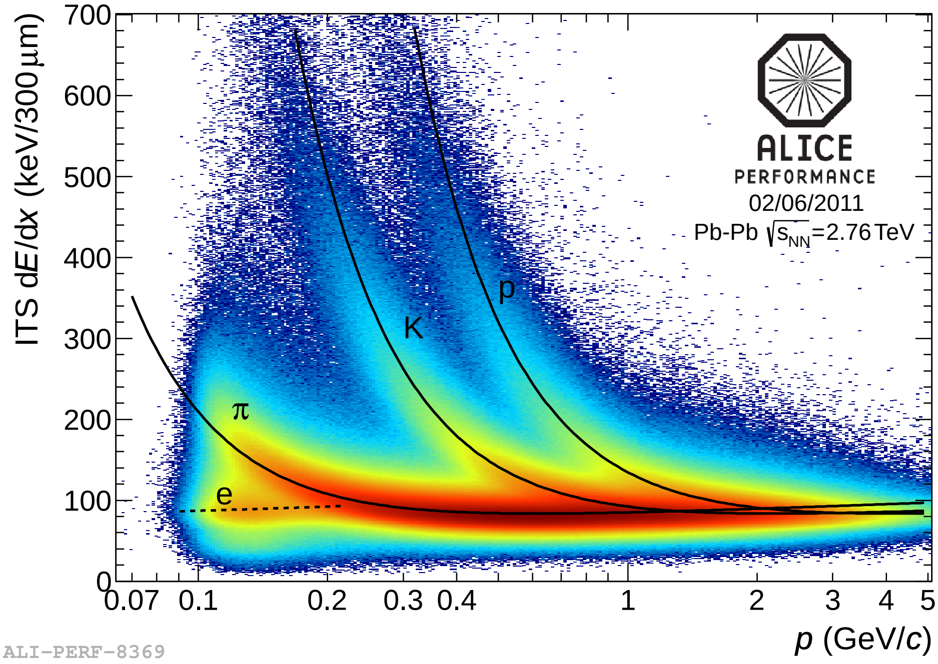

Figure 3.3: ITS specific energy loss versus particle momentum.

3.1.2 Time Projection Chamber (TPC)

The TPC [ALM10] is the main tracking detector in ALICE. It provides three dimensional tracking of the traversing particles. The TPC also allows particle identification (PID) via specific energy loss dE/dx. Charged particles traversing the gas volume ionize the gas atoms along their way and loose a given amount of energy per unit track length, which is different for each particle species.

A schematic view of the TPC is shown in Fig. 3.4. One can see that the central electrode divides the drift region in two parts. One is pointing into the direction of the muon arm and the other opposite to it. The two sides of the central electrode are facing the endplates, where the read-out chambers are placed. The gas volume itself is build by the field cage and the read-out chambers and create a volume of around $90\,\mathrm{m}^3$ which is filled with a mixture of Neon and CO_2 (90%/10%). It was filled for parts of the data taking (until end of 2010) with in the proportions of Ne/CO_2/N_2 (90%/10%/5%). The central electrode provides a high voltage of 100 kV with about 400 V/cm field strength to transport the main charges towards the read-out chambers. The end-plate area is split in the radial direction into two parts, an inner part and an outer part. This leads to the naming of the read-out chambers, which are called IROCs and OROCs (Inner- and Outer- Read-Out Chamber). They are segmented in phi direction into 18 sectors whereas the inner and outer readout chambers have different pad densities. Each chamber is a Multi Wire Proportional Chamber (MWPC) with cathode pad readout. In total the TPC has 557568 pads and samples the collision over the drift time of $\approx 100\,\mu$s. Since the primary electrons from the ionization are not able to induce a signal which is large enough to be detected an amplification is needed. This is done in the amplification region near the anode wires, where an avalanche effect is generated. Further a gating

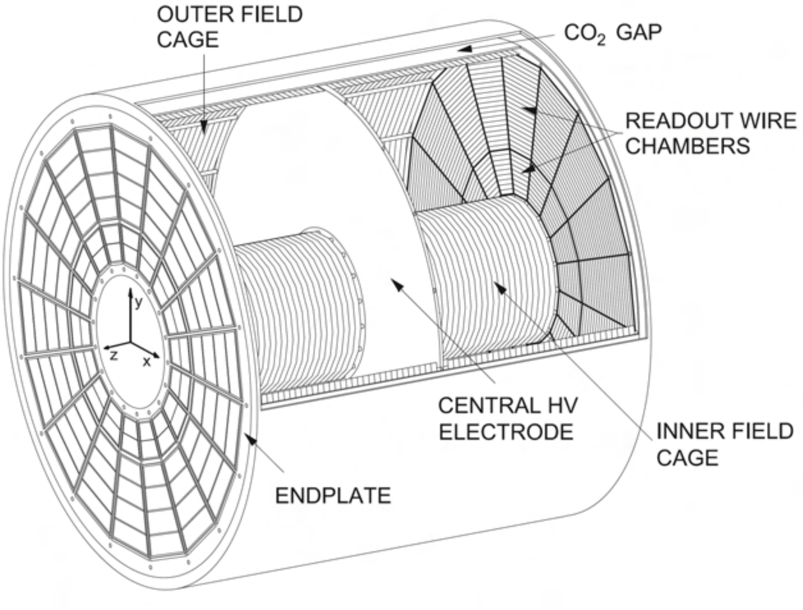

Figure 3.4: Schematic view of the ALICE TPC [ALM10].

grid is added to separate the drift region from the amplification region, such that ions are hindered to distort the drift field.
The particle identification capabilities are shown from the specific energy loss dE/dx in Fig. 3.5. The excellent dE/dx-resolution is between 5-8 % depending primarily on the sample length of the track, but also slightly on the multiplicity of the event.

3.1.3 Transition Radiation Detector (TRD)

The TRD [AAM08, DÖN07] is segmented into 18 sectors aligned with the TPC sectors. Presently, 13 out of 18 supermodules are installed. Each of the sectors will contain one supermodule built up from five stacks (counted from 0 to 4) in beam direction each filled with six Multi-Wire Drift Chambers (MWDCs). These sit on top of each other building 6 layers, counted from 0 to 5. The total TRD will consist of 522 MWDCs ($15 \times 30 + 3 \times 24 = 450 + 72 = 522$), three supermodules will leave holes for another detector (PHOS)) when it will be completed. For the first year of data taking (2010) 7 supermodules were installed. In the winter shutdown 2010-2011 further three supermodules were moved in and commissioned in the spaceframe. Finally in the winter shutdown 2011-2012 three further supermodules were installed. Each detector module contains a radiator followed by a drift region with a gas containing 85% Xe and 15% CO_2. Anode wires are mounted before the pad readout. The TRD uses the effect that a charged particle emits a typical radiation when it crosses the interface of two media of different dielectric properties. This effect depends strongly on the relativistic Lorentz γ-factor ($\gamma = E/mc^2$). For electrons of 3 GeV it is $\gamma \approx 5870$, while it is only $\gamma \approx 21$ for pions of the same energy. This allows the seperation from electrons to hadrons.
The TRD is designed to trigger on electrons and dielectrons, mainly to provide a hardware trigger on heavy quarkonia (J/ψ and Υ). It also provides fast ($6\,\mu$s) triggering capability for high transverse momentum charged particles ($p_t > 3\,\mathrm{GeV}/c$).
The TRD performance is shown in Fig. 3.6. On the left part it shows the TRD signal for pions and

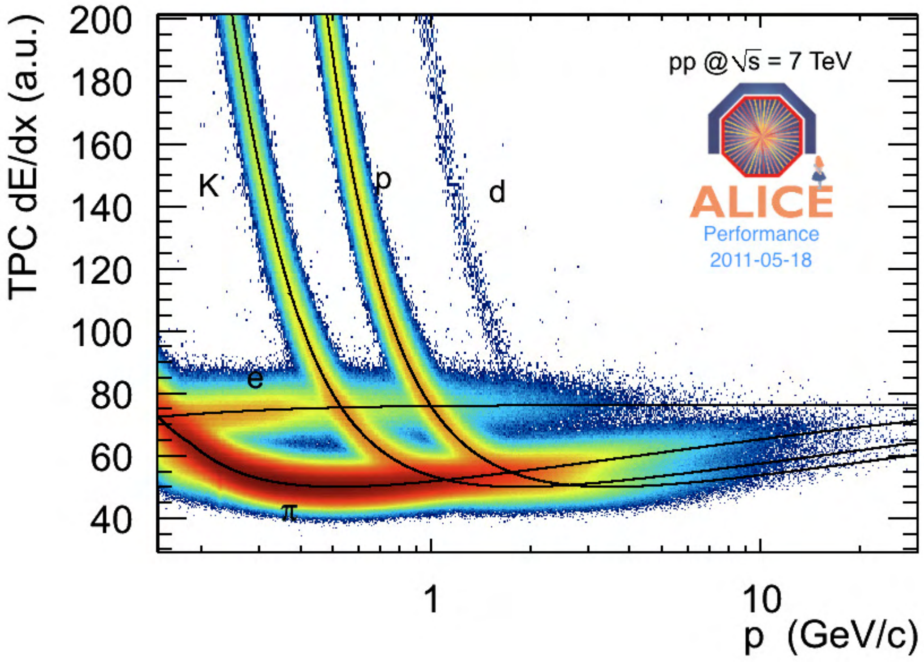

Figure 3.5: TPC dE/dx performance versus momentum p.

electrons (of $p = 2\,\mathrm{GeV}/c$) from measured data in pp collisions at $\sqrt{s} = 7\,\mathrm{TeV}$, compared with testbeam data. On the right part the TPC signal in number of σs for expected electrons with and without utilisation of the TRD is shown.

A large fraction of my time as doctoral student was spent on the TRD itself. I was involved in three parts: TRD Front-End Electronics (FEE) integration, TRD pretrigger and some time was spent connected to the gas system. These parts will be described in more detail in the following.
My diploma thesis was related to the assembly and the tests of the first supermodule. All integration steps are described in detail in [DÖN07]. After the first supermodule was assembled, tested and installed (the assembly was completely done in Heidelberg), the steps of the integration were split upon the collaborating institutes, namely:

Institute	**Task**
Physikalisches Institut (PI), Heidelberg	Test of ROBs, hardware and software for pre-trigger
Kirchhoff Institut für Physik (KIP), Heidelberg	TRD trigger part
Institut für Kernphysik (IKF), Frankfurt	FEE integration
GSI	FEE integration
Institut für Kernphysik, Münster	Integration of ROCs into SMs
CERN	Tests of the supermodule and commissioning

TRD FEE

The main component of the ALICE TRD FEE is the Multi-Chip Module (MCM). It consists of two chips: the PASA (PreAmplifier and ShAper) and the TRAP (TRAcklet Processor). The steps of each part of the FEE processing chain are shown in Fig. 3.7. The electronics allows to decide online if the

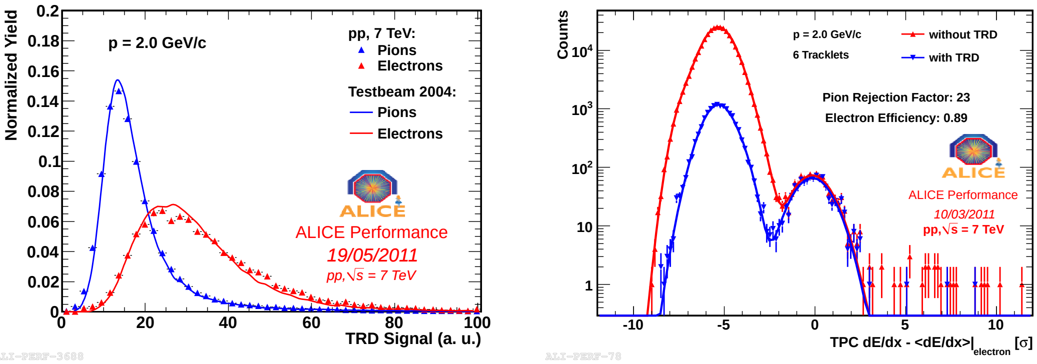

Figure 3.6: Measured TRD signals for pions and electrons in pp collisions at $\sqrt{s} = 7\,\mathrm{TeV}$ compared with testbeam data (left). TPC dE/dx signal in number of σs for expected electrons with and without utilisation of the TRD (right). Both at $p = 2\,\mathrm{GeV}/c$.

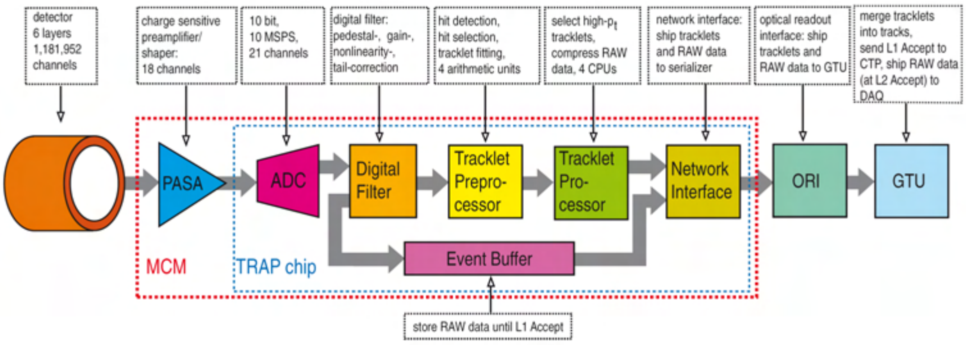

Figure 3.7: The TRD electronics process chain, taken from [AAM08].

tracked particle is an electron and ships its decision via Optical Readout Interface (ORI) to the Global Tracking Unit (GTU).

The MCMs are soldered onto Read-Out Boards (ROBs), specially developed printed circuit boards. Depending on the position in a supermodule, 6 to 8 of these ROBs are grouped together on one chamber. They process the charge reaching the pad plane towards the MCMs. The MCMs then deliver the data to the ORI which ships the data to the GTU. The whole processing chain needs careful testing while FEE integration.

For the FEE integration a test setup and the corresponding infrastructure had to be built. The infrastructure had to be close to the final environment at the ALICE cave.

Two personal computers formed the main part of the setup. One PC was used for networking and data readout. Networking here means it was providing a gate towards the GSI network and at the same time was providing the utilities for a subnetwork of GSI (the trd.net network). The second PC was mainly providing the test software for the FEE and was able to compile the software for the DCS (Detector Control System) board, which main component is a FPGA (Field Programmable Gate Array) that had to be programmed, respectively flashed. Two databases are necessary, one for the communication and acknowledgement channels (a mysql database) and a database containing the FEE parts and where they are mounted (an Oracle database).

The communication to the DCS boards is possible in two ways: The DCS boards utilize a small linux operating system which can be accessed via ssh (secure shell), or through the intercomlayer, a communication based on a protocol developed at CERN which is called DIM (Distributed Information Management system).
For this communication a so-called feeserver is running on each DCS board. This feeserver gets encoded commands from the PC via the intercomlayer. Those are interpreted then by the Control Engine (CE). Quite some work was connected with the continuous development of the CE and the feeserver of the pretrigger DCS boards.

Pretrigger

During data taking, the TRD electronics requires an early wake-up signal from the forward detectors (VZERO and T0) and/or the fast (TOF) detector. This wake-up signal is called pretrigger.
The pretrigger is needed to keep the power consumption of the TRAPs low until a proper signal is observed and the electronics is switched on.
In the ALICE design the global hardware trigger has three levels: level 0 (L0), level 1 (L1) and level 2 (L2). The TRD pretrigger has three input detectors which are also used as L0 input to the Central Trigger Processor (CTP). In a physics event which is finally read out by all participating detectors all three levels have to be passed.
The delay for the pretrigger signal is 700 ns from the interaction up to the arrival at the front-end electronics. This corresponds to an arrival of the L0 of the CTP of above 900 ns. This means the electronics can process 2 pre-samples, since the electronics uses 100 ns timebins. When a pretrigger arrives at the MCMs, they start to reconstruct tracklets (the track fragment within one of the six layers of the TRD drift chambers) which are then shipped via an optical link to the GTU if no L0 reject is given within a certain time window. The GTU then starts to combine the tracklets to tracks and identifies electrons with high transverse momentum: a local TRD level 1 trigger accept is issued and sent to the CTP. A scheme of the pretrigger system is shown in Fig. 3.8.

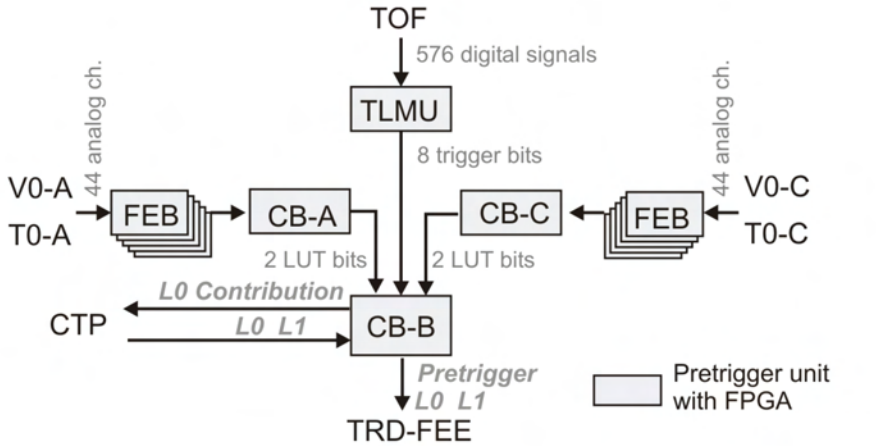

Figure 3.8: Schematic view of the TRD pretrigger setup.

The pretrigger system consists of 5 front-end boxes (FEBs) and one control box (CB-A/CB-C) on each side. Further a control box combining the signals from CB-A and CB-C and the TOF (CB-TOF) related trigger decision is part of the design. The FEBs are programmed via JTAG (Joint Test Action Group) connection through CB-A/CB-C and are controlled via Slow Control Serial Network (SCSN). The CBs itself are controlled via DCS boards which sit on the control box board and are accessible through ethernet. To fulfill the strict timing requirements the signals of the forward detectors VZERO and T0 are directly fed into the FEBs and used to perform a trigger decision in the FPGA of CB-A/CB-C, independently. The CB-A/CB-C trigger decision is then combined with the trigger decision of the control box for the TOF part of the pretrigger system. A final decision is then taken by another FPGA and in case of a true event the pretrigger is provided to the electronics via optical fibres to each DCS board of the TRD. It is also sent to the CTP of ALICE as the L0 input from the TRD. For the analysis of the trigger efficiency, the signals from each VZERO/T0 channel and the signals from each FEB at the level of CB-A/CB-C and CB-TOF are counted, independent of the trigger decision. The CB-TOF has been used to sent pretrigger signals to the TRD electronics in cosmic runs, which allowed calibration and alignment of these detectors [HUB10].

Gas system

The ALICE TRD is using a gas mixture of Xenon and CO_2 and has, when it is completed, a total gas volume of $28\,\mathrm{m}^3$. Each supermodule has an own gas control line (except the three lowest and the three uppermost chambers which are fed by one line). The whole gas system allows the purification and liquidification of the Xenon. This system is necessary because Xenon is one of the rare and therefore also expensive gases. Thus, as little as possible of it should be lost. Xenon has to be taken to provide efficient transition radiation photon absorption (because the photon absorption cross-section in the keV-regime scales with Z^5), whereas CO_2 is used as quenching gas. This means the total gas system has also to be quite gas tight.

In November 2007 a beam test was done at CERN PS with a complete supermodule. Previous to this only beam tests with prototypes or in 2004 with a complete stack, but not with the final electronics, happened. During the beam test in 2007 a huge gas leak was discovered (see also [EMS09]). This led to cross checks of the gas tightness of all produced chambers (since it was pinned down to the leakage of a single chamber). The already installed supermodules were pulled back out of the spaceframe and disassembled. Each chamber was filled with helium and possible leaks were searched for. If a leak was found it had to be closed with the appropriate glue.

The main source of the leaks was identified to come from a honeycomb support structure which is directly glued on the pad plane. The gas is creeping towards this honeycomb structure. Therefore it was decided to close the possible gas exits in the honeycomb. The final measurements of the gas leakage of each chamber showed that the current total leak rate is below the design value.

3.1.4 Time-Of-Flight detector (TOF)

The TOF [AAM08] detector is also split into 18 supermodules like the TRD. It utilises MRPC (Multi-gap Resistive Plate Chambers) technology for the measurement of the flight time t_{flight}. This is given by $t_{\mathrm{flight}} = t_{\mathrm{hit}} - t_0$. Where the start time is measured either by the T0 detector, which will be described shortly after this detector. Or from a global time minimization from the fit of the particle distribution reaching the TOF detector itself, if the number of tracks reaching the TOF is large enough (≥ 3). Another option makes use of the average t_0 from the LHC fill, when the other two possibilities are not available. The mass can be calculated from $m = \frac{p}{c}\sqrt{\frac{c^2 t_{\mathrm{flight}}^2}{L^2} - 1}$, where the length L, the momentum p

and the t_{flight} are measured. Instead of the momentum p very often the rigidity $R = \frac{p}{z}$ is used. This leads to $m^2/z^2 = R^2/(\gamma^2 - 1)$.

The TOF detector consists of 1638 multi-gap resistive plate chambers. They provide an intrinsic resolution of approximately 80 ps. Since the overall time resolution for particle identification also depends on the t_0 uncertainty of the event, the TOF resolution is determined by $\sigma_{TOF} = \sqrt{\sigma_{intr}^2 + \sigma_{t0}^2}$. With this one gets $\sigma_{TOF} \approx 86$ ps for Pb–Pb collisions and $\sigma_{TOF} \approx 120$ ps for pp collisions. This allows a 2σ-separation between protons and kaons up to 5 GeV/c. The performance for Pb–Pb data taken in 2011 is shown in Fig. 3.9, where $\beta = \frac{v}{c}$ is drawn versus the momentum p.

TOF also provides a wake-up signal (pre-trigger) input for the TRD which can be used as a cosmic trigger or a trigger on diffractive events.

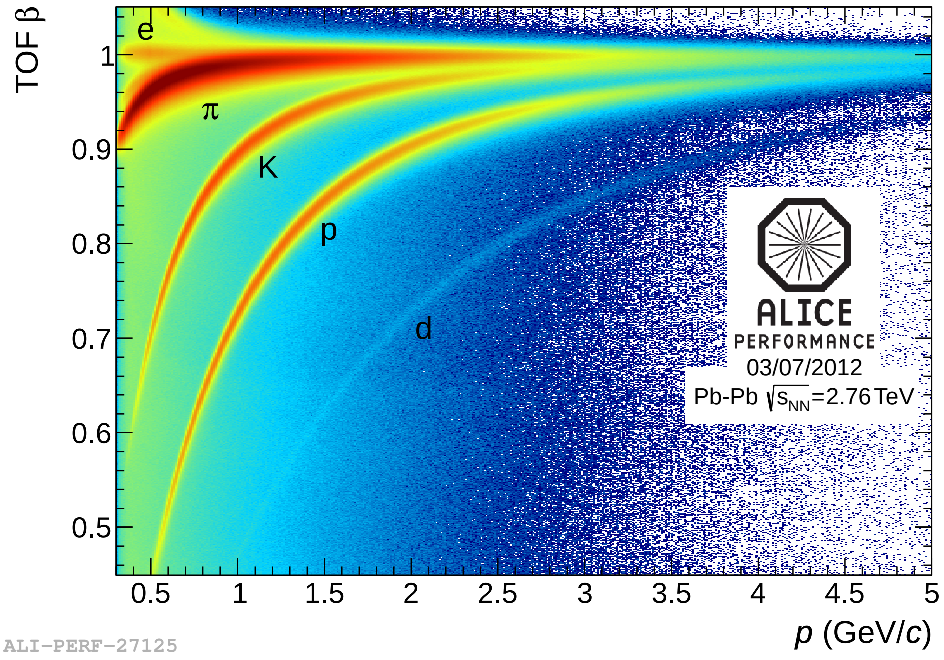

Figure 3.9: TOF β versus p, the clear separation of hadrons is visible.

3.1.5 T0

The T0 detector [AAM08] is built to generate time related signals for the whole ALICE trigger chain. It has to produce the t_0 signal for the TOF detector, which corresponds to the real time of the collision (plus a fixed time delay). It also has to provide a pretrigger signal to the TRD, prior to the L0 level. Since the T0 detector generates the earliest L0 trigger signals, they must be very fast. The dead time of the detector has to be less than 25 ns which corresponds to the bunch-crossing period in pp collisions (25 ns). The T0 consists of two arrays of 12 Cherenkov radiators optically coupled to photo-multiplier tubes, surrounding the beampipe on two sides relative to the interaction point.

3.1.6 VZERO

The VZERO detector [AAM08] has to provide a minimum bias trigger for the central barrel detectors. It also provides centrality triggers in lead-lead collisions, i.e. triggers for minimum-bias, semi-central and central events. It can be used as a centrality indicator in multiple roles. It can also be used for a validation signal for the muon trigger to filter background in pp collisions. The VZERO is a small-angle detector consisting of two arrays of scintillator counters. The VZERO time resolution is better than 1 ns, allowing discrimination of beam-beam collisions from background events produced upstream of the experiment.

3.1.7 VZERO and centrality selection

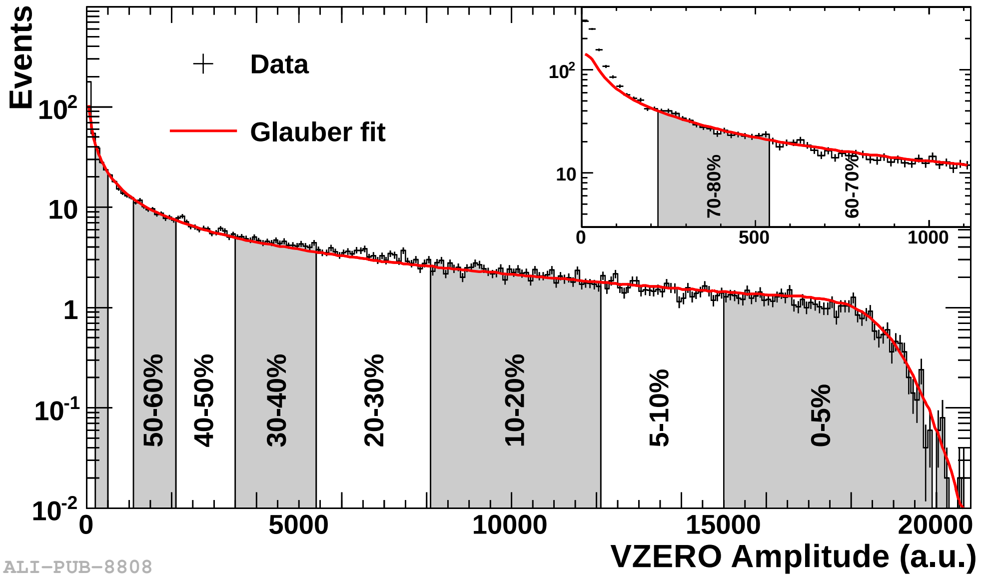

Figure 3.10: Different centrality classes from the measured distribution of the VZERO amplitude.

Also the offline centrality selection in ALICE can be done utilising the VZERO detector. This is used in the analyses which will be discussed later. Figure 3.10 shows the measured distribution of the VZERO amplitudes. The red line fitting the measurement comes from a Glauber model [GLA53]. It is a two-component model which assumes that the number of sources which produce particles is given by

$$f \times N_{\text{part}} + (1-f) \times N_{\text{coll}} .$$

Here N_{part} is the number of nucleons which participate in the collision, N_{coll} is the number of binary nucleon-nucleon collisions and f a measure of their relative contributions. The number of particles produced is modeled by a negative binomial distribution. It is parametrized through μ and κ, where κ gives control on the multiplicity distribution tail and μ is the mean multiplicity of each source. The negative binomial can be written as

$$P_{\mu,\kappa}(n) = \frac{\Gamma(n+\kappa)}{\Gamma(n+1)\Gamma(\kappa)} \frac{(\mu/\kappa)^n}{(\mu/\kappa+1)^{n+\kappa}} .$$

The full fit is then performed using $P_{\mu,\kappa}(n) \times f \times N_{\text{part}} + (1-f) \times N_{\text{coll}}$.
From this the centrality classes are determined by integrating the measured distribution and split into different percentiles as shown in Fig. 3.10.

Chapter 4

Strange baryons

4.1 Λ particle

We discuss here mainly the Λ, since it is one of the particles which has to be reconstructed to be able to finally detect the H-Dibaryon, which search is the major part of this thesis. We also discuss briefly particles which can be detected by using the reconstructed Λs when they are combined with charged pions or photons.

The Λ baryon, also called Λ hyperon, has a mass of (1115.683 ± 0.006) MeV and a $c\tau = 7.89$ cm. It is measured in ALICE in the $p\,\pi^-$ channel which has a branching ratio of $(63.9 \pm 0.5)\%$ [PDG12]. The reconstruction of this channel makes use of the fact that the Λ has a special decay topology, the so called V0 topology. Since the Λ is neutral and lives relatively long it produces no visible track in the tracking detectors until it decays and leads into two visible tracks of opposite signed charged tracks. These two tracks form the shape of a V, starting at the decay vertex of the Λ. V0s have been discovered in 1947 by G.D. Rochester and C.C. Butler [ROB47] in a cloud-chamber by observing exactly this special topology. This was the first observation of neutral kaon decays. The Λ was first observed in 1950 by V. D. Hopper and S. Biswas in photographic emulsions [HOP50].
For the detection of these V0s two approaches are followed in ALICE. Either the entire event is checked offline for tracks which show a V0 topology or already while the tracks are reconstructed were the tracking algorithm searches for V0 candidates. These are the so called Offline and the On-the-Fly V0 finders.

4.1.1 Offline V0 finder

From the taken data (one should admit that the algorithm(s) are developed on Monte Carlo events) first a set of reconstructed tracks is build. The procedure for finding proper V0 candidates then starts with the selection of secondary tracks. These tracks should not have too small impact parameter with respect to the primary vertex. Then tracks with opposite charge are combined. Further cuts on the positive and the negative track's impact parameter are applied. Then pairs of tracks are rejected if the distance of closest approach (DCA) between the two tracks is larger than a given value. The minimization of the distance between the tracks is performed numerically using a 3-dim helix track parametrization [ALI06]. From this process a secondary (decay) vertex is obtained, whereas only the vertices inside a given fiducial volume are kept. The inner boundary of this fiducial volume is limited by the expected particle density and the tracking precision which, in turn, is mainly defined by the multiple scattering on the pixel layers of the ITS. The V0 finding procedure finishes with checks whether the momentum of the V0 candidate points well back to the primary vertex. For this the two corresponding tracks are extrapolated to the

points of the DCA and the V0 momentum is calculated as the sum of the track momenta taken at those points. Then a cut on the cosine of the angle (pointing angle) between the V0 momentum and a vector connecting the primary vertex and the V0 vertex positions is applied [ALI06].
Depending on the size of the fiducial volume one can reduce a huge amount of background and reach a good significance. But at the same time the efficiency drops dramatically. This has to be adjusted by the used cuts.

4.1.2 On-The-Fly (online) V0 finder

The online reconstruction algorithm of a V0 is done similar to the offline V0 finding algorithm. But since it is applied while the track is calculated the track properties can be used, i.e. the full material and the magnetic field are known while the tracks are propagated, which is the main difference to the offline V0 finder. It starts with the identification of possible daughter tracks with a similar algorithm as the offline V0 finder and using their properties to calculate the characteristics of a possible mother particle. The daughter tracks are identified already while each track is reconstructed and is done by cutting on the distance of the daughter tracks to the primary vertex, the distance of closest approach DCA between the daughter tracks and the pointing angle Θ_{pointing}. The momentum of the mother particle should point to the primary vertex. Further a causality check is performed. This means the absence of space points in forbidden ITS layers can be required if the decay takes place far enough from the vertex. This shows that the on-the-fly finder depends strongly on the performance of both: TPC and ITS.

4.2 Λ reconstruction

The reconstructed momenta of the V0 candidates using either offline or on-the-fly V0 are then used to calculate the invariant mass assuming the positive particle to be a proton and the negative to be a pion. But since the candidates are built for findable V0 decays they do not just consist of true Λ, but also contain true K^0_S and $\overline{\Lambda}$ and γ (which have been converted into $\mathrm{e}^+\mathrm{e}^-$ pairs) decays. They give a significant contribution to the invariant mass of the Λ which is shown in figure 4.1. To remove these so-called reflections several ways are possible:

- tuning of the topological cuts,
- usage of particle identification,
- cuts in the Armanteros-Podolanski space.

The topological cuts are chosen to be quite open, to not cut to deep into the signal. The strongest cut (strong in the sense of removing most background but keeping at the same time most of the signal) is the cut on the cosine of the pointing angle (angle between the reconstructed flight line of the Λ and the vector between the primary and the decay vertex).
The particle identification, utilizing a $\mathrm{n}\sigma$ cut on the $\mathrm{d}E/\mathrm{d}x$ in the Time-Projection Chamber, helps a lot to remove fake Λs. But since electrons cross pions at momenta of around $100\,\mathrm{MeV}/c$ and protons at around $1.0\,\mathrm{GeV}/c$, and at higher momenta also protons and pions are becoming harder to disentangle, there are still fakes left.
The Armenteros-Podolanski space [ARM53] is spanned by the relative asymmetry of the momenta of the two decay products coming from a V0 decay and the transverse momentum of the mother. Each particle species describes the shape of an ellipse in the Armenteros-Podolanski space.
Cutting on the Armenteros-Podolanski space has to be done very carefully, similar to the topological cuts one can cut into the signal without knowing. This cut is used mainly for the cleanup. A further

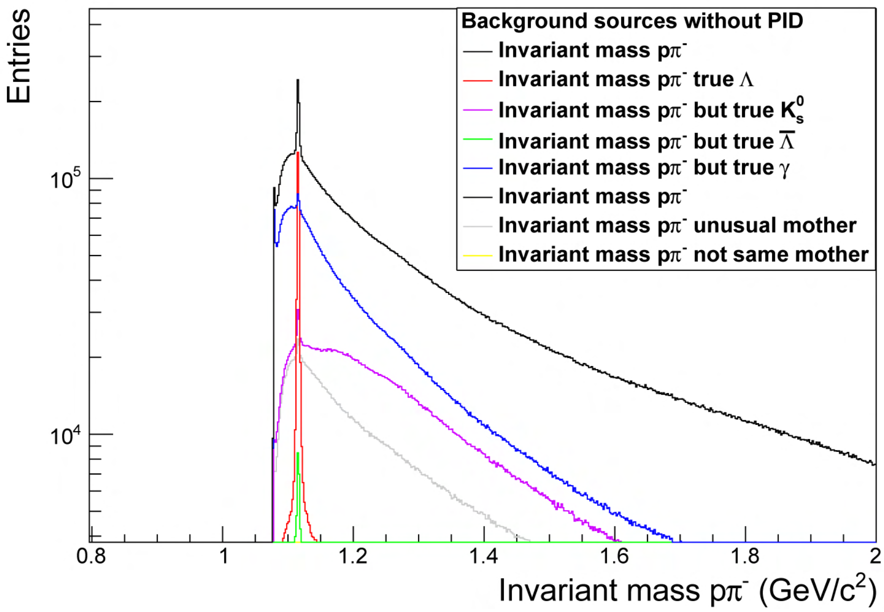

Figure 4.1: Different background sources of the reconstructed Λ invariant mass from a Monte Carlo simulation.

method is to cut on the invariant mass of the unwanted particles. Which lead to white spaces in the Armenteros-Podolanski plot, see Fig 4.2.

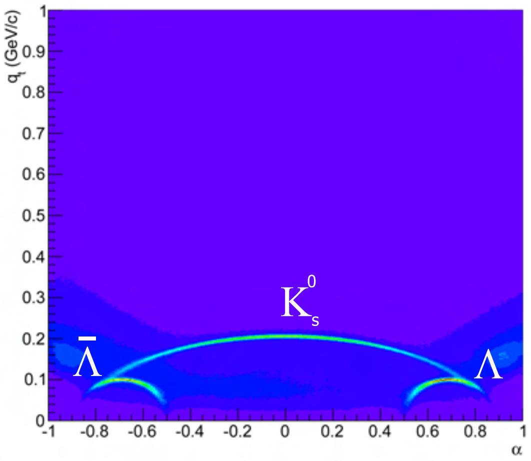

Figure 4.2: Armenteros-Podolanski plot, where the ellipses for Λ, $\overline{\Lambda}$ and K_s^0 are visible.

The final invariant mass plot after applying all cuts (Tab. 4.1) is shown in figure 4.3

These cleaned up Λs are then used for the further combination with particles within a 3σ region around the peak.

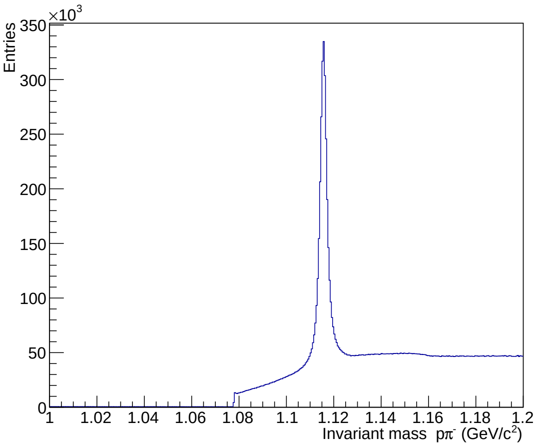

Figure 4.3: Reconstructed Λs in pp collisions at $\sqrt{s} = 7$ TeV.

4.3 Ξ^- and $\Sigma(1385)$ signal

To cross-check the results of an analysis done in the ALICE resonance group and to confirm the quality of the selcted Λs (selected from the cuts described in the previous section) we also performed studies on the $\Sigma(1385)^+ \to \Lambda\pi^+$ and the $\Sigma(1385)^- \to \Lambda\pi^-$ which is interesting because if one does not constrain the cuts too much onto particles from the primary vertex, also the Ξ^- becomes visible in the invariant mass distribution. This is shown in Fig. 4.4 for the $\Lambda\pi^-$ invariant mass for a subset of the pp data at 7 TeV.

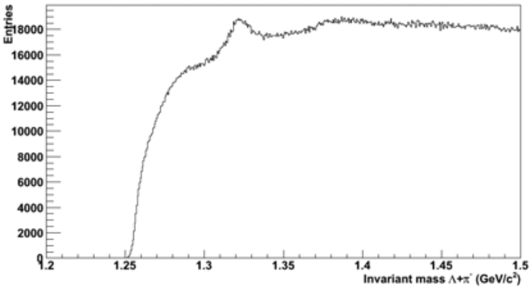

Figure 4.4: Invariant mass of $\Lambda + \pi^-$, showing the Ξ^- at 1.319 GeV/c^2 and the $\Sigma(1385)$ as a broad structure with the mean at 1.385 GeV/c^2.

4.4 Σ^0 measurement

The measurement of Σ-Hyperons might help to understand the issue raised by the proton yield in Pb–Pb collisions which is not well described by the thermal model. Therefore we performed first studies in pp collisions which should be continued soon in Pb-Pb.

The easiest experimentally accessible Σ-Hyperon is the Σ^0. First attempts have also been started in ALICE to look for the Σ^+ (51.6% $\Sigma^+ \to p\pi^0$), where the more problematic part is the π^0 measurement. Whereas π^0 decays via $\pi^0 \to \gamma\gamma$ in $\approx$ 100% [PDG12]. But the Σ^- (99.94% go into $\Sigma^+ \to n\pi^-$) is by the current ALICE setup inaccessible, since neutrons are not detectable with the central barrel detectors.

The Σ^0 decays electromagnetically into $\Lambda\gamma$ and this by a branching ratio of nearly 100%. The Λ reconstruction is described in 4.2.
The main task to get a Σ^0 is the detection of the photon. For this ALICE offers two methods:

- Electromagnetic calorimetry (two different arrays of electromagnetic calorimetry are available, but both only cover a small range of acceptance), and
- Photon conversions into dielectrons (at $\approx 8\%$ conversion probability).

The second was preferred since it covers a larger area of acceptance and at the same time the most photons are soft and would not be easy to disentangle from background in the calorimeters.
The detection of the converted photon is making use of the V0 shape of the emitted e^+e^- pair. The detection is therefore similar to those of the Λ, described in 4.2. There the photons make a contribution to the background and have therefore to be removed. Here it is now opposite, we need the photons and have the Λ as possible background candidates. But we can use the same cut strategy as for the Λ, namely V0 cuts and background removal by particle identification (3σ cut on electrons in the TPC) and Armenteros-Podolanski cuts.
The reconstructed photons are shown in Fig. 4.5.

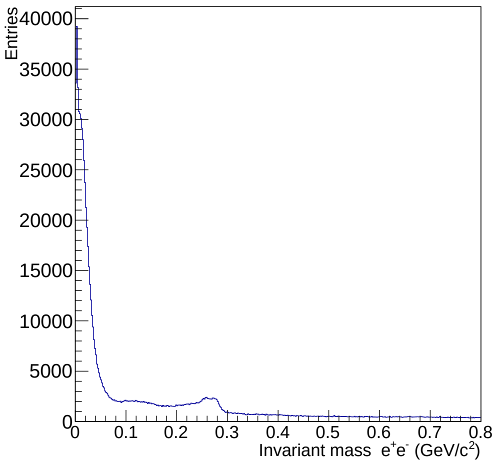

Figure 4.5: Invariant mass of $\gamma \rightarrow e^+e^-$. The peaks at around 150 MeV/c^2 and 275 MeV/c^2 come from wrongly identified protons and pions and corresponding to left over Λ and K_s^0 signal.

They are then combined with the detected Λ which leads to the invariant mass shown in Fig 4.6. The peak at 1.193 GeV/c^2 is the reconstructed $\Sigma^0 \rightarrow \Lambda\gamma$. The figure shows the complete data set of 2010 for 7 TeV pp collsions (close to 360 million minimum bias events).
A small Monte Carlo study has been done to estimate the Acceptance×Efficiency. But further studies, especially on the cuts are needed to be able to get yields and spectra for the Σ^0.

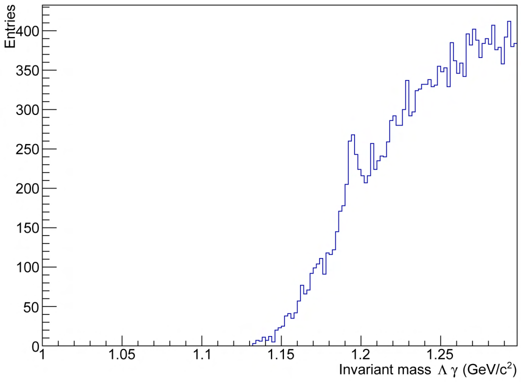

Figure 4.6: Invariant mass of $\Lambda\gamma$. The peak at 1.193 GeV/c^2 corresponds to the Σ^0.

cut	**value**
Track cuts	
Kink daughters	rejected
TPC	refit
n_{clusters}(TPC)	> 80
χ^2/cluster	< 5
$\lvert\eta\rvert$	≤ 0.9
V0 cuts	
dca V0 daughters	< 1 cm
dca positive V0 daughter - Vertex	< 1 cm
dca negative V0 daughter - Vertex	< 1 cm
Armenteros-Podolanski cuts	
q_t	$< -2.21\,\alpha^2 + 2.945\,\alpha - 0.887$
q_t	$> -2.21\,\alpha^2 + 2.945\,\alpha - 0.873$

Table 4.1: Optimised cuts used for the Λ reconstruction.

Chapter 5

$\Lambda(1520)$ measurement

The measurement of the $\Lambda(1520)$ is done concentrating on the pK^- channel which has a branching ratio of $\approx 22.5\%$ [PDG12]. The decay topology is shown in 5.1. Since it has a width of 15.6 MeV it lives only 12.6 fm/c, which makes it impossible to distinguish its decay vertex. For the measurement the decay happens already inside the fireball. This makes it a good candidate for signs of resonance-fireball interactions as re-scattering and regeneration [MAR03]. The identification of proton and kaon is done using the dE/dx information of the TPC and the time-of-flight TOF to be in a 3σ band in each detector. There was a comparison done combining the different available techniques, energy loss in ITS, TPC and flight-time measurement in TOF. The figure 5.2 shows the different combinations p_t integrated, the combinations using TOF are scaled by a factor of 180 to increase the visibility. From this study one can easily see that a pure particle identification using only energy loss in either TPC or ITS is not sufficient, at least if one looks for the p_t integrated signal.

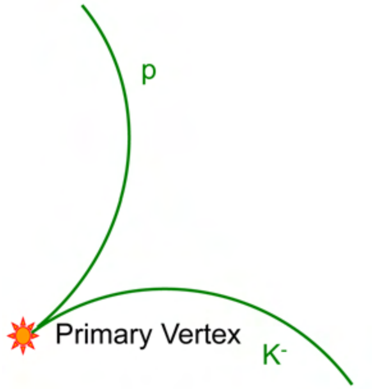

Figure 5.1: Decay topology of $\Lambda(1520) \to pK^-$.

There are several reflections visible on the TPC and the TPC+ITS PID options. These correspond to missidentified particles at larger momenta, especially pions are then also possible to be identified as kaons or even protons. Monte Carlo studies have been performed to identify the different reflection kinks and peaks which are becoming visible at 1.5 GeV/c^2, 1.56 GeV/c^2 and 1.62 GeV/c^2. They correspond mainly to K_s^0, $K^0(890)$ and $\rho(770)$.

The other used cuts are the single track cuts commonly used in the resonance analysis group in ALICE. All used cuts are grouped together in Table 5.1.

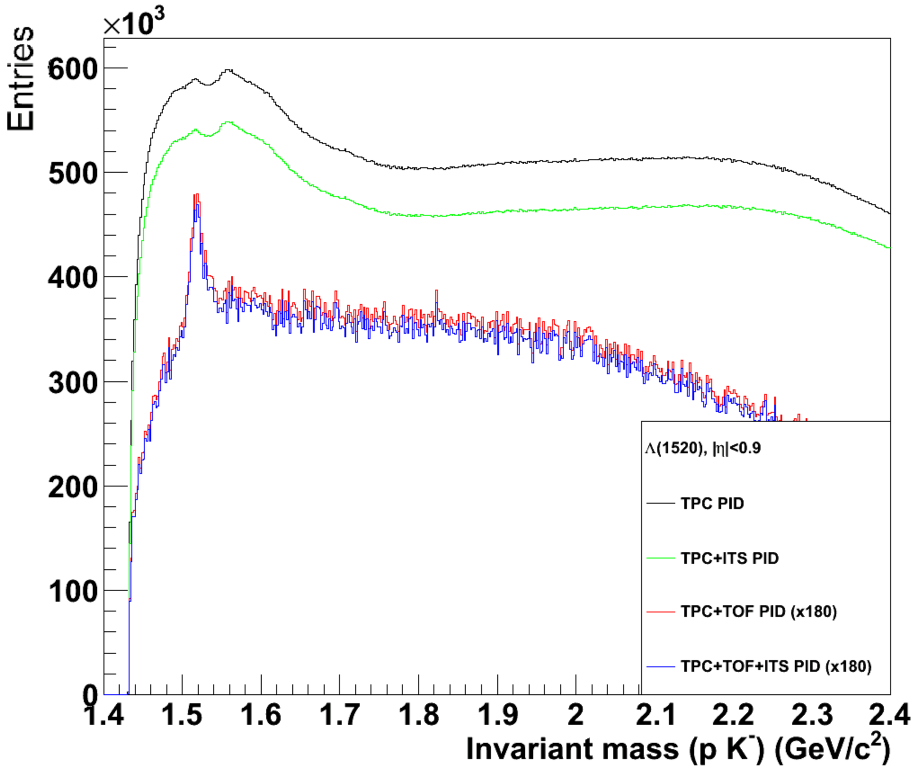

Figure 5.2: Different combinations of particle identification methods for the invariant mass reconstruction of pK^{-}.

One can see already from Fig. 5.2, that the signal sits on a huge amount of combinatorial background. To reduce errors on the signal extraction it is common to subtract the background. For this several techniques have been tried, such as like-sign, rotation, mixed events and the description of the background by mathematical functions. Rotation has lead to the worst results and was discarded already in the beginning of these studies.
The other techniques have been utilized to incorporate systematic effects on the signal extraction.

As a resonance the $\Lambda(1520)$ signal can be fitted with the shape of a Breit-Wigner function [BRE36], in their paper on the slow capture of neutrons Breit and Wigner established the following cross-section:

$$\sigma(E) = 4\pi\lambda(2l+1)\frac{\Gamma^2/4}{(E-E_R)^2+\Gamma^2/4},$$

where λ is the de Broglie wavelength, l the angular momentum, E the measured energy, E_R the energy at the resonance and Γ the width of the resonance. We use here in the following this version of the Breit-Wigner function:

$$\frac{\pi}{2}\frac{Y\Gamma(M_{K\mathrm{p}})^2}{(M_{K\mathrm{p}}-M_{\Lambda(1520)})^2+0.25\Gamma(M_{K\mathrm{p}})^2},$$

where $M_{\Lambda(1520)}$ is the mass of the $\Lambda(1520)$, $(M_{K\mathrm{p}}$ is the mass of the Kp pair, $\Gamma(M_{K\mathrm{p}})$ is the width of the Breit-Wigner and Y a free parameter to handle the height of the distribution.

cut	value
Single track cuts	
ITS	refit
Hits in ITS	at least 1 hit in SPD plus one anywhere else in ITS
TPC	refit
n_{clusters} (TPC)	> 70
χ^2/cluster (TPC)	< 4
DCA_z	$< 2\,\text{cm}$
DCA_{xy}	$< (0.0182 + 0.035/p_t^{1.01})\,\text{cm}$
$\lvert\eta\rvert$	≤ 0.8
Particle identification cuts	
K	in 3σ band in TPC and TOF
p	in 3σ band in TPC and TOF
Mother cut	
$\lvert y\rvert$	< 0.5

Table 5.1: Cuts used for the $\Lambda(1520)$ analysis

The invariant mass distributions for $\Lambda(1520)$ to pK^- at $\sqrt{s}$ =900 GeV and $\sqrt{s}$ =2.76 TeV are shown in Fig. 5.3. A complete analysis was only performed in the limits of this work for pp collisions at $\sqrt{s}$ =7 TeV and this will be discussed in the rest of this chapter.

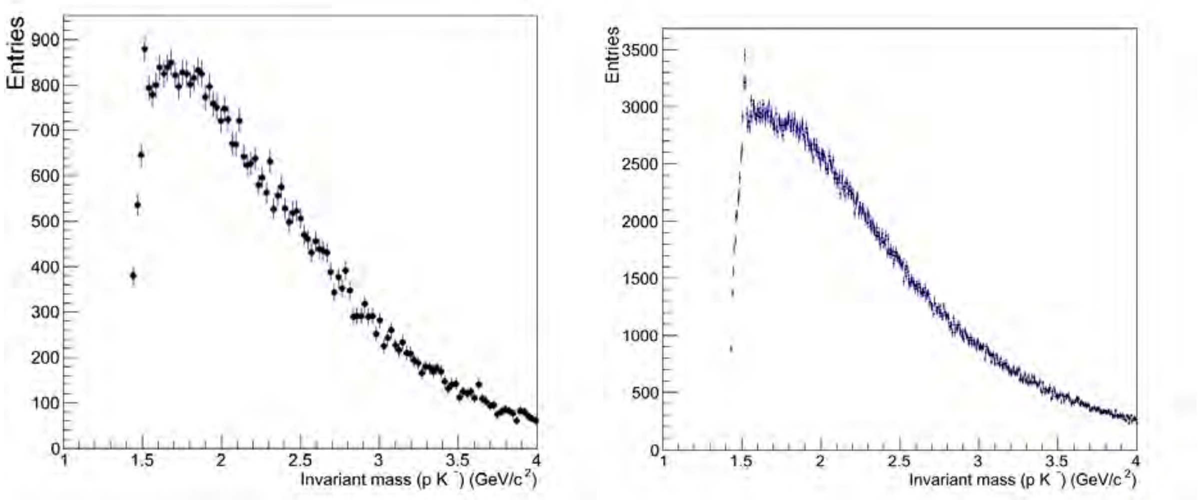

Figure 5.3: Invariant mass distribution for the $\Lambda(1520)$ to pK^- at $\sqrt{s} = 900\,\text{GeV}$ (left) and $\sqrt{s} = 2.76\,\text{TeV}$.

5.0.1 $\Lambda(1520) \rightarrow \mathrm{p}\,\mathrm{K}^-$ in pp collisions at 7 TeV

The large statistics of 2010 allows to split the $\Lambda(1520)$ in to 16 p_t-bins for $\Lambda(1520)$ and $\overline{\Lambda}(1520)$ separately, which was not possible for the previously performed experiments NA49 and STAR.

As main background description method the mixed event technique was utilized. Figure 5.4 shows an example p_t-bin of the invariant mass for pK^- from the same event in black and for mixed events in red.

Whereas Fig. 5.5 shows the example of the fit to the mixed-event subtracted signal. The fit function is chosen to be a third-order polynomial to describe the residual background shape and the signal shape is fitted by a Breit-Wigner.

The mixed events describe the background for lower p_t reasonably well but deviates quite strongly at higher p_t. This is currently under study in the ALICE resonance group but was not seen as a huge issue for the further analysis and the extraction of the yields. Most likely this difference is due to problems in the mixing framework. In addition to this, remaining background after the mixed events subtraction is taken care of with the third order polynominal.

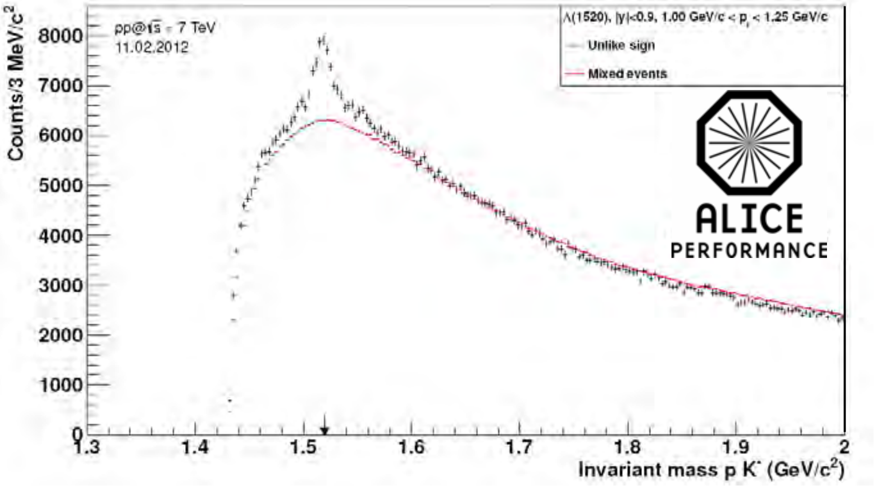

Figure 5.4: Example p_t-bin for the invariant mass of pK^- from the same event (black) and for mixed events (red).

The invariant mass distributions of same and mixed event for the different p_t-bins of the $\Lambda(1520)$ and the $\overline{\Lambda}(1520)$ are shown in Fig. 5.6, respectively Fig. 5.7.

After the subtraction of the mixed event from the same event invariant mass distribution in p_t bins, shown in Fig. 5.8 for the $\Lambda(1520)$ and in Fig. 5.9 the $\overline{\Lambda}(1520)$, all values like mass, width and yield can be extracted from the fit.
The raw yields extracted from the fit of the $\Lambda(1520)$ invariant mass in different p_t-bins are shown in Fig. 5.10. The systematic uncertainties are estimated from different particle identification combinations, namely the change from the standard value of 3σ to 1.5σ and 4σ, respectively.

5.0.2 Acceptance and Efficiency studies

For the estimation of the Acceptance and Efficiency of the measurement full Monte Carlo (MC) simulations have to be performed. Full here means the complete chain from the pp collision towards the interaction with detector (and/or support material) and the detection in the detector was simulated. The

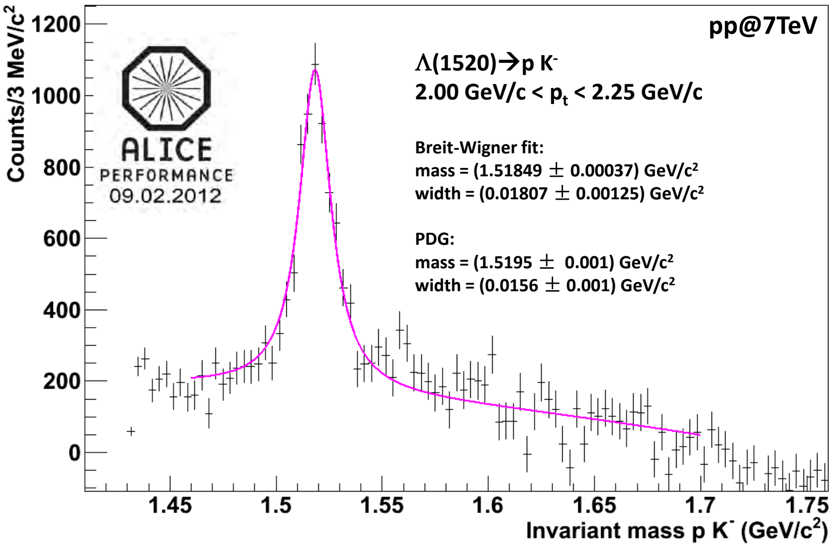

Figure 5.5: Invariant mass distribution for an example p_t-bin after mixed event subtraction for $\Lambda(1520)$ decaying to pK^-. The Breit-Wigner fit is shown in violet.

studies make use of the AliRoot framework which has interfaces via ROOT [ROOT] to Geant3 [GEANT] and PYTHIA [PYT06]. The $\Lambda(1520)$ is not implemented in the standard version of PYTHIA normally used for pp studies. Therefore it was necessary to implement the $\Lambda(1520)$ in the version used for the simulations. The reconstructed acceptance × efficiency is shown in Fig. 5.11. It is the result of the ratio of reconstructed $\Lambda(1520)$ and generated $\Lambda(1520)$.

To also correct for the anti-proton absorption of the $\overline{\Lambda}(1520)$ also Geant/Fluka corrections have been applied. The ratio of the extracted acceptance × efficiency for $\Lambda(1520)$ to $\overline{\Lambda}(1520)$ is shown in Fig. 5.12 and shows deviations mainly at low momenta, here the Geant/Fluka correction was applied.

5.0.3 Results and discussion for the analysis of the $\Lambda(1520)$

From the extracted mass of the $\Lambda(1520)$ we can see a deviation from the PDG value at low p_t in Fig. 5.13. It starts to agree within errors with the PDG value starting from a p_t of 0.75 MeV.
In comparison the extracted mass of the MC sample does not show this dependence. This behaviour is also seen in all other invariant mass analyses and is due to the worse description of energy loss for lower p_t particles.

The extracted width (Fig. 5.14) shows agreement with the PDG value for all used p_t-bins. The $\overline{\Lambda}(1520)$ shows the same behaviour for mean and width and is therefore not shown here.

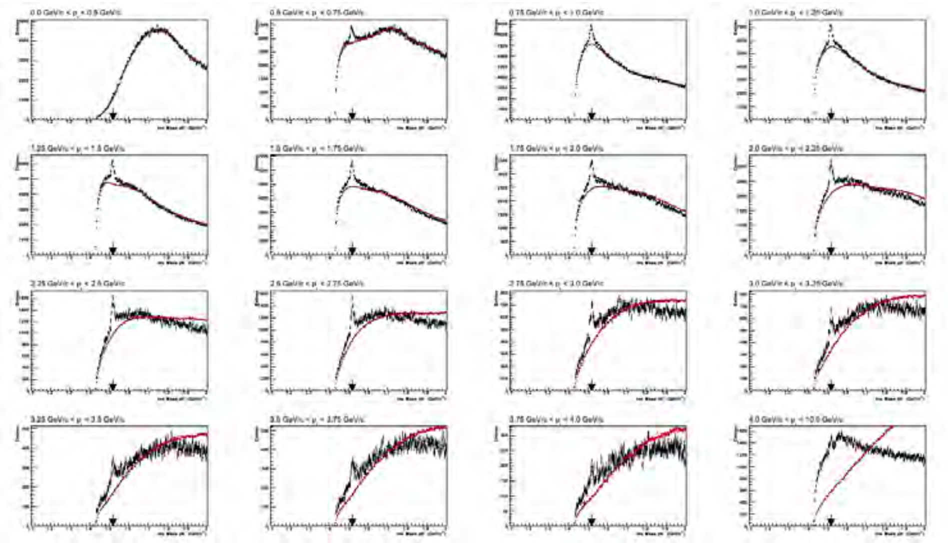

Figure 5.6: The 16 different p_t-bins for the invariant mass of pK^-.

The obtained raw yields are now corrected with the acceptance × efficiency from 5.0.2. They further need corrections for the trigger efficiency and correct normalisation. Thus the final spectra are obtained from

$$\frac{1}{N}\frac{d^2}{dydp_t} = \frac{1}{N_{used}} \times R_{norm} \times \varepsilon_{trigger} \frac{Y_{raw}}{Acc \times Eff} .$$

Here N_{used} is the number of analysed events, $\varepsilon_{trigger}$ the actual trigger efficiency and R_{norm} the normalisation coming from the different possible min. bias triggers, it is determined from Van-de-Meer scans performed for each LHC running period. Y_{raw} is the raw yield and $Acc \times Eff$ the acceptance × efficiency. The outcome is shown in Fig. 5.15 and Fig. 5.16 for $\Lambda(1520)$ and $\overline{\Lambda}(1520)$. The spectra are fitted with the Lévy-Tsallis distribution

$$\frac{d^2N}{dydp_t} = \frac{(n-1)(n-2)}{nT[nT+m(n-2)]} \times \frac{dN}{dy} \times \left(1 + \frac{m_t - m}{nT}\right)^{-n} ,$$

which describes the exponential shape at low p_t (characterised by an inverse slope parameter T) and the more power law behaviour at larger p_t (governed by the power parameter n) at once. It was used in previous analyses done at the ALICE experiment, see for instance [AAM11, ABE12c].

From the fit of the spectra we can extract the mean p_t

$$\langle p_t \rangle = (1.07 \pm 0.11)\,\mathrm{GeV}/c$$

and the yield per rapididty unit

$$\frac{dN}{dy} = 0.0089 \pm 0.0015 .$$

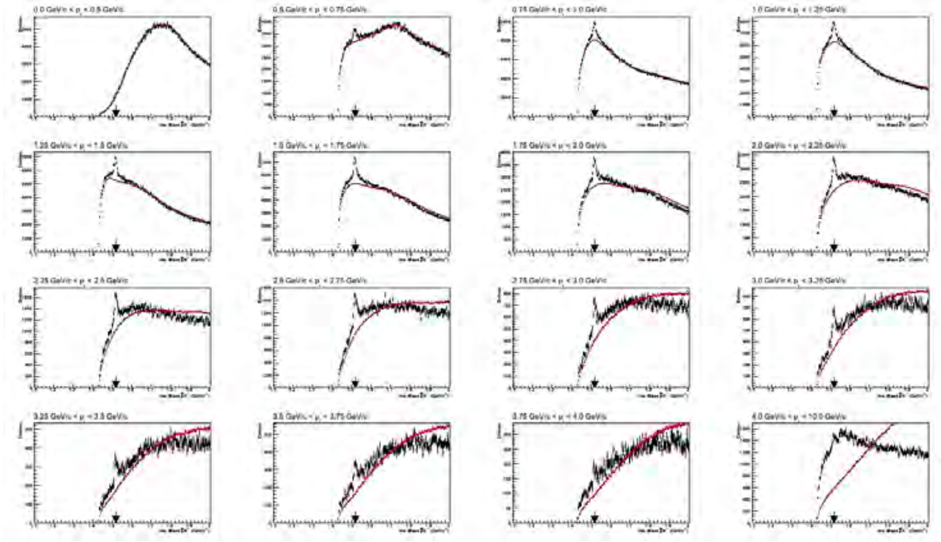

Figure 5.7: The 16 different p_t-bins for the invariant mass of $\overline{p}K^+$.

To compare this to previous experiments we calculated here the ratio of the yield of $\Lambda(1520)$ to the weakly decaying Λ (the yield is the preliminary ALICE value from a separate analysis [CHI12]). We get

$$\frac{\frac{dN}{dy}|_{\Lambda(1520)}}{\frac{dN}{dy}|_{\Lambda}} = \frac{0.0089}{0.093} = 0.0956 \pm 0.0211\,,$$

where STAR had a value of 0.093 ± 0.017 in pp collisions at 200 GeV [ABE05] and NA49 measured 0.109 ± 0.021 in pp collisions at 158 GeV [MAR00].

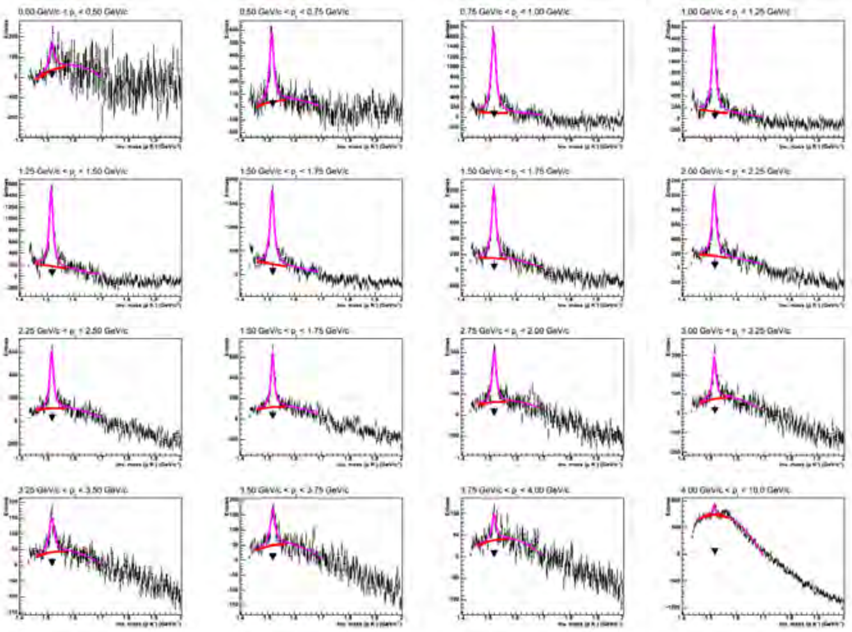

Figure 5.8: Invariant mass of pK^- after mixed event subtraction. The 16 different p_t-bins are fitted with a Breit-Wigner (purple) on top of a third-order polynomial (red).

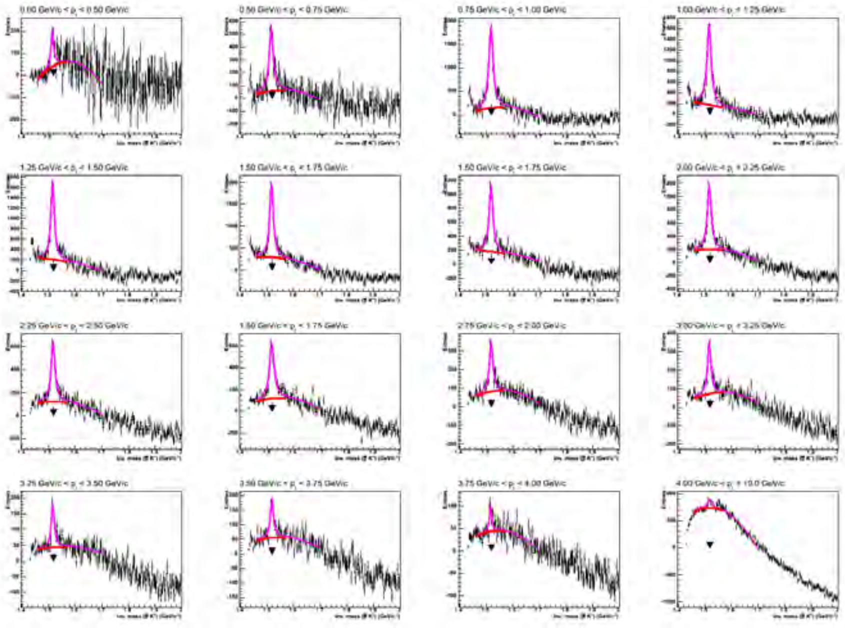

Figure 5.9: Invariant mass of $\overline{p}K^{+}$ after mixed event subtraction. The 16 different p_t-bins are fitted with a Breit-Wigner (purple) on top of a third-order polynomial (red).

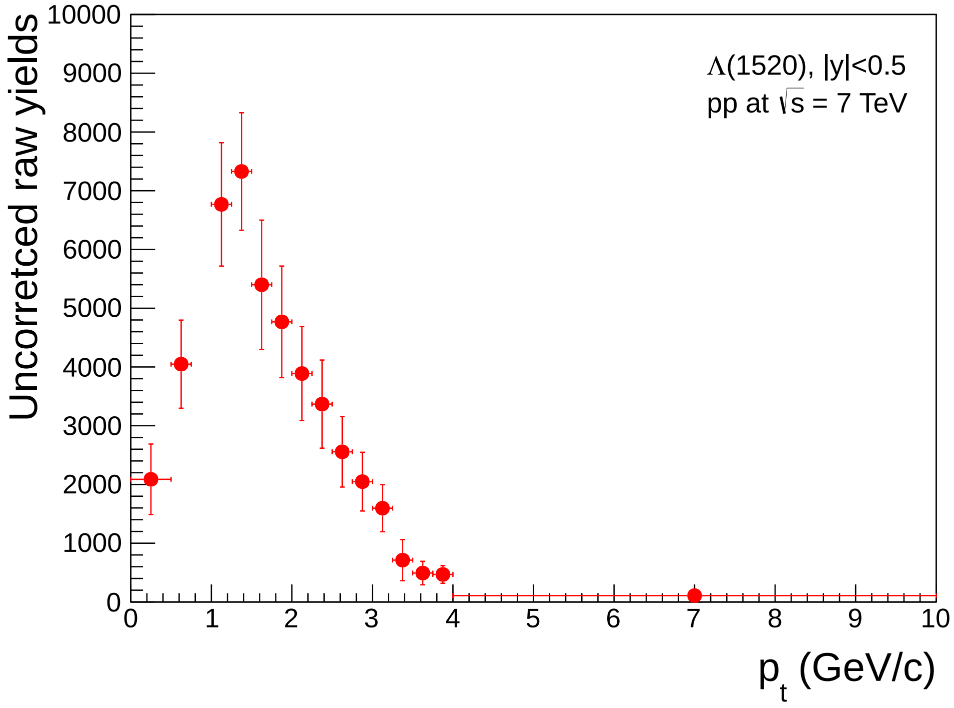

Figure 5.10: Extracted raw yields for the $\Lambda(1520)$.

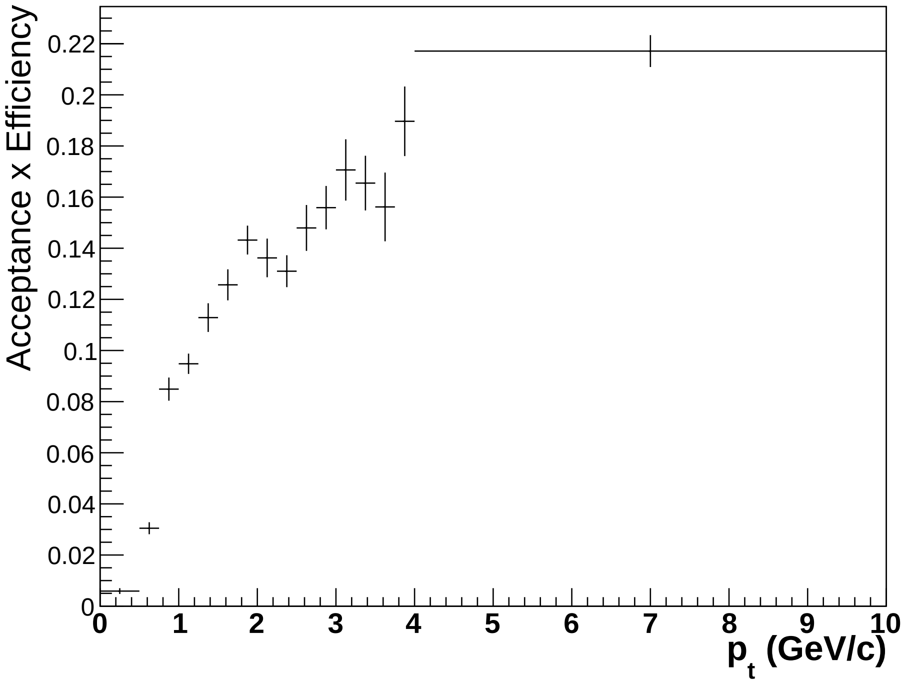

Figure 5.11: Acceptance × efficiency versus p_t for pK^-.

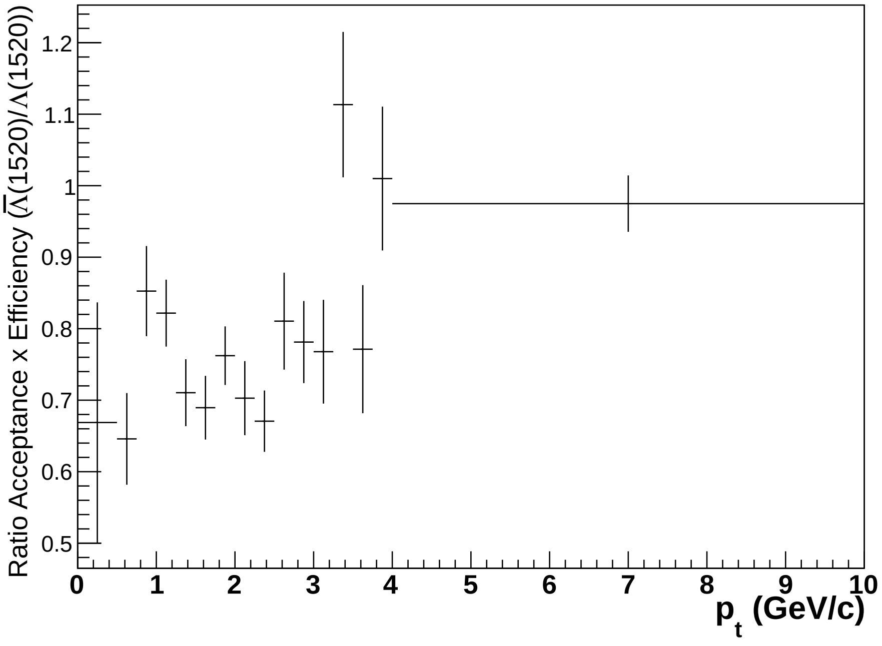

Figure 5.12: Ratio of the acceptance × efficiency for $\overline{\Lambda}(1520)$ to $\Lambda(1520)$.

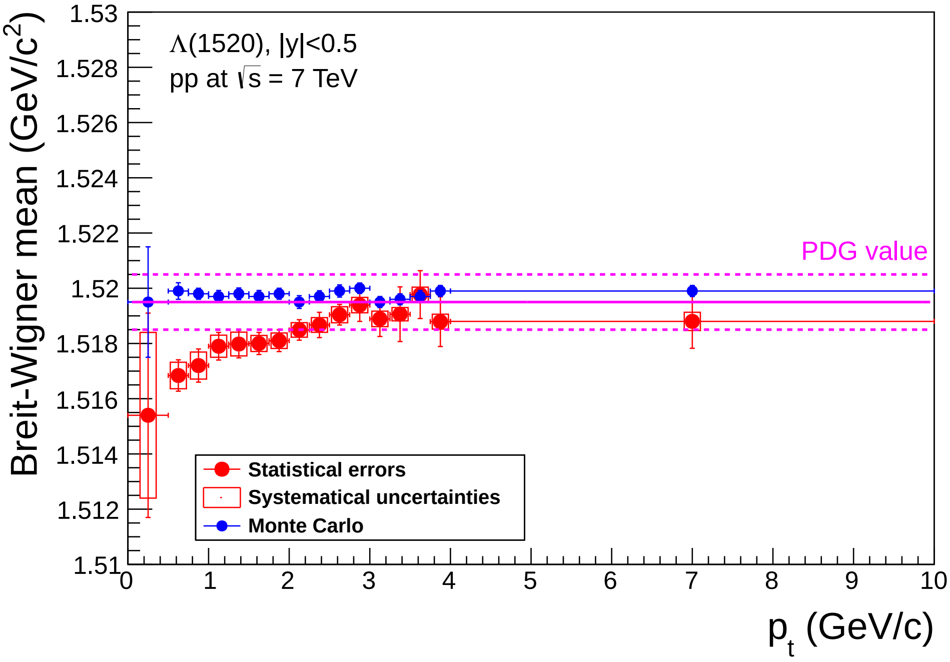

Figure 5.13: Extracted Breit-Wigner mean for the $\Lambda(1520)$.

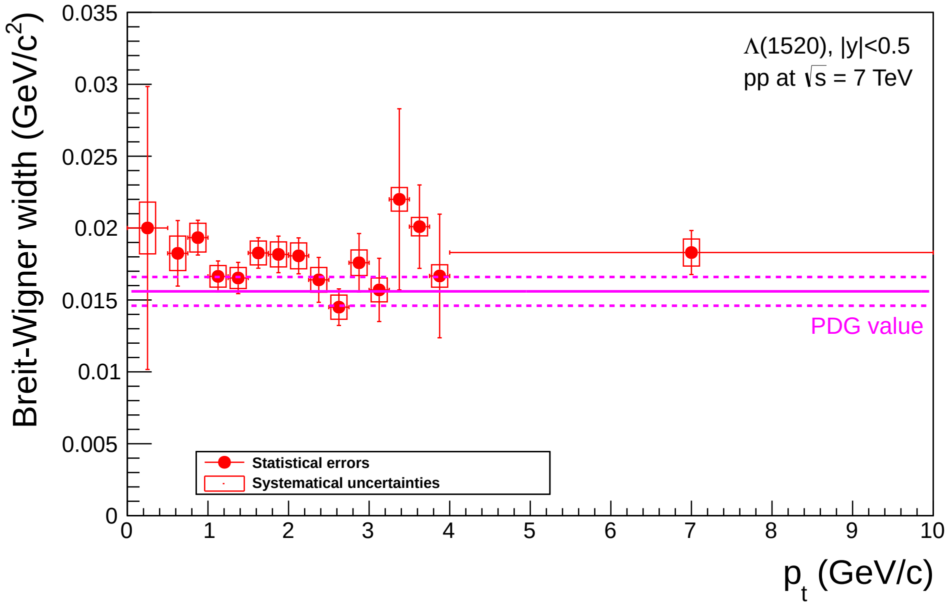

Figure 5.14: Extracted Breit-Wigner width for the $\Lambda(1520)$.

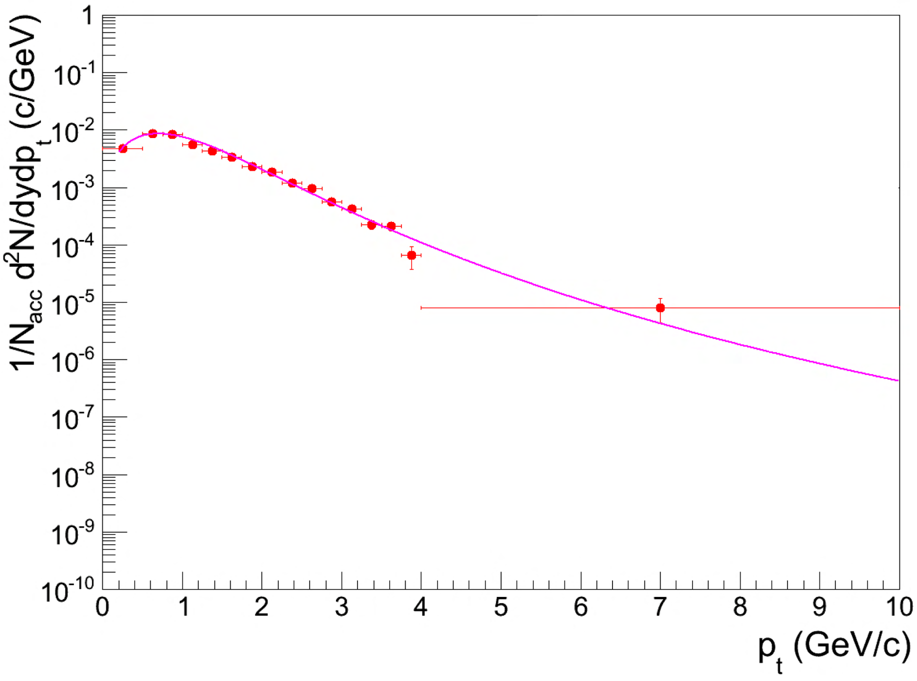

Figure 5.15: p_t spectrum for $\Lambda(1520)$ (only statistical errors) and a Lévy-Tsallis fit.

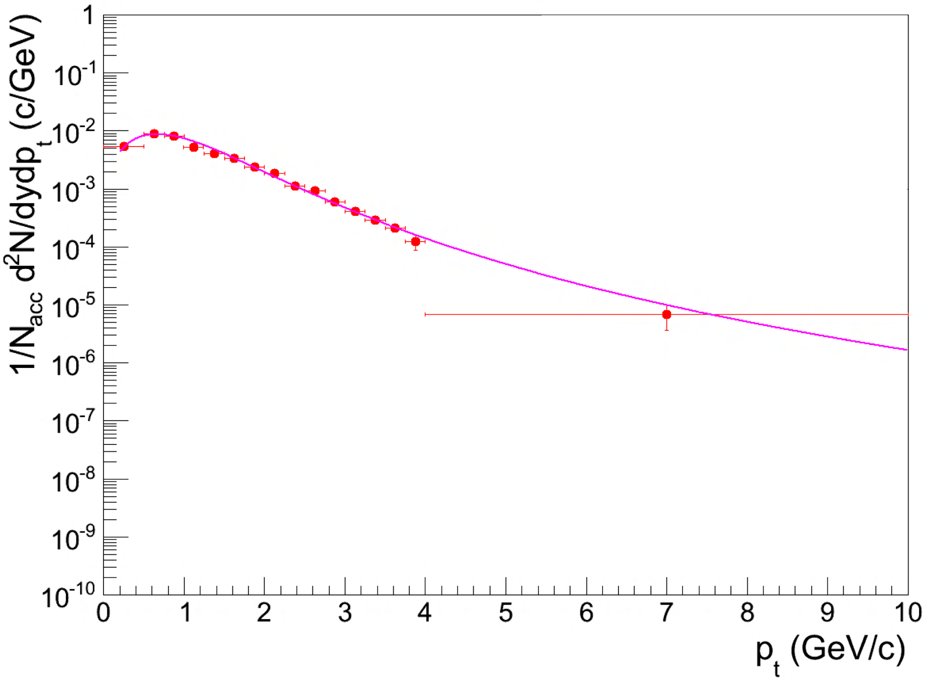

Figure 5.16: p_t spectrum for $\overline{\Lambda}(1520)$ (only statistical errors) and a Lévy-Tsallis fit.

Chapter 6

Exotica searches

We perform here two searches for exotic particles which both follow similar steps. First the search for the H-Dibaryon ($\Lambda\Lambda$ bound state) secondly the search for the Λn bound state. But before we can discuss those, we have to discuss shortly the analyses which are directly connected to these searches: The analysis of p, K, π, the analysis of light nuclei and the hypertriton, all are performed in Pb–Pb collisions at $\sqrt{s_{\mathrm{NN}}} = 2.76\,\mathrm{TeV}$. They are directly connected in the sense of being used as an input to the searches or show the physical capabilities of ALICE when these analyses are compared.

For all discussed analyses the following basic event selection have been used:

1. Physics selection for Minimum-Bias events;
2. Accept only events whose primary vertex falls within $< 10\,\mathrm{cm}$;
3. Accept only events whose primary vertex was not obtained solely through TPC tracking (rejecting events with zero contributors);
4. Centrality selection done using V0 of 0 to 80% (If possible splitted into smaller centrality bins).

6.1 Analysis of p, K, π and Blast-Wave fits

The p_t-spectra have been measured in ALICE with different particle identification techniques, for example utilising TPC and TOF [AKA12]. The measured spectra are corrected for acceptance × efficiency and then have to be properly normalised, like discussed in chapter 5. From this procedure p_t-spectra can be determined and in case of Pb–Pb collisions split into different centrality classes.
These spectra have to be fitted to get the final yields. The currently most used function to fit the spectra in A–A collisions is called blast-wave distribution [SCH93].

The blast-wave distribution is a simplified version of the relativistic hydrodynamic approach which can describe the collective expansion observed in heavy-ion collisions. It has three parameters: T_{fo}, β, n, i.e. a kinetic freeze-out temperature, a velocity parameter and a scale parameter to connect the radial and the transverse evolution of the system. A more complete description of this model can for example be found in [SCH93].
The model assumes a spectrum of purely thermal sources which are boosted in transverse direction. The velocity distribution in $0 \leq r \leq R$ is assumed to be

$$\beta_r = \left(\frac{r}{R}\right)^n \beta_s ,$$

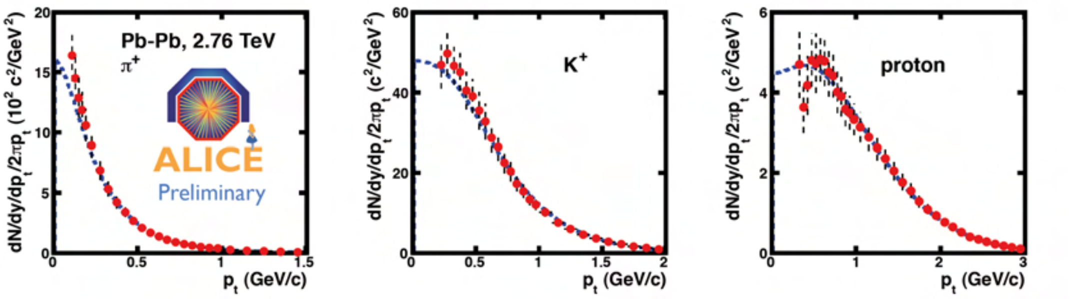

Figure 6.1: Blast-wave fit with a common parameter set to pion, kaon, and proton (π, K, p) spectra simultaneously in the 0-5% centrality class. From [SCH12].

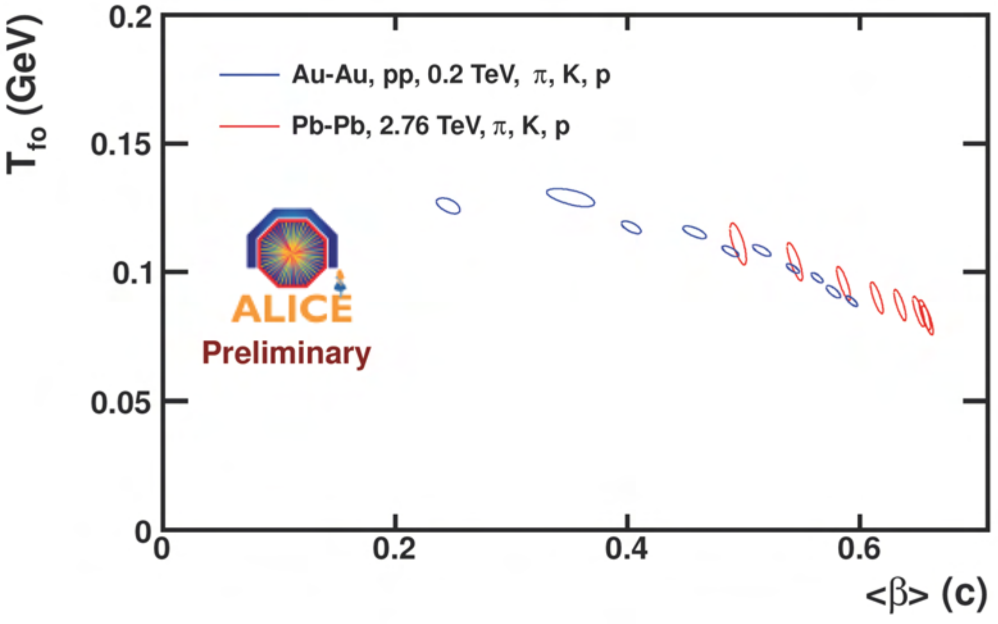

Figure 6.2: Resulting fit contours (1σ) for the kinetic freeze-out temperature and velocity for different centrality bins compared with the results of a similar analysis of RHIC data. From [SCH12].

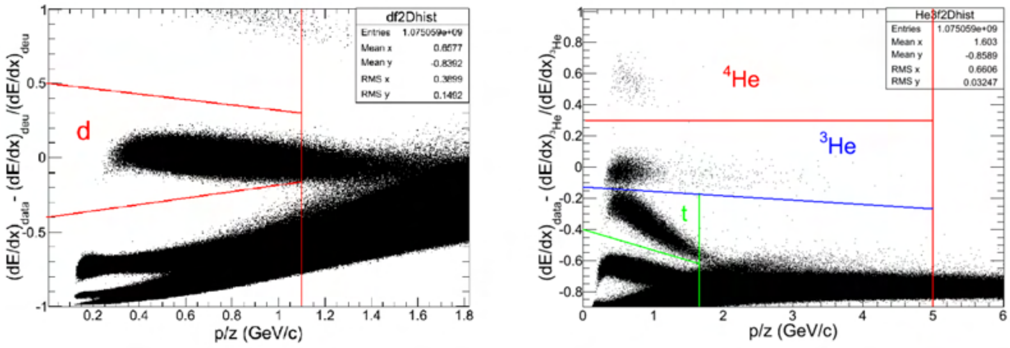

Figure 6.3: The specific energy loss as function of rigidity for deuterons and helium-3.

where β_s is the surface velocity, it is a free parameter of the fit. In many applications, a linear profile is assumed and n is fixed equal to unity. The quality of the fit can be improved if n acts as a further free parameter, whereas the resulting values for the kinetic freeze-out temperature T_{fo} and β_s are only slightly affected [SCH93, SCH12]. The resulting spectral shape is a superposition of the individual thermal sources and is given by

$$\frac{1}{m_t}\frac{\mathrm{d}N}{\mathrm{d}m_t} \propto \int_0^R I_0\left(\frac{p_{\text{t}}\sinh\rho}{T_{\text{fo}}}\right) K_1\left(\frac{p_{\text{t}}\cosh\rho}{T_{\text{fo}}}\right) r\,\mathrm{d}r\,,$$

$I_0(x)$ and $K_1(x)$ are Bessel functions and $\rho = \tanh^{-1}\beta_r$. An example fit is shown in Fig. 6.1 with a common parameter set in the 0-5% centrality class and the resulting fit parameters in all other centrality bins. The excesses at low momenta are due to feed-down from resonance decays, mainly $\rho(770) \rightarrow \pi^+\pi^-$ for the pions and $\phi(1020) \rightarrow K^+K^-$ for the kaons.
The comparison of this fit with the previous results from STAR at RHIC is shown in Fig. 6.2. We observe a 10% higher radial flow at the LHC compared to RHIC.

Blast-wave fits allow a simple phenomenological description of spectra as the model parameters are fit to the data. They can not describe the full collective properties. For this a full hydrodynamic theory is needed. But they offer an easy way to study systematically the evolution of particle spectra with only three parameters.

The previous equation shows the presence of transverse flow effectively leads to a characteristic modification of the spectral shape [HEI04]. The collective flow increases the particle energies proportional to their rest mass m_i. Thus the spectrum at low momenta ($p_{\text{t}} \ll m_i$) can be described with a correspondingly higher effective temperature T_{eff}. One directly obtains the expected scaling $T_{\text{eff}} \approx T_{\text{fo}} + \frac{1}{2}m_i\langle\beta_s\rangle^2$ in the non-relativistic limit [SCH99]. Another advantage of the blast-wave fits is given by the fact that the obtained parameters can also be used to approximate the spectral shape for any particle i with a given mass m_i. This will be used in the upcoming sections.

6.2 Light nuclei (deuterons (d) and helium-3 (^{3}He))

The excellent performance of TPC and TOF allows for the clear identification of all stable particles over a range of 0.15 to 5 GeV/c in rigidity $R = p/z$, where p is the track momentum and z is the charge number. The measurement of light nuclei makes use of this.

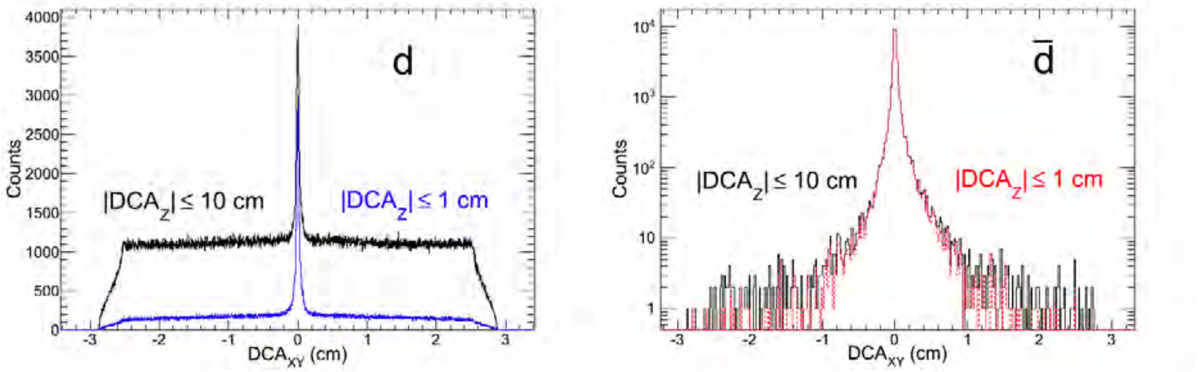

Figure 6.4: DCA$_{\mathrm{XY}}$ for two different DCA$_{\mathrm{Z}}$ cuts for deuterons (left) and anti-deuterons (right).

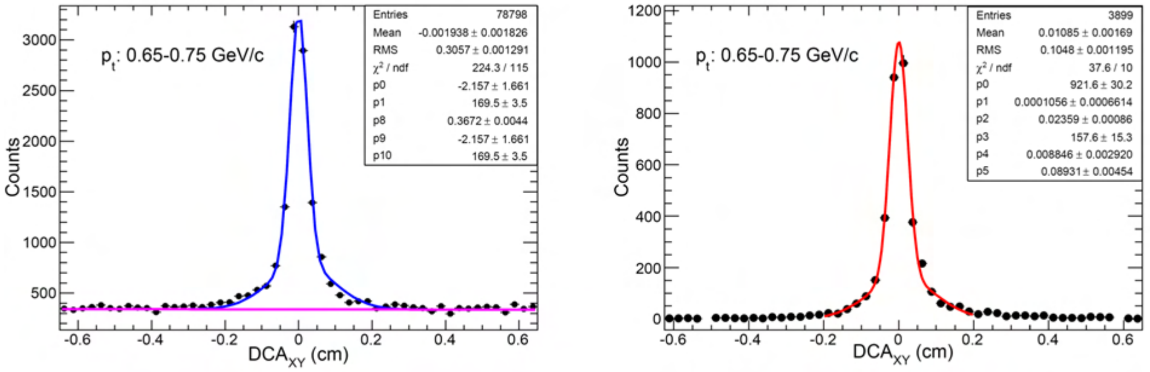

Figure 6.5: DCA$_{\mathrm{XY}}$ distribution of deuterons and anti-deuterons in the transverse momentum region $0.65 \leq p_t \leq 0.75$ GeV/c. Left panel: DCA$_{\mathrm{XY}}$ distribution of deuterons fitted with a function (2 Gauss + 1 linear) as blue line. To calculate yield linear background (pink line) is subtracted. Right panel: DCA$_{\mathrm{XY}}$ distribution of anti-deuterons fitted with a function (2 Gauss) as red line.

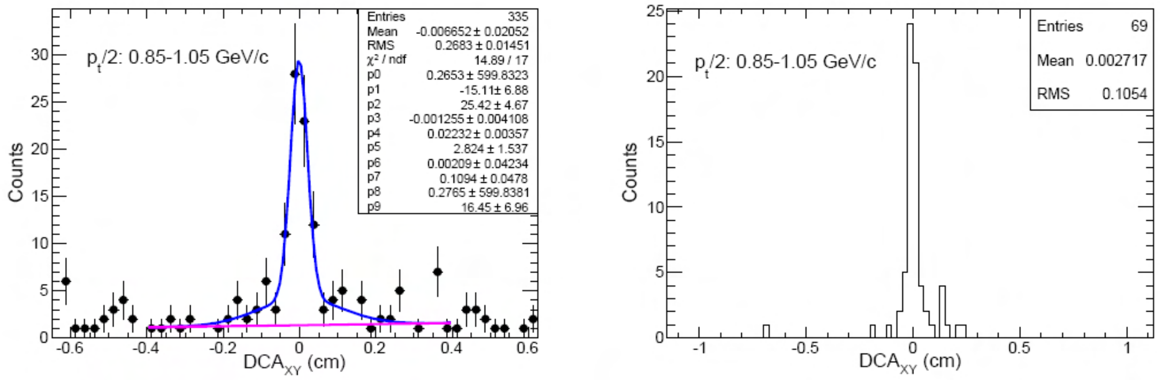

Figure 6.6: DCA$_{\mathrm{XY}}$ distribution of helium-3 and anti-helium-3 in the transverse momentum region $0.85 \leq p_t/2 \leq 1.05$ GeV/c. Left panel: DCA$_{\mathrm{XY}}$ distribution of helium-3 fitted with a function (2 Gauss + 1 linear) as blue line. To calculate yield linear background (pink line) is subtracted. Right panel: DCA$_{\mathrm{XY}}$ distribution of anti-helium-3.

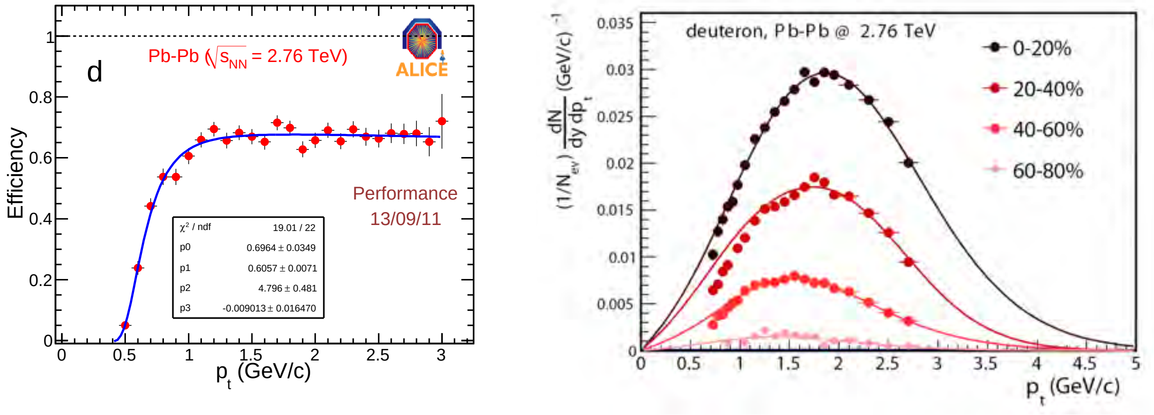

Figure 6.7: Deuteron efficiency in Pb–Pb and corrected spectrum in four centrality classes, fitted with blast-wave functions (right).

We concentrate here on the analysis of deuterons and helium-3 which are needed as limits for the searches. The various connected track selection cuts are shown in table 6.1.
To identify deuterons and ^{3}He we use the measurement of the specific energy loss ($\mathrm{d}E/\mathrm{d}x$) in the TPC between data and the expected theoretical value of the energy loss, using parametrized Bethe-Bloch curves which are plotted as the function of the rigidity, this is shown in Fig. 6.3 for Pb–Pb data. The left part of the figure shows the d identification, the tracks around zero specific energy loss ($\mathrm{d}E/\mathrm{d}x$) difference are identified as deuterons. Like this, one can clearly identify d up to the momentum range of 1.1 GeV/c. To further go up in rigidity and clearly identify the d also TOF is used. This is done by a fit of signal+background to the m^2-distribution of the deuterons. The right part of the figure 6.3 shows ^{3}He and ^{4}He identification for Pb–Pb collisions. Also tritons are visible. ^{3}He and ^{4}He are identified similar to the deuteron by using parametrized Bethe-Bloch curve for ^{3}He. We can clearly identify ^{3}He up to 8 GeV/c rigidity, since the helium is doubly charged and has a mass number of three (or four for the alpha). Therefore helium-3 and helium-4 are nicely separated from the particles with a charge of unity.

Secondary tracks, mainly from knock-out in the material, are rejected using the distance of closest approach (DCA) to the reconstructed vertex information. It can be seen from Fig. 6.4 that the $\mathrm{DCA_Z}$ cut of 1.0 cm removes a large fraction of background for deuterons. Further a $\mathrm{DCA_{XY}}$ cut is used to select primary tracks. In order to select primary d, $\mathrm{DCA_{XY}}$ is plotted for various momentum slices of 0.1 GeV/c, one example is shown in Fig 6.5 for Pb–Pb data. As can be seen from the lower plot of Fig. 6.4 there are less counts for deuterons outside the $|\mathrm{DCA_{XY}}| \leq 1.0\,\mathrm{cm}$. We need to reject the linear background in order to count the primary deuterons. For this, we fit the corresponding anti-deuteron $\mathrm{DCA_{XY}}$ distribution (same p_t range) with two Gaussian functions (red line in Fig. 6.5) and then fit the deuteron $\mathrm{DCA_{XY}}$ distribution with two Gaussian function plus one linear line (blue line in Fig. 6.5). To obtain the primary deuterons we then subtract the linear background (pink line in Fig. 6.5) from the fit function in the $|\mathrm{DCA_{XY}}| \leq 1.0\,\mathrm{cm}$ region. To select primaries the $\mathrm{DCA_{XY}}$ is plotted for various transverse momentum slices of size 0.2 GeV/c, one of the example is shown in Fig. 6.5. For ^{3}He the $\mathrm{DCA_{XY}}$ distribution of variable transverse momentum slices is made because of less statistics, one of the examples is shown in Fig. 6.6. The ^{3}He yield is calculated by integrating counts in $|\mathrm{DCA_{XY}}| \leq 0.5\,\mathrm{cm}$ in their $\mathrm{DCA_{XY}}$ distribution. The same procedure as used for deuterons is used to count ^{3}He in the $|\mathrm{DCA_{XY}}| \leq 0.5\,\mathrm{cm}$ region i.e. by fitting the $\mathrm{DCA_{XY}}$ distribution with a function (2 Gauss + 1 linear) and then subtracting the linear background. The statistical error is calculated as $\sqrt{(\mathrm{Sig}+\mathrm{Bg})+\mathrm{Bg}}$. The raw

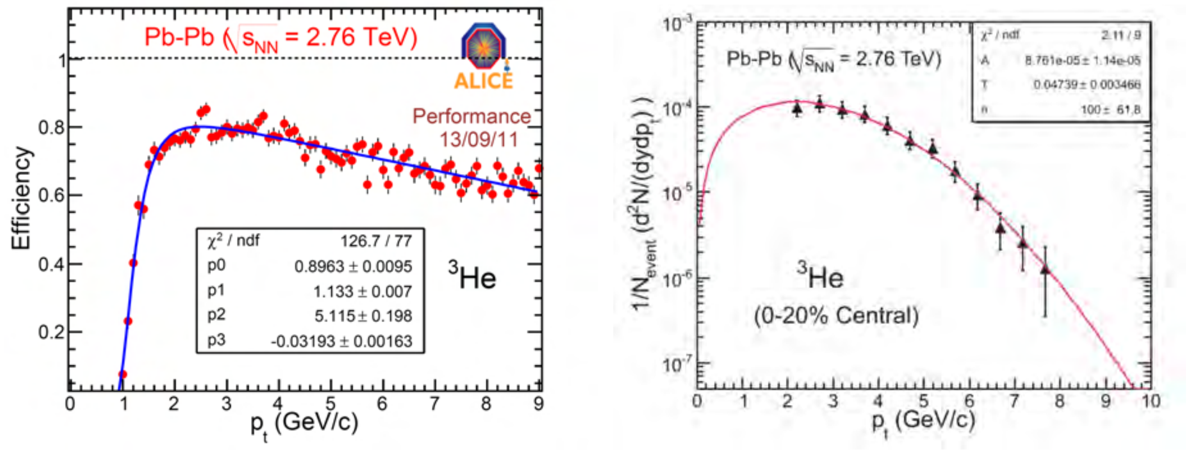

Figure 6.8: ^{3}He efficiency in Pb–Pb (left) and corrected spectrum fitted with a blast-wave distribution (right).

yield of various nuclei is obtained after background rejection.

To get the final yield of nuclei the efficiency correction has to be taken into account. The efficiency correction for nuclei is done using Geant3 [GEANT] in the AliRoot framework [ALIROOT]. The simulation for obtaining the nuclei efficiencies in Pb–Pb collisions is done by including one d, one ^{3}He and one ^{4}He in each parametrised HIJING [HIJING] event. Fig. 6.7 shows the deuteron efficiency as a function of transverse momentum for 0-80% Pb–Pb collisions at 2.76 TeV. A similar efficiency plot is obtained for ^{3}He (see Fig 6.8). The efficiency and acceptance corrected spectra for d (in 4 centrality bins) and ^{3}He (for a centrality of 0-80%) are shown in Fig 6.7, and respectively Fig. 6.8. They are fitted with blast-wave functions.

Combining the specific energy loss (dE/dx) in the TPC and the TOF information as discussed above, we identified 10 anti-alpha nuclei in 23 million Pb–Pb collisions at $\sqrt{s_{\mathrm{NN}}} = 2.76\,\mathrm{TeV}$, recorded in the heavy-ion run of November 2011 where a trigger mix of minimum bias, semi-central and central events was applied. We further apply an offline trigger selecting all $^3\overline{\mathrm{He}}$-nuclei or heavier candidates. Figure 6.9 shows the dE/dx versus rigidity distribution for candidates after the offline selection for negative particles in the region where the bands of $^3\overline{\mathrm{He}}$ and $^4\overline{\mathrm{He}}$ are clearly visible. Below a rigidity of $p/z \approx 2\,\mathrm{GeV}/c$ three candidates are clearly identified based on the dE/dx information only. At higher p/z the energy-loss information of the candidates is combined with mass determination performed with the TOF detector following $m^2/z^2 = R^2/(\gamma^2 - 1)$. The inlet in Fig. 6.9 shows the m^2/z^2 distribution for all tracks within a 2σ-band around the expected dE/dx for $^4\overline{\mathrm{He}}$. The 10 identified anti-alphas are highlighted in both the m^2/z^2 and the dE/dx versus rigidity plot. A similar analysis had been performed for the 2010 data, which led to four anti-alpha candidates [AKA11]. The anti-alpha was observed first by the STAR collaboration in 2011 [AGA11].

6.3 Hypernuclei: hypertriton

The lightest hypernucleus is the hypertriton, consisting of a proton, a neutron and a Λ. It has a mass of $2.991\,\mathrm{GeV}/c^2$ and a lifetime close to the one of the free Λ [MAR11]. The hypertriton and anti-hypertriton are identified via their weak decays ($^3_\Lambda\mathrm{H} \to {}^3\mathrm{He} + \pi^+$ and $^3_{\overline{\Lambda}}\overline{\mathrm{H}} \to {}^3\overline{\mathrm{He}} + \pi^-$), for details of the signal reconstruction see also [LEA12, MAR11]. Using the data of 2011, a signal for hypertriton (anti-hypertriton) with a significance of 4.6 (2.6) has been obtained. The background was evaluated with

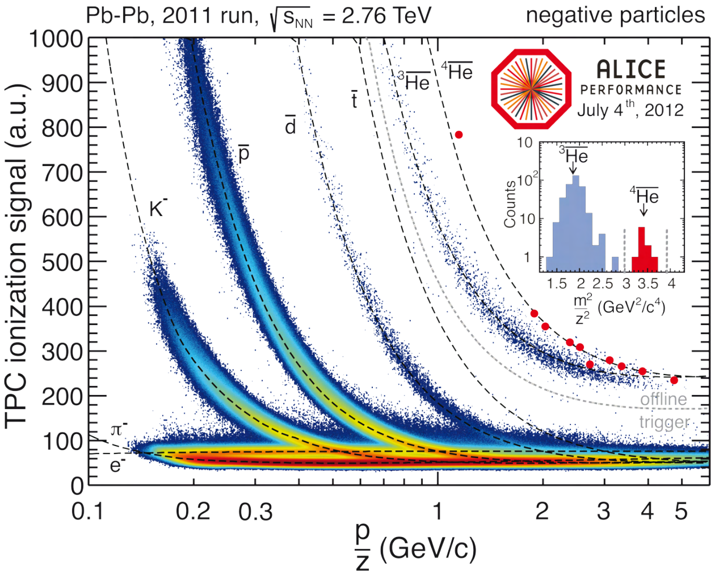

Figure 6.9: TPC dE/dx spectrum for negative particles after a selection of events that contain at least one $^3\overline{\mathrm{He}}$ or $^4\overline{\mathrm{He}}$ candidate. The inlet shows the m^2/z^2 distribution for this pre-selected data. The 10 anti-alphas clearly identified by TPC and TOF are indicated as red dots.

two different methods, i.e. like-sign and a combined fit (Gaussian on top of a third order polynomial, where the Gaussian describes the signal and the polynomial the background shape), shown in Fig. 6.10. Combining the information from the fits, a mean value of $\mu = (2.992 \pm 0.001)\,\mathrm{GeV}/c^2$ (only statistical error) for the mass, which agrees with the world data, and a width of $\approx 3.4 \times 10^{-3}\,\mathrm{GeV}/c^2$, are extracted. The latter reflects the resolution over the covered momentum range. For this analysis, the work on efficiency correction, where the main issue is connected to the poorly known $^3\overline{\mathrm{He}}$ matter interaction, and the connected study of systematics are ongoing. But a clear signal is observed in the data.

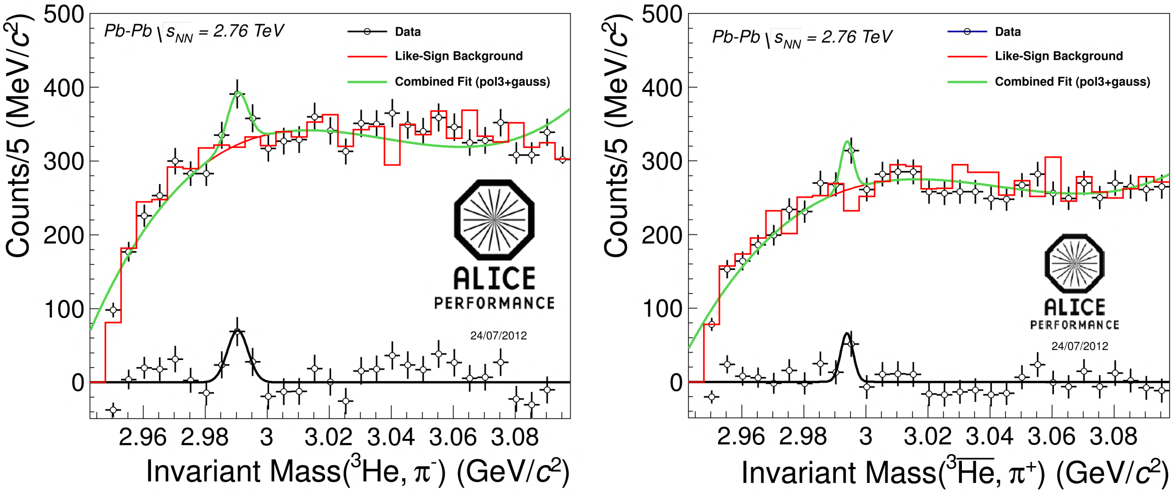

Figure 6.10: Invariant-mass analyses for hypertriton (left) and anti-hypertriton (right). Both figures show data (black), like-sign background (red) and a combined fit of a Gaussian on top of a third order polynomial (green).

6.4 H-Dibaryon

6.4.1 Analysis strategy

The analysis strategy for the H-Dibaryon is based on the search of one V0 candidate identified as a Λ going into p and π^- and another V0 kind decay pattern at the decay vertex of the H-Dibaryon, see figure 6.11. First the invariant mass of the Λ is reconstructed (shown in Fig. 6.12) and then the candidates in the invariant mass window of $1.1113\ \mathrm{GeV}/c^2 < m_\Lambda < 1.1202\,\mathrm{GeV}/c^2$ are combined with the Four-Vectors of the p and π at the decay vertex. The decay vertex is constructed via the two opposite signed tracks. To identify the protons and the pions for both the true Λ and the V0 kind topology at the H^0 decay vertex a 3σ $\mathrm{d}E/\mathrm{d}x$ cut in the TPC is used.
The cuts which are used are grouped together in table 6.2.

6.4.2 Efficiency and acceptance

To estimate the efficiency × acceptance we generated a Monte Carlo sample of Hijing events enhanced with Λn and H-Dibaryon, anchored to the corresponding runs of real data. This means that the main distributions like vertex distribution and multiplicity are forced in the generation process to be close to the ones of the data.
For the production of the hypermatter enhanced sample the new particles H-Dibaryon and Λn bound state (plus the Hypertriton in its two and three body decay) first had to be added to AliRoot via Virtual Monte Carlo. In the sample they are then added on top of a minimum bias MC event. This is done flat in p_t from 0 to 10 GeV/c and flat in rapidity from -1 to 1.

The efficiency is then estimated using the described Monte Carlo production. In Fig. 6.13 the generated H-Dibaryons are shown on the left side and the corresponding reconstructed associates are shown on the right side. The result of the division of the two, towards the p_t axis projected, histograms is shown in Fig. 6.14. The estimated efficiency is of the order of 0.04.
Since the efficiency is p_t dependent it has to be weighted with the shape of the p_t spectrum, for this we use a blast-wave calculation (see Fig. 6.15) which uses the blast wave fits of p, K, π measured with ALICE as an input.
From the convolution of the efficiency with the blast-wave calculation one gets the true efficiency as the integral of the convoluted function (see Figure 6.16), this leads to an overall p_t weighted efficiency of 0.0385.

The gathered statistics are 13.8 million events after physics selection and in centrality from 0-80 %. For the dedicated MC production of the Λn bound state and the H-Dibaryon 42128 events have been produced locally.

6.4.3 Estimation of expected yields

From the statistical hadronization model one gets a value for the possible yield per rapidity unit in central collisions (Fig. 2.5) which is for the H-Dibaryon $\mathrm{d}N/\mathrm{d}y|_{0-80\%} = 3.1 \times 10^{-3}$ in the 0-80 % centrality class which is analysed here.

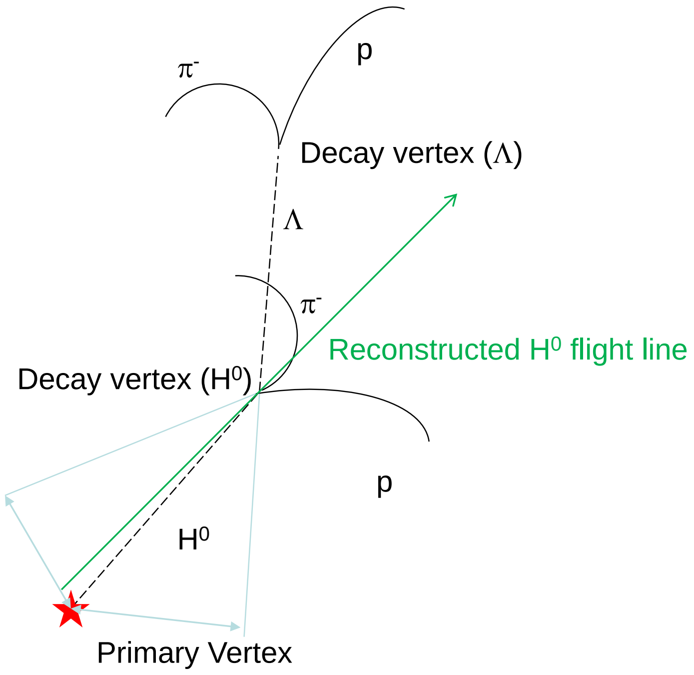

Figure 6.11: Decay topology of the H-Dibaryon.

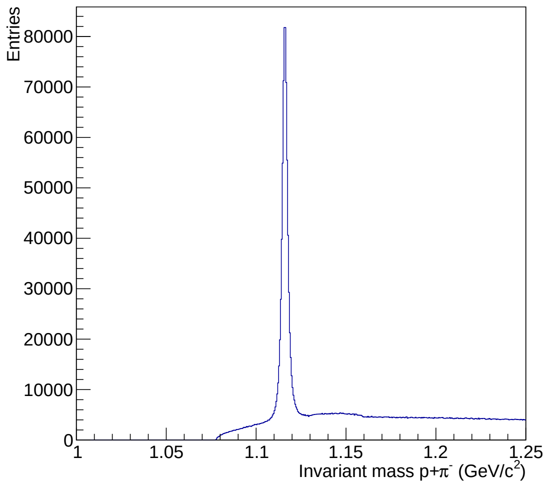

Figure 6.12: Reconstructed invariant mass for Λs used for the further analysis.

One can calculate the number of expected H-Dibaryons as the product of number of events, efficiency, branching ratio of the Λ, dN/dy and the accessible rapidity window:

$$N_{\mathrm{H}^0,\,exp.\ w/o\ \mathrm{H}^0\ BR} = \underbrace{1.38\cdot 10^7}_{events}\cdot\underbrace{0.0385}_{eff.}\cdot\underbrace{0.64}_{BR(\Lambda)}\cdot\underbrace{3.1\times 10^{-3}}_{\frac{dN}{dy}}\cdot\underbrace{2}_{dy} = 2108.2\,. \tag{6.1}$$

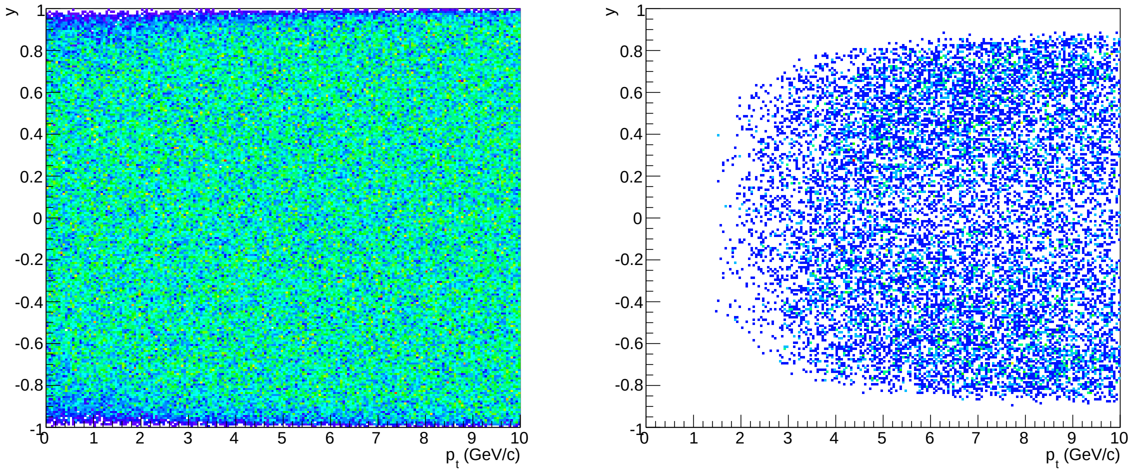

Figure 6.13: y vs. p_t from generated (left) and reconstructed (right) H-Dibaryon.

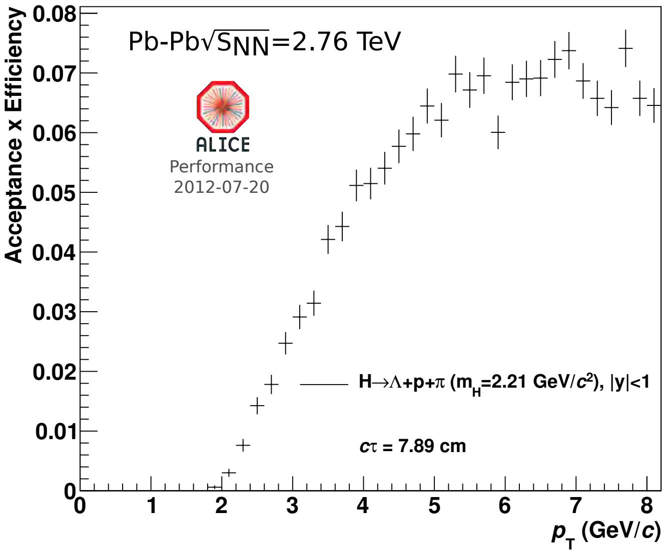

Figure 6.14: Acceptance x Efficiency for the H-Dibaryon.

To get an estimate for the expected yield at a given mass this has now to be multiplied with the expected branching ratio of the H-Dibaryon. From the calculation of J. Schaffner-Bielich and colleagues (see Figure 2.4) it ranges from 0.1 for a deeply bound H to 0.64 at the $\Lambda\Lambda$ threshold. So we would expect $2108.2 \times 0.1 = 211$ H candidates for a deeply bound state and $2108.2 \times 0.64 = 1349.2$ for weakly bound H close to the $\Lambda\Lambda$ threshold.

Figure 6.17 shows the invariant mass reconstructed from real data and on top the two possible observations for a deeply bound H-Dibaryon (in blue) and one close to the $\Lambda\Lambda$ threshold (in red).

The latest theoretical discussion concludes (see [SHA11, HAI11] and references therein) that the H is either a sligthly bound state or an unbound resonance between $\Lambda\Lambda$ threshold and the Ξp threshold which

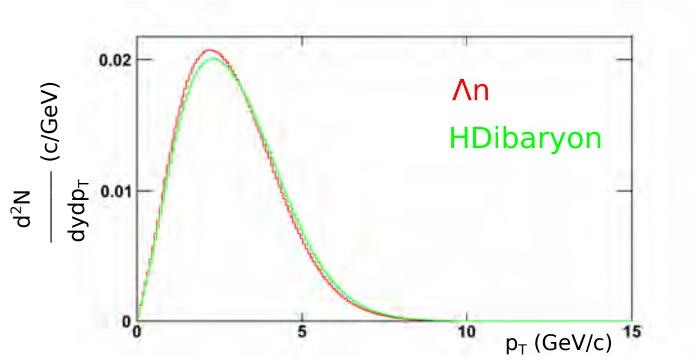

Figure 6.15: Blast wave calculation for Λn bound state (red) and H-Dibaryon (green), which is based on the p,K,π spectra. The integral is normalised to one.

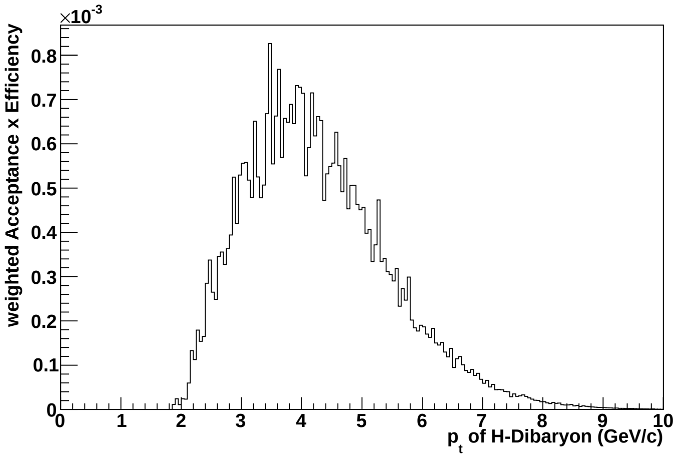

Figure 6.16: Convolution of the blast-wave calculation (Figure 6.15) for the H-Dibaryon with the acceptance × efficiency extracted from MC (Figure 6.14).

are indicated in Figure 6.17 as arrows.

6.4.4 Error estimation

To estimate the error of the expected yield one should take into account the error of the output of the statistical hadronization model and the uncertainty of the weighted efficiency. Since the influence of the p_t spectrum is the major source of uncertainty, we investigate different mathematical functions to describe the p_t shape. For this we use Levy-Tsallis, Fermi-Dirac, Bose-Einstein and Boltzmann. The mean p_t for the H has to be between the mean p_t of the deuteron (m_d) and that of the ^{3}He ($m_{^3\mathrm{He}}$) since its mass lies between them for the discussed cases.
The mean p_t of π, K, p, deuteron and ^{3}He is shown in Fig. 6.19. The Evaluation of the weighted mean for the different functions leads to a minimum efficiency of 0.0288 and a maximum efficiency of 0.0493.

Thus we assign an absolute error of the efficiency of (0.0493-0.0288)/2 = 1.025×10^{-2}.
Taking this into account one gets as expected numbers for the deeply bound H: 211±56 and for the

slightly bound H: 1349±359.

To further estimate the error of the measured invariant mass we changed the topological cuts which are shown in table 6.2 for data and Monte Carlo systematically. By this we can see that the efficiency is changing up to 20%. The invariant mass is behaving non-linear as visible in fig. 6.17.

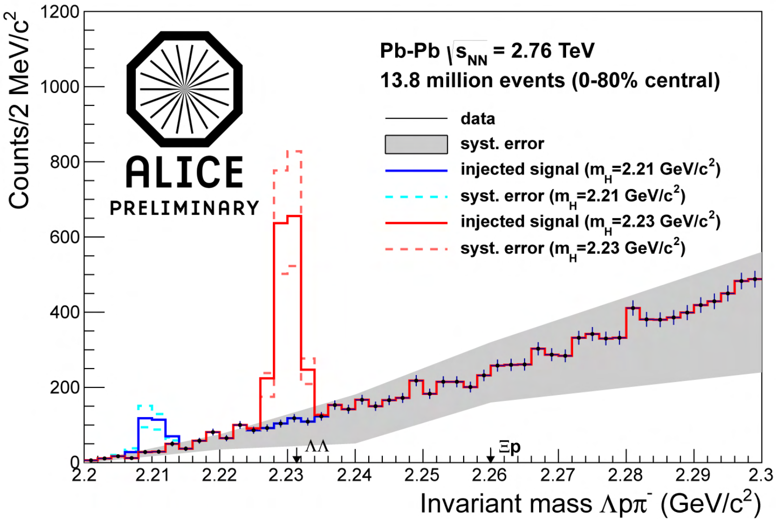

Figure 6.17: Final invariant mass of H-Dibaryon→ $\Lambda p \pi^-$ with injected signal for a weakly bound H in red ($m_H = 2.23\,\mathrm{GeV}/c^2$) and a stronger bound H in blue ($m_H = 2.21\,\mathrm{GeV}/c^2$). The arrow at 2.231 GeV/c^2 indicates the ΛΛ threshold and the arrow at 2.260 GeV/c^2 the Ξp threshold. The systematic errors are shown for data in grey and for the injected signals as dashed lines.

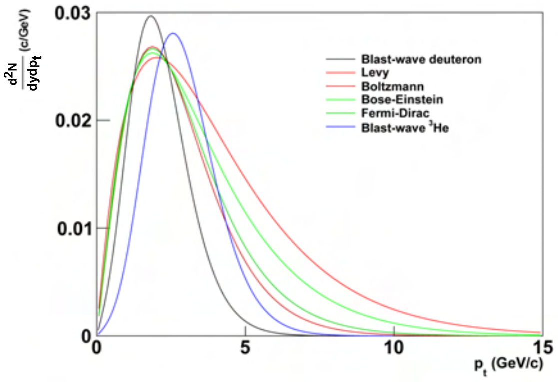

Figure 6.18: Different mathematical functions used for the evaluation of the systematic errors of the weighted efficiency. The two extreme cases are in black the blast-wave fit of the deuteron and in blue the blast-wave fit of the ^{3}He. The other functions are Levy-Tsallis, Fermi-Dirac, Bose-Einstein and Boltzmann as described in the text.

6.4.5 Upper Limit

In a first conclusion one can say that the expected yield is not observed and an upper limit of the production yield can be set. The simplest possibility to get a rough estimate of the maximum signal included in

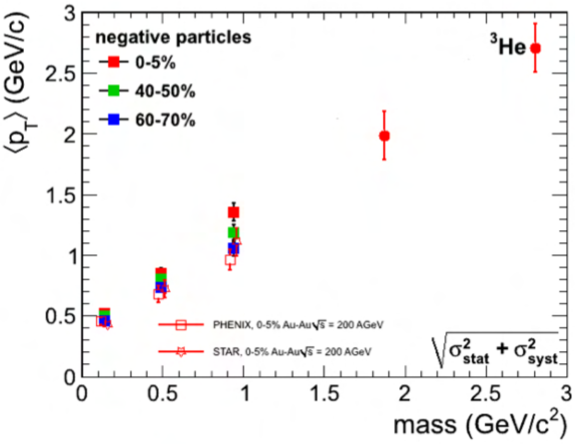

Figure 6.19: Mean p_t vs. mass for different particles (π, K, p, d and ^{3}He). The full markers correspond to ALICE points, the open points to RHIC measurements.

the measured invariant mass distribution we use the signal significance as a measure. The signal significance (ς) of a signal S is defined as $\varsigma = \frac{S}{\sqrt{S+B}}$, whereas B denotes the background in the signal region. One can now resolve this equation for the signal S which is unknown a priori. This leads to

$$S^2 - \varsigma^2 S - \varsigma^2 B = 0\,, \text{so one gets } S \text{ as} : S_{1,2} = \frac{\varsigma}{2} \pm \sqrt{\frac{\varsigma^2}{4} + \varsigma^2 B}\,. \tag{6.2}$$

We calculate the necessary signal for a significance of 5, which is typically the value needed to claim an observation. From the data we get in a 3σ region around the signal a background of 423±21 counts (for the slightly bound H), respectively 153±12 counts for the stronger bound H. Using this as an input one can calculate the necessary signal for a significance of 5 by:

$$S_{1,2} = \frac{5}{2} \pm \sqrt{\frac{5^2}{4} + 5^2 B}\,. \tag{6.3}$$

From this we get a necessary signal S of 116 counts for the weakly bound H and 76 counts for the stronger bound H. But the expected signal predicted by the thermal model is 1349±359, respectively 211±56.

This can be also translated into an upper limit for a given confidence level using a more sophisticated method. This is done using a frequentist approach which assumes Poissonian likelihood distributions for background and signal. The method we use here to determine the upper limit was introduced in [ROL01] and further extended in [ROL05].

The usual Neyman construction [NEY37] used by frequentists for the confidence belt is in this method replaced by the usage of -2 log distribution of a likelihood profile.

From the likelihood, which is treated as fully Poissonian in our case, a likelihood ratio $\Lambda(\mu;x,y)$ is constructed. μ is the expected signal, x are the events in the signal region and y the events in the background region. $\Lambda(\mu;x,y)$ is the ratio of the null hypothesis and the description of the data if no assumption is made for μ. This is then used as likelihood profile and since the $-2\log\Lambda(\mu;x,y) \sim \chi^2(d)$ the profile can be treated as a χ^2 distribution. This allows the determination of the upper limits from the treatment of the profile in a numerical minimisation process similar to MINUIT [JAM75, JAM80], which is widely used as the optimisation algorithm for fitting in high-energy physics. This allows the estimation of the upper limit, for this we used the ROOT package TRolke, which also takes into account the uncertainty on the efficiency. For the observed background of the stronger bound H we observe an upper limit of 31.4 (57.4) at 95% (99%) confidence level for a signal. For the slightly bound H we observe 54.5 (85.8) at 95% (99%) confidence level. This leads to dN/dy of 4.6×10^{-4} (8.4×10^{-4}) for the deeply bound H and 1.25×10^{-4} (2×10^{-4}) for the slightly bound one as upper limits.

6.4.6 Lifetime dependence

The influence of the lifetime on the efficiency was studied by three small Monte Carlo productions which were done at the GSI computing facility. We set the lifetime of the H-Dibaryon from 2.63×10^{-10} s, to 1.3×10^{-10} s, to 5.2×10^{-10} s and 1.4×10^{-9} s. This corresponds to $0.5\times\Lambda$-lifetime, $2\times\Lambda$-lifetime and $5.3\times\Lambda$-lifetime. The influence of the lifetime on the efficiency is shown in Fig. 6.20. The result for the upper limit is shown in table 6.3.

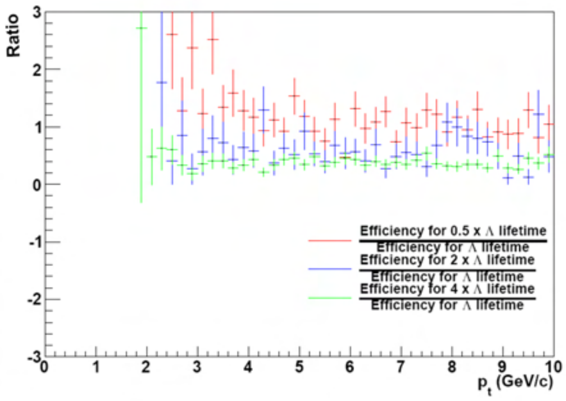

Figure 6.20: Efficiency dependence on the lifetime of the H-Dibaryon.

6.5 Λn bound state

6.5.1 Analysis strategy

The analysis strategy for the $\overline{\Lambda \text{n}}$ bound state is assuming a V0 decay topology for this state. Therefore the V0 online finder is used to detect it. We focus here on the $\overline{\Lambda \text{n}}$, since the background is much lower compared to Λn because of knocked-out deuterons on the matter side. As sketched in the schematic picture of the decay in figure 6.21, the $\overline{\Lambda \text{n}}$ bound state decays into a $\overline{\text{d}}$ and a π^+. The deuterons and pions are selected with their specific energy loss dE/dx in the TPC and the invariant mass of these two daughters is calculated.
The track cuts, as well as the V0 and kinematical cuts, which where used in the analysis are summarised in table 6.4.

6.5.2 Efficiency estimation and expected signal

The efficiency was determined by using the above indicated Monte Carlo production, and is shown in figure 6.24. It is analysed in the same way as the H-Dibaryon.

As for the H-Dibaryon one gets a value for the possible yield per rapidity unit in central collisions from the statistical hadronization model, see figure 2.5. This is for the $\overline{\Lambda\mathrm{n}}$ bound state of the order of $\mathrm{d}N/\mathrm{d}y = 6.5 \times 10^{-2}$. This has to be adjusted to the 0-80 % centrality which is analysed here, which leads to $\mathrm{d}N/\mathrm{d}y|_{0-80\%} = 1.625 \times 10^{-2}$.
The branching ratio is taken from Fig. 6.25 to be 0.35, since it depends on the binding energy of the Λn bound state which is around 1.3 MeV according to the HypHI experiment which claims its observation (shown at conferences but not published so far, see for instance [HYP11, HYP12]). Using this all as an input one gets:

$$N_{\overline{\Lambda\mathrm{n}},\, rec} = \underbrace{1.38 \cdot 10^7}_{events} \cdot \underbrace{0.0255}_{eff.} \cdot \underbrace{0.35}_{BR} \cdot \underbrace{0.01625}_{\frac{dN}{dy}} \cdot \underbrace{\ 2\ }_{dy} = 4002.9\ . \tag{6.4}$$

Figure 6.26 shows the invariant mass reconstructed from real data and on top the possible observations for a $\overline{\Lambda\mathrm{n}}$ bound state.

6.5.3 Error estimation

Errors can be evaluated like for the H-Dibaryon. The error for the efficiency is 0.014.
This leads to a value of the expected $\overline{\Lambda\mathrm{n}}$ yield of 4003±2198.

As for the H-Dibaryon the signal is clearly not observed and an upper limit and the confidence level of the exclusion has to be determined.
We use the same strategy as for the H and calculate the necessary signal for a significance of 5. The background in the 3σ region around the peak is 9868.
From this we get a required signal of 366. So the statistical hadronisation model would need to be wrong by a factor of 11.
Using the above discussed statistical evaluation one gets an upper limit of 258.1 (405.4) at 95% (99%) confidence level. From this one can estimate the corresponding $\mathrm{d}N/\mathrm{d}y$ to 1×10^{-3} (1.6×10^{-3}).

We also studied the influence of the lifetime on the efficiency using the same three small Monte Carlo productions which were done locally. We set the lifetime of the Λn bound state from 2.63×10^{-10} s, to 1.3×10^{-10} s, to 5.2×10^{-10} s and 1.4×10^{-9} s. This corresponds to 0.5×Λ-lifetime, 2×Λ-lifetime and 5.3×Λ-lifetime. The behaviour of the efficiency is shown in Fig. 6.27. The result for the upper limit is shown in table 6.5.

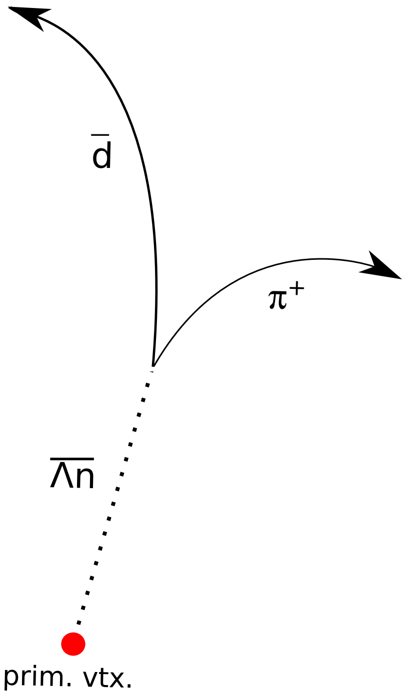

Figure 6.21: Decay topology of the $\overline{\Lambda n}$ bound state.

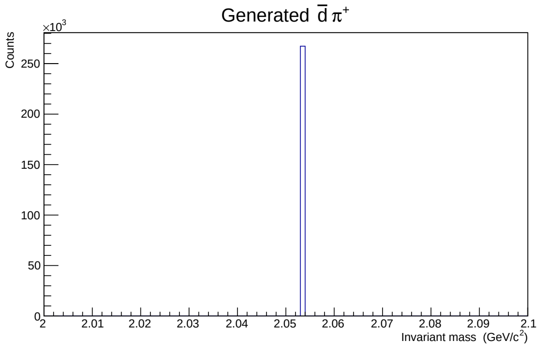

Figure 6.22: Invariant mass of $\bar{d}$ and π^+ originating from the generated $\overline{\Lambda n}$ bound states.

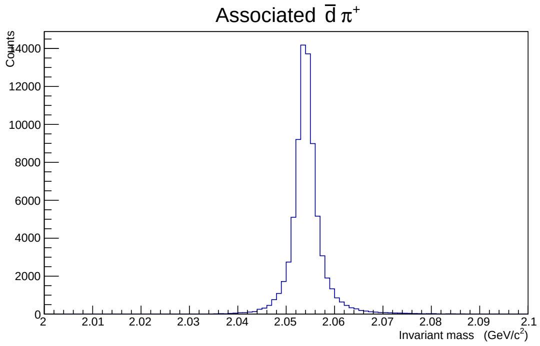

Figure 6.23: Invariant mass of $\bar{d}$ and π^+ associated to the generated $\overline{\Lambda n}$ bound states.

$\lvert V_Z \rvert$	$\leq$ 10cm
No.of TPC Clusters	$\geq$ 80
χ^2 per TPC Clusters	$\leq$ 4
$\lvert \eta \rvert$	$<$ 1.5
$\lvert$DCA$_Z$	$\leq$ 10 cm
Kink daughters	rejected
min number of ITS Clusters	1

Table 6.1: Track selection cuts for the nuclei analysis

cut	**value**
Track cuts	
Kink daughters	rejected
TPC	refit
$\mathrm{n}_{\mathrm{clusters}}$(TPC)	> 80
χ^2/cluster	< 5
$\lvert\eta\rvert$	≤ 0.9
V0 cuts	
dca V0 daughters	< 1 cm
dca positive V0 daughter - Vertex	< 1 cm
dca negative V0 daughter - Vertex	< 1 cm
Kinematical cuts	
dca positive H^0 daughter - Vertex	> 1 cm
dca negative H^0 daughter - Vertex	> 1 cm
dca H^0 daughters	< 1 cm
Pointing angle of H^0	< 0.1 rad

Table 6.2: Cuts used for the H-Dibaryon analysis

lifetime (10^{-10} s)	**decay length (cm)**	**efficiency**	**upper limit**
1.3	3.95	0.0531	0.00061
2.63	7.89	0.0385	0.00084
5.2	15.8	0.0308	0.0011
14	42	0.0154	0.0017

Table 6.3: Efficiency and upper limit in dependence of the lifetime of the H-Dibaryon

cut	**value**
Track cuts	
Kink daughters	rejected
TPC	refit
$\mathrm{n}_{\mathrm{clusters}}$(TPC)	> 60
χ^2/cluster	< 5
pseudo-rapidity $\lvert\eta\rvert$	$\lvert\eta\rvert < 0.9$
rapidity y	$\lvert y\rvert < 1$
V0 and kinematical cuts	
VO finder	online
Cosine of pointing angle	$\cos(\Theta) > 0.99$
DCA V0 daughters	$dca < 1$ cm
Momentum p_{tot} of the anti-deuteron	$p_{tot} > 0.2$ GeV/c
Energy loss dE/dx anti-deuteron	$dE/dx > 110$

Table 6.4: Cuts for $\overline{\Lambda\mathrm{n}}$ bound state analysis

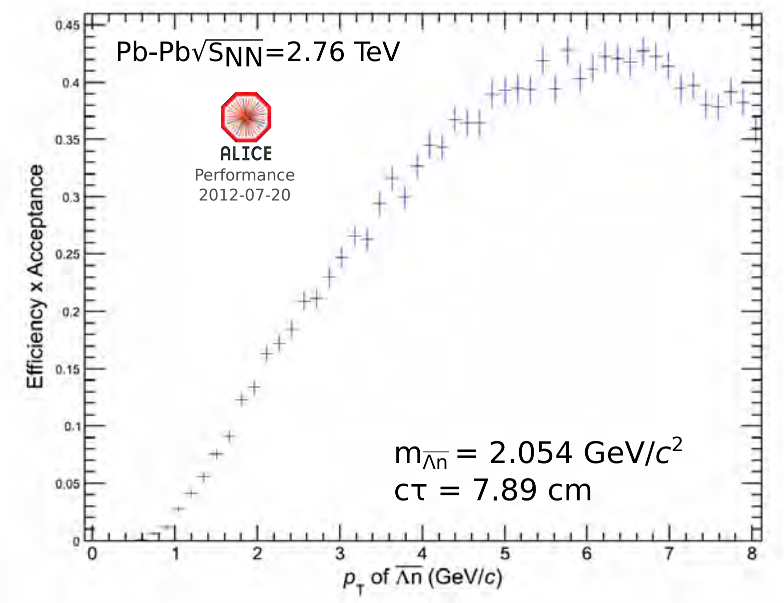

Figure 6.24: Acceptance × Efficiency for the $\overline{\Lambda n}$ bound state.

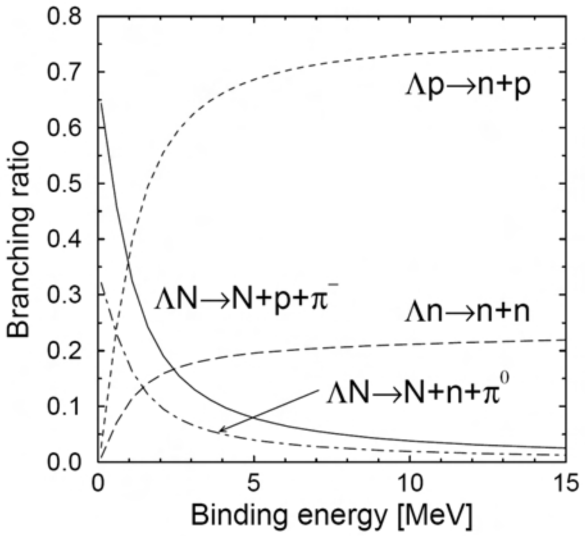

Figure 6.25: Theoretical calculation of the branching ratios of possible Λ-nucleon bound state decay channels [JSB12].

lifetime (10^{-10} s)	**decay length (cm)**	**efficiency**	**upper limit**
1.3	3.95	0.022	0.001708
2.63	7.89	0.0255	0.001474
5.2	15.8	0.032	0.001174
14	42	0.044	0.000854

Table 6.5: Efficiency and upper limit in dependence of the lifetime of the $\overline{\Lambda n}$ bound state

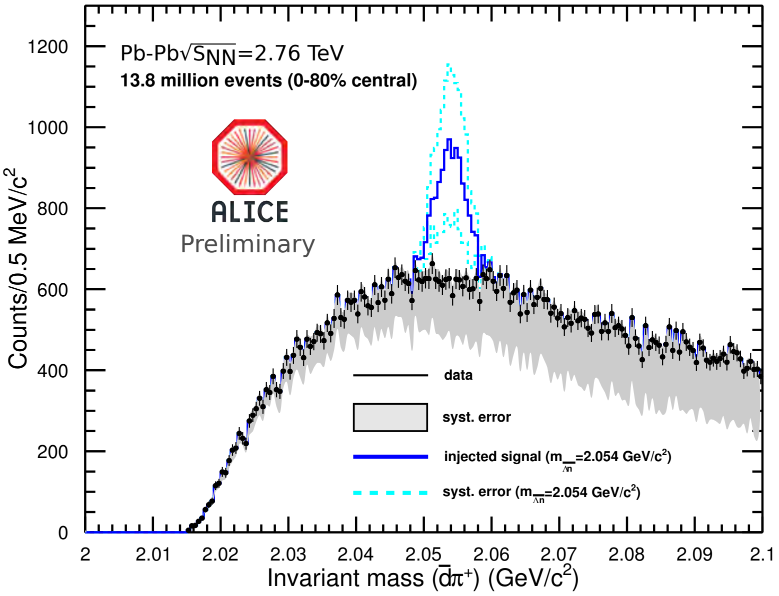

Figure 6.26: Invariant mass of the $\bar{\mathrm{d}}$ and π^+ with injected signal in blue.

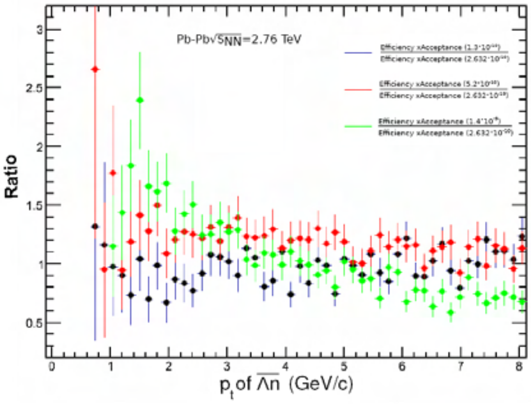

Figure 6.27: Efficiency dependence on the lifetime of the $\overline{\Lambda\mathrm{n}}$ bound state.

Chapter 7

Discussion

The upper limits obtained in the previous chapter are compared with the predictions from the production models introduced in chapter 2. The two models discussed here are the statistical or thermal model and the coalescence model. Both give predictions for the H-Dibaryon production yields, while we only have predictions from the thermal model for the Λn bound state.

The prediction from the thermal model [AND12a] gives values for dN/dy of 3.1×10^{-3} for the H-Dibaryon and 1.625×10^{-2} for the Λn bound state.
While the coalescence gives a value of $\mathrm{d}N/\mathrm{d}y = 9.5 \times 10^{-3}$ for the hadron coalescence and 2.05×10^{-3} for the quark coalescence model for the H-Dibaryon at top LHC energies.

The determined upper limit for the H-Dibaryon (assuming a lifetime of that of a free Λ) is 8.4×10^{-4} for the stronger bound one and 2×10^{-4} for the weakly bound one. This leads to a disagreement of factors of 3.7 for the stronger bound H-Dibaryon and 15.5 for the slightly bound one. The disagreement with the coalescence models are also of the order of 10. This leads to the conclusion that either the model predictions are wrong or this particle simply does not exist.

However, the thermal model is describing the yields of all known particles quite reasonable. The exception are only the protons measured at the LHC (see chapter 1.2). The predictions shown in Fig. 2.5 reach over 8 decades, where the H-Dibaryon and the Λn bound state lie in the upper half of the predictions. On the other hand, the hypertriton $^{3}_{\Lambda}\mathrm{H}$ is measured and a signal of significance of 3 can be established in the ALICE data (discussed in 6.3). Its production probability is a factor of hundred lower than the predicted H-Dibaryon rate. Even particles like the anti-alpha, predicted to have one of the lowest production yield per rapidity unit in Fig. 2.5 are detected as shown in Fig. 6.9 which should be produced by a factor of 10^4 less than the H-Dibaryon.

The thermal model predictions have been calculated for a temperature of 164 MeV this gives a reasonable fit to all up to now measured particles when the protons are left out. The best fit including the protons brings the temperature down to 152 MeV, but gives some tension towards the preliminary measured yields of the multi-strange baryons Ω^- and Ξ^-. One can get an estimate for the temperature needed to explain the factor of 10 difference between upper limit and prediction by assuming a simple exponential behaviour of the thermal production:

$$\frac{Yield_{predicted}}{Yield_{observed}} = \frac{\exp(-m/T_1)}{\exp(-m/T_2)} = C \Rightarrow T_2 = \frac{T_1 \cdot m}{T_1 \ln(C) + m}.$$

Here, m denotes the particle mass, C is the factor between the predicted yield and the observed upper limit, T_1 is the temperature of the prediction and T_2 the temperature at the upper limit. Setting C to 10 and T_1 to 164 MeV, leads to necessary temperatures of 138.6 MeV for the Λn bound state and to 140 MeV for the H-Dibaryon.

If one assumes the thermal model prediction is correct, and the particle exists, then only two possibilities can explain the non-observation of the H-Dibaryon. Either the branching ratios are off by a factor of 10 or the lifetime of the H-Dibaryon of such hight, that it is not decaying in the detector acceptance.

The latter was investigated by estimating the efficiency for different lifetimes and show that at 5 times the lifetime of the free Λ the upper limit will go down by roughly 50% for the H-Dibaryon. Whereas the upper limit for a longer living Λn bound state would go up by more than 50%. This is due to the enlarged fiducial volume for the V0 kind decay of the Λn bound state. However, the H-Dibaryon is harder to detect since the two decay vertices have to be clearly identified. This is only possible if all of the four final decay products (two protons and two pions) are in the acceptance, since the whole H-Dibaryon identification does not work without all four final decay products.

The branching ratios for the H-Dibaryon have been calculated by two different groups (J. Schaffner-Bielich et al. [JSB00] and E. Golowich and colleagues [GOL86, DON86]) and they both agree in the order ($\approx$ 10%) of the decay channel which we analysed. For the $\overline{\Lambda\mathrm{n}}$ bound state we used a calculation of J. Schaffner-Bielich [JSB12] which led us to the 35% for the decay channel and the binding energy observed by the HypHI collaboration [HYP11, HYP12]. From a simple perspective this is even underestimated since the free Λ has a branching ratio of 63.9% [PDG12] and the deuteron + pion decay should be equivalent to this Λ decay. The only other possibility, if charged particles are involved, would be proton + neutron + pion, but the hypertriton [MAR11] decays preferably in deuteron + proton + pion, followed by ^{3}He + pion, but not into 2 protons + neutron + pion. In conclusion, it is unlikely that the branching ratios are off by a factor of 10 or more.
The only reasonable conclusion here is that the the Λn bound state does not exist either.

Chapter 8

Conclusion and Outlook

Within this thesis, we presented results on two different kinds of analyses. A study of the $\Lambda(1520)$ resonance in pp collisions at $\sqrt{s} = 7$ TeV and two searches (H-Dibaryon and $\overline{\Lambda \mathrm{n}}$ bound state) in Pb–Pb collisions at $\sqrt{s_{\mathrm{NN}}} = 2.76$ TeV.

For the $\Lambda(1520)$ we presented a first estimate of the dN/dy of $\frac{\mathrm{dN}}{\mathrm{dy}} = 0.0089 \pm 0.0015\,(\mathrm{stat.})$ and the mean p_{t} of $\langle p_{\mathrm{t}} \rangle = (1.07 \pm 0.11)\,\mathrm{GeV}/c$. The corresponding ratio of the yield of the $\Lambda(1520)$ to the yield of the Λ is in agreement with the values measured by previous experiments at lower energies. The measured mass and width are in agreement with the PDG values. In the scope of this thesis not all errors were estimated completely. For the publication, further checks and a full estimation of all systematics are needed and foreseen.

For the searches for the H-Dibaryon and the $\overline{\Lambda \mathrm{n}}$ bound state we set upper limits since no signal was observed. These limits are for both particles below the thermal and coalescence predictions. The factor 10 difference between upper limit and predictions which we observe, implies temperatures of around 140 MeV instead of the 164 MeV for the thermal model prediction. Further statistics is needed to bring the upper limit further down. The whole data set of 2011 was not touched for these analyses. A rough estimate what could be gained from the usage of the 2011 data can be seen from the analysis of the anti-alpha (shortly discussed in 6.2), where the whole 2011 statistics was scanned and 11 anti-alphas were observed, whereas the data of 2010 allowed the identification of 4. From this we can say that roughly a factor of 3 should be expected utilising the 2011 data.

To get a more precise knowledge about the usage of the 2011 data we make use of the numbers of the J/ψ analysis, they analysed 18×10^6 events in the centrality bin of 0-10% and 13×10^6 events in the centrality of 10-40% [ARS13] for these numbers we can make the same calculation of expected signal as done before in 6.4.3. But we have to take into account the lower efficiency because of several not working chambers and reduced voltage in the TPC and an increase in the number of dead channels in the silicon pixel detector, for this we take only 70% of the efficiency extracted from the simulations done for the 2010 data. We further have to take into account the different centrality class involved in the 2011 data, therefore we use the numbers measured from [AAM11a] and get scaling factors of 0.9 for the 0-10% compared to 0-5% used for the prediction and 0.52 as scaling factor for the 10-40% compared to the 0-5%. So we can make the following calculation:

$$N_{\mathrm{H}^0,\, exp.\ w/o\ \mathrm{H}^0\ BR} = \underbrace{1.8 \cdot 10^7}_{events} \cdot \underbrace{0.0385}_{eff.} \cdot \underbrace{0.7}_{red.eff.} \cdot \underbrace{0.64}_{BR(\Lambda)} \cdot \underbrace{1.05x\,10^{-2}}_{\frac{dN}{dy}} \cdot \underbrace{0.9}_{centr.scal.} \cdot \underbrace{2}_{dy} = 5588.4\,. \qquad (8.1)$$

$$N_{\mathrm{H}^0,\,exp.\ w/o\ \mathrm{H}^0\ BR} = \underbrace{1.3\cdot 10^7}_{events}\cdot\underbrace{0.0385}_{eff.}\cdot\underbrace{0.7}_{red.eff.}\cdot\underbrace{0.64}_{BR(\Lambda)}\cdot\underbrace{1.05x\,10^{-2}}_{\frac{dN}{dy}}\cdot\underbrace{0.52}_{centr.scal.}\cdot\underbrace{2}_{dy} = 2331.9 \qquad (8.2)$$

These numbers have to be multiplied with the possible branching ratios for the H-Dibaryon (0.1 for the stronger bound H-Dibaryon and 0.64 for the lightly bound one) and we get for the stronger bound one 558.8 (0-10%) plus 233.2 (10-40%) which adds up to 792 expected stronger bound H-Dibaryons. For the lightly bound H-Dibaryon we get 3576.5 (0-10%) plus 1492.4 (10-40%) which lead to 5069 expected H-Dibaryons in the 2011 data.
If we now compare this with the expected signal calculated in section 6.4.3 we see that we would gain a factor of 3.75 of signal compared to the 2010 data utilised in the discussed analysis. The calculation for the Λn bound state leads to the same result.
The factor of 3.75 would lead to a drop of the upper limit we have set by an amount of $\sqrt{3.75} = 1.9$. Unfortunately, the events of 2011 are more central, this also leads to an increase of the background which is not easy to approximate. Thus, we assume that the upper limit would drop by an even lower number which is challenging to estimate.
The data of 2011 might help to make a stronger statement if these particles exist. But the current data implies that the H-Dibaryon and the Λn bound state do not exist.

Even if the H-Dibaryon or the ΛΛ bound state do not exist, the ΛΛ interaction is of certain interest also in the connection to the ΛΛ hypernuclei discussed in 2.1. A direct measurement is done through the ΛΛ correlation measurement.
Further bound states (dibaryons and anti-dibaryons with strangeness) are predicted [JSB00, HAI12] and searches for those are possible with the ALICE apparatus.
Furthermore, the interaction of heavier hyperons is poorly known, i.e. ΞΞ or ΛΩ. Measurements in this field would allow also the theoreticians to provide better calculations of possible bound states.

The planned upgrade of the ALICE setup for high-luminosity Pb–Pb running [ALI12] would enable also searches for multi-strange baryon bound states via the invariant mass method as presented here for the H-Dibaryon and the Λn bound state. These searches for dibaryons like (ΛΞ) or (ΞΞ) are possible since they should be produced abundantly at LHC energies, see [ALI12]. It will be possible to study particles and anti-particles separately, which will give a significantly improved handle on the systematic errors. Should none of these predicted states be bound it is even more important to investigate the interaction among them, which would be measured via the ΛΞ- or ΞΞ correlations. First results on $p\Lambda$- and $\Lambda\overline{\Lambda}$-correlations have already been presented by ALICE [SZY12, SAF12].

Finally the baryon-baryon interaction is of crucial interest for the understanding of nuclei and hypernuclei and an interplay of experiment and theory is needed. ALICE is suitebale for providing a solid database for the theoretical modeling of the baryon-baryon interaction and will thus help to judge on the reliability of these models. A major role will be played by the ALICE group at GSI which started with this thesis in this area and is currently continued with the master thesis of J. Tscheuschner [TSC14] and the PhD thesis of N. Martin [MAR14].

Appendix A

Armenteros-Podolanski

This appendix describes the Armenteros-Podolanski space which is used in the previous discussed analyses to cut on the V0 particles.

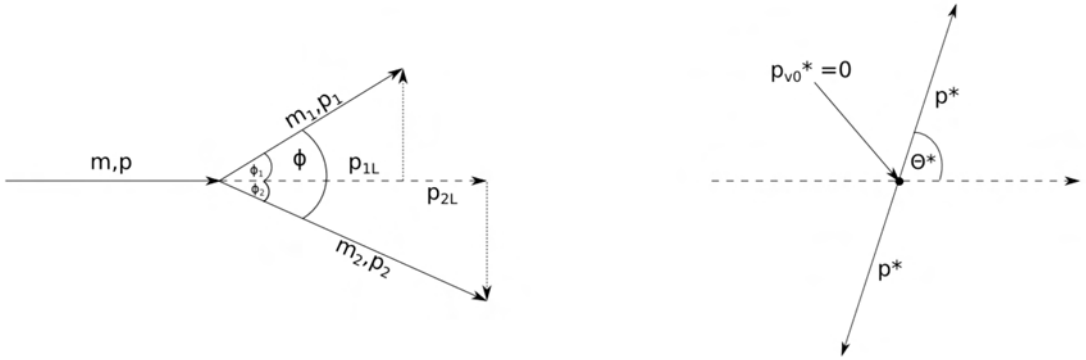

Figure A.1: Schematic decay of a V0 particle with mass m and momentum p into two daughters with masses m_1, m_2 and momenta p_1, p_2 in the laboratory frame (left) and the rest frame of the mother particle (right). Figure from [MAR11].

The Armenteros-Podolanski variables [ARM53] can be used to classify mother particles from V0 decays by identifying different decay topologies. The schematic Fig. A.1 shows the decay of a V0 particle with mass m and momentum p into two daughter particles with masses m_1, m_2 and momenta p_1, p_2, the index 1 always corresponds to the positively charged daughter and the index 2 to the negatively charged one. The left side of Fig. A.1 shows the decay kinematics in the laboratory frame and the right side shows the decay in the rest frame of the mother particle. The decay of the V0 particle can be symmetric or asymmetric. In the symmetric case the V0 particle decays into two particles with the same rest mass (e.g. K_s^0), whereas in the antisymmetric case one daughter particle has a higher rest mass than the other (e.g. Λ). The asymmetry can be quantified by a unitless number α, which relates the longitudinal momenta of the two daughter particles to the momentum of the V0 particle:

$$\alpha = \frac{p_{1_L} - p_{2_L}}{p_{1_L} + p_{2_L}}$$

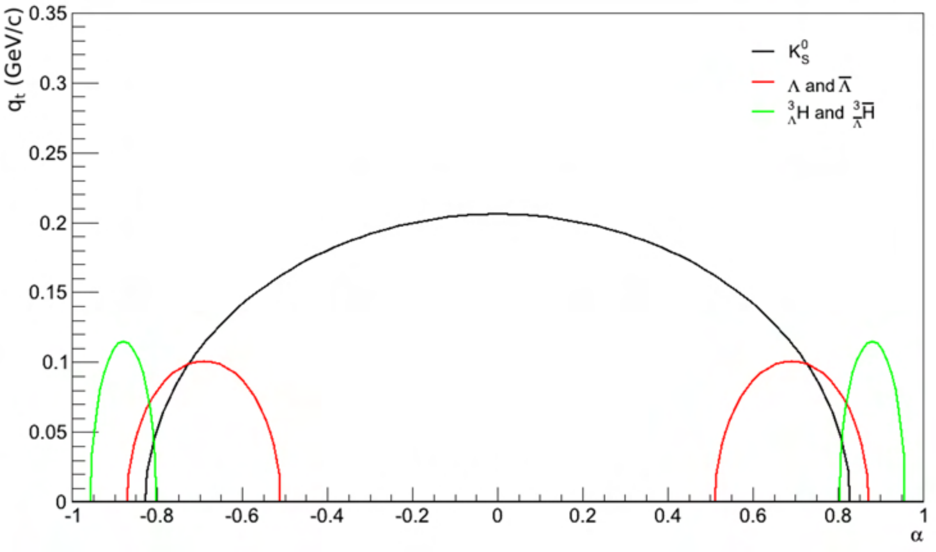

Figure A.2: Armenteros Podolanski ellipses for K_S^0 (black), Λ and anti-Λ (red) as well as for hypertriton and anti-hypertriton (green). The particles show up on the right side, which corresponds to positive asymmetries α, while the ellipsis for the anti-particles corresponding to negative asymmetries α show up on the left side. Figure from [MAR11].

while the longitudinal momenta are conserved: $p_L = p_{1_L} + p_{2_L} = p_1 \cos(\varphi_1) + p_2 \cos(\varphi_2)$. Since the velocity β of the V0 particle can not be measured directly, Armenteros and Podolanski introduced the quantity q_T , which is independent of β, but given by the momenta of the daughter particles

$$q_T = p_1 \sin(\varphi_1) = p_2 \sin(\varphi_2)\,.$$

If the variable q_T is plotted as a function of the asymmetry α, the different decay types are characterised by ellipses for $\beta \approx 1$ (ultra-relativistic case). In the ultra-relativistic case the ellipses are given by this expression:

$$\left(\frac{\alpha - \overline{\alpha}}{a}\right)^2 + \left(\frac{q_t}{p^*}\right) = 1\,,$$

with $\overline{\alpha} = \frac{E_1^* - E_2^*}{m_0}$, $p^* = (2m_0)\sqrt{m_0^4 + m_1^4 + m_2^4 - 2m_0^2 m_1^2 - 2m_0^2 m_1^2 - 2m_1^2 m_2^2}$ and $a = \frac{2p^*}{m_0}$.

Like this the center of the ellipsis is given by $(\overline{\alpha}, 0)$, whereas a corresponds to the half-axis in x-direction and p^* to the half-axis in y-direction. Figure A.2 shows the Armenteros-Podolanski ellipsis for K_s^0 in black, Λ and Anti-Λ in red as well as for hypertriton and anti-hypertriton in green. The particles show up on the right side, which corresponds to positive asymmetries α, while the ellipses for anti-particles corresponding to negative asymmetries α lie on the left side. For a rigorous deduction of formula refer to [ARM53].

Appendix B

$\Lambda(1520)$ branching ratio

The $\Lambda(1520)$ was not implemented in the standard Monte Carlo frameworks used at the LHC. Since we need to do the correction of the spectrum for acceptance and efficiency we decided to implement the particle in these tools.
To do this implementation correctly we checked the Particle Data Group entries on the $\Lambda(1520)$ which state:

$N\overline{K}$	$45 \pm 1\%$
$\Sigma\pi$	$42 \pm 1\%$
$\Lambda\pi\pi$	$10 \pm 1\%$
$\Sigma\pi\pi$	$0.9 \pm 0.1\%$
$\Lambda\gamma$	$0.85 \pm 0.15\%$

From this it is not clear how the fraction 45% of $N\overline{K}$ is split into $n\overline{K^0}$ and pK^-, where the first is not easy to detect with the current ALICE setup. Formerly experiments like NA49 and STAR used 22.5% for each of the $N\overline{K}$ decays.
A proper calculation has to include the isospin symmetry. We list here the relevant Clebsch-Gordan coefficients using the notation $\langle j_1, m_1, j_2, m_2 \,|\, J, M\rangle$:

$$\begin{array}{rl} \Lambda(1520) \to pK^- & \langle 1/2, 1/2, 1/2, -1/2 \,|\, 0,0\rangle = \sqrt{1/2} \\ \Lambda(1520) \to n\overline{K^0} & \langle 1/2, -1/2, 1/2, 1/2 \,|\, 0,0\rangle = -\sqrt{1/2} \end{array}$$

These values squared will give us the first approximation of the *BR* fractions to be assigned to the individual channels. Now there is a small difference caused by the phase space. For a two body decay with effective mass M_e we have

$$S_2 = \pi \cdot p_1 / M_e$$

where $p_1 = \sqrt{M_e^2 - (m_1 + m_2)^2} \cdot \sqrt{M_e^2 - (m_1 - m_2)^2} / M_e$.
This translates to $S_2(n\overline{K^0})/S_2(pK^-) \approx 97\%$ for the central value of the $\Lambda(1520)$ mass. From this we decided to keep the 22.5% used by the previous experiments.

Bibliography

[AAM08] K. Aamodt et al. (ALICE Collaboration), *The ALICE experiment at the CERN LHC*, JINST 3 (2008) S08002

[AAM11] K. Aamodt et al. (ALICE Collaboration), *Strange particle production in proton-proton collisions at $\sqrt{s} = 0.9\,TeV$ with ALICE at the LHC*, Eur. Phys. J. C 71 (2011) 1594

[AAM11a] K. Aamodt et al. (ALICE Collaboration), *Centrality Dependence of the Charged-Particle Multiplicity Density at Midrapidity in Pb–Pb Collisions at $\sqrt{s_{\mathrm{NN}}} = 2.76\,TeV$*, Phys. Rev. Lett. 106 (2011) 032301

[ABE05] B. L. Abelev et al. (STAR Collaboration), *Strange Baryon Resonance Production in $\sqrt{s}\mathrm{NN} = 200\,GeV$ p+p and Au+Au Collisions*, Phys. Rev. Lett. 97 (2005) 132301

[ABE07] B. Abelev et al. (STAR Collaboration), *Transverse momentum and centrality dependence of high-pt non-photonic electron suppression in Au+Au collisions at $\sqrt{s_{\mathrm{NN}}} = 200\,GeV$*, Phys. Rev. Lett. 98 (2007) 192301

[ABE10] B. I. Abelev *et al*. (STAR Collaboration), *Observation of an Antimatter Hypernucleus*, Science 328 (2010) 58

[ABE12a] B. Abelev et al. (ALICE Collaboration), *Centrality Dependence of Charged Particle Production at Large Transverse Momentum in Pb–Pb Collisions at $\sqrt{s_{\mathrm{NN}}} = 2.76$ TeV*, arXiv:1208.2711 (2012)

[ABE12b] B. Abelev et al. (ALICE Collaboration), *Suppression of high transverse momentum D mesons in central PbPb collisions at $\sqrt{s_{\mathrm{NN}}} = 2.76\,TeV$*, JHEP 09 (2012) 112

[ABE12c] B. Abelev et al. (ALICE Collaboration), *Multi-strange baryon production in pp collisions at $\sqrt{s} = 7\,TeV$ with ALICE*, Phys. Lett. B 712 (2012) 309

[ADA05] J. Adams et al. (STAR Collaboration), *Experimental and theoretical challenges in the search for the quark gluon plasma: the STAR collaborations critical assessment of the evidence from RHIC collisions*, Nucl. Phys. A 757 (2005) 102

[ADA11] A. Adare et al. (PHENIX Collaboration), *Heavy quark production in p + p and energy loss and ow of heavy quarks in Au+Au collisions at $\sqrt{s_{\mathrm{NN}}} = 200\,GeV$*, Phys. Rev. C 84 (2011) 044905

[ADC02] K. Adcox et al. (PHENIX Collaboration), *Suppression of Hadrons with Large Transverse Momentum in Central Au+Au Collisions at $\sqrt{s_{\mathrm{NN}}} = 130\,GeV$*, Phys. Rev. Lett. 88 (2002) 022301

[ADC05] K. Adcox et al. (PHENIX Collaboration), *Formation of dense partonic matter in relativistic nucleus-nucleus collisions at RHIC: experimental evaluation by the PHENIX collaboration*, Nucl. Phys. A 757 (2005) 184

[ADL06] S. Adler et al. (PHENIX Collaboration), *Nuclear modication of electron spectra and implications for heavy quark energy loss in Au+Au collisions at* $\sqrt{s_{\mathrm{NN}}} = 200\,GeV$, Phys. Rev. Lett. 96 (2006) 032301

[AGA11] H. Agakishiev et al. (STAR Collaboration), *Observation of the antimatter helium-4 nucleus*, Nature 473 (2011) 353

[AHN01] J. K. Ahn et al., *Doubly strange nuclei by a hybrid-emulsion experiment E373 at KEK*, AIP Conf. Proc. 594 (2001) 180

[AHN11] J. K. Ahn et al., *Letter of Intent*, KEK_J-PARC-PAC2011-03, (2011)

[AKA11] A. Kalweit for the ALICE Collaboration, *Particle identification in the ALICE experiment*, J. Phys. G: Nucl. Phys. 38 (2011) 124073

[AKA12] A. Kalweit, *Production of light flavor hadrons and anti-nuclei at the LHC*, Dissertation, Darmstadt (2012)

[ALI06] B. Alessandro et al. (ALICE Collaboration), *ALICE: Physics Performance Report, Volume II*, J. Phys. G: Nucl. Part. Phys. 32 (2006) 1295

[ALI12] K. Safarik and L. Musa (editors) (ALICE Collaboration), *Upgrade of the ALICE Experiment - Letter Of Intent* , CERN-LHCC-2012-012 / LHCC-I-022 (2012)

[ALIROOT] http://aliweb.cern.ch/Offline/AliRoot

[ALM10] J. Alme et al. (ALICE TPC Collaboration), *The ALICE TPC, a large 3-dimensional tracking device with fast readout for ultra-high multiplicity events*, Nucl. Intr. Meas. A 622 (2010) 316

[ALV86] R. F. Alvarez-Estrada et al., *Models of Hadron Structure based on Quantum Chromodynamics*, Springer, (1986)

[AND06] A. Andronic, P. Braun-Munzinger and J. Stachel, *Hadron production in central nucleus-nucleus collisions at chemical freeze-out*, Nucl. Phys. A 772 (2006) 167

[AND09] A. Andronic, F. Beutler, P. Braun-Munzinger, K. Redlich, J. Stachel, *Thermal description of hadron production in e+e- collisions revisited*, Phys. Lett. B 675 (2009) 312

[AND09a] A. Andronic, F. Beutler, P. Braun-Munzinger, K. Redlich, J. Stachel, *Statistical hadronization of heavy flavor quarks in elementary collisions: successes and failures*, Phys. Lett. B 678 (2009) 350

[AND11] A. Andronic, P. Braun-Munzinger, J. Stachel, H. Stöcker, *Production of light nuclei, hypernuclei and their antiparticles in relativistic nuclear collisions*, Phys. Lett. B 697 (2011) 203

[AND11a] A. Andronic, P. Braun-Munzinger, K. Redlich, J. Stachel, *The thermal model on the verge of the ultimate test: particle production in Pb–Pb collisions at the LHC* , J. Phys. G 38 (2011) 124081

[AND12] A. Andronic, P. Braun-Munzinger, K. Redlich, J. Stachel, *The statistical model in Pb-Pb collisions at the LHC*, arXiv:1210.7724 [nucl-th] (2012)

[AND12a] A. Andronic, private communication

[AOK91] S. Aoki et al. (KEK-E176 Collaboration),*Direct Observation of Sequential Weak Decay of a Double Hypernucleus*, Prog. Theor. Phys. 85 (1991) 1287

[AOK06] Y. Aoki et al., *The order of the quantum chromodynamics transition predicted by the standard model of particle physics*, Nature 443 (2006) 675

[ARM53] J. Podolanski and R. Armenteros, *Analysis of V-events*, Philosophical Magazine, 45 (1953) 13 1953

[ARM00] T. A. Armstrong et al., *Antideuteron yield at the AGS and coalescence implications*, Phys. Rev. Lett. 85 (2000) 2685

[ARM06] N. Armesto et al., *How sensitive are high-pt electron spectra at RHIC to heavy quark energy loss?*, Phys. Lett. B 637 (2006) 362

[ARM10] N. Armesto et al., *Constraint tting of experimental data with a jet quenching model embedded in a hydrodynamical bulk medium*, J. Phys. G 37 (2010) 025104

[ARS13] I. C. Arsene, private communication

[BAY85] G. Baym et al., *Is Cygnus X-3 strange?*, Phys. Lett. B 160 (1985) 181

[BIJ07] J. Bijnens, *Chiral perturbation theory beyond one loop*, Prog. Part. Nucl. Phys. 58 (2007) 521

[BJO82] J. D. Bjorken, *Energy Loss of Energetic Partons in Quark - Gluon Plasma: Possible Extinction of High p(t) Jets in Hadron - Hadron Collisions*, FERMILAB-PUB-82-059-THY, (1982)

[BLM11] C. Blume and C. Markert, *Strange hadron production in haevy ion collisions from SPS to RHIC*, Prog. Part. Nucl. Phys. 66 (2011) 834

[BOG68] P. N. Bogolioubov, *On a Model of quasiindependent quarks*, Ann. Inst. Henri Poincaré 8 (1968) 163

[BOT12] E. Botta, T. Bressani, G. Garbarino, *Strangeness nuclear physics: a critical review on selected topics*, Eur. Phys. J. A 48 (2012) 41

[BRE36] G. Breit and E. Wigner, *Capture of Slow Neutrons*, Phys. Rev. 49 (1936) 519

[BRO90] F. R. Brown et al., *On the Existence of a Phase Transition for QCD with Three Light Quarks*, Phys. Rev. Lett. 65 (1990) 2491

[BUB05] M. Buballa, *NJL-model analysis of dense quark matter*, Phys. Rep. 407 (2005) 205

[CAP75] N. Cabibbo and G. Parisi, *Exponential hadronic spectrum and quark liberation*, Phys. Lett. B 59 (1975) 67

[CAR12] T. F. Caramés and A. Valcarce, *Examination of the H dibaryon within a chiral constituent quark model*, Phys. Rev. C 85 (2012) 045202

[CHA12] S. Chatrchyan et al., *Suppression of non-prompt* J/ψ *, prompt* J/ψ*, and* $\Upsilon(1S)$ *in PbPb collisions at* $\sqrt{s_{\mathrm{NN}}} = 2.76\,TeV$, JHEP 05 (2012) 063

[CHI12] D. D. Chincellato, ALICE internal analysis note ANA-501, unpublished, (2012),

[CHO74] A. Chodos et al., *New extended model of hadrons*, Phys. Rev. D 9 (1974) 3471

[CHO74a] A. Chodos et al., *Baryon structure in the bag theory*, Phys. Rev. D 10 (1974) 2599

[CMS11] V. Khachatryan et al., *Strange Particle Production in pp Collisions at* $\sqrt{s} = 0.9$ *and 7 TeV*, JHEP 05 (2011) 064

[CLE11] J. Cleymans and D. Worku, *The Hagedorn temmperature Revisited*, Mod. Phys. Lett. A26 (2011) 1197

[COL75] J. C. Collins and M. J. Perry, *Superdense Matter: Neutrons or Asymptotically Free Quarks?*, Phys. Rev. Lett. 34 (1975) 1353

[CRA98] H. J Crawford, H-particle searches with heavy ions, Nucl. Phys. A 639 (1998) 417c

[CRE80] M. Creutz, *Monte Carlo study of quantized SU(2) gauge theory*, Phys. Rev. D 21 (1980) 2308

[DAN63] M. Danysz et al., *The identification of a double hyperfragment*, Nucl. Phys. 49 (1963) 121

[DEG76] T. DeGrand et al., *Masses and other parameters of the light hadrons*, Phys. Rev. D 12 (1976) 2060

[DÖN07] B. Dönigus, *Assembly And Tests Of The First Supermodule Of The ALICE Transition Radiation Detector*, Diplomarbeit, TU Darmstadt (2007)

[DÖN12] B. Dönigus for the ALICE Collaboration, *(Anti-)matter and hyper-matter production at the LHC with ALICE*, Nucl. Phys. A in press (2012)

[DOK01] Dokshitzer and Kharzeev, *Heavy quark colorimetry of QCD matter*, Phys. Lett. B 519 (2001) 199

[DON86] J. F. Donoghue, E. Golowich and B. R. Holstein, *Weak decays of the H dibaryon*, Phys. Rev. D 34 (1986) 3434

[DOV89] C. B. Dover, P. Koch and M. May, *Production of the H dibaryon in relativistic heavy-ion collisions*, Phys. Rev. C 40 (1989) 115

[DOV91] C. B. Dover, *Strange quarks in nuclei*, BNL-46322 (1991)

[DÜR08] S. Dürr et al., *Ab Initio Determination of Light Hadron Masses*, Science 322 (2008) 1224

[EMS09] D. Emschermann, *Construction and Performance of the ALICE Transition Radiation Detector*, Dissertation, Universität Heidelberg 2009

[ESW03] R. K. Ellis, W. J. Stirling, B. R. Webber, *QCD and Collider Physics*, Cambridge University Press (2003)

[EXH11] S. Cho et al. (ExHIC Collaboration), *Identifying Multiquark Hadrons from Heavy Ion Collisions*, Phys. Rev. Lett. 106 (2011) 212001

[EXP11] S. Cho et al. (ExHIC Collaboration), *Exotic hadrons in heavy ion collisions*, Phys. Rev. C 84 (2011) 064910

[FLUKA] http://www.fluka.org/fluka.php

[FRY56] W. F. Fry, J. Schneps and M. S. Swami, *Disintegration of Hyperfragments. II*, Phys. Rev. 101 (1956) 1526

[FUK11] K. Fukushima and T. Hatsuda, *The phase diagram of dense QCD*, Rep. Prog. Phys. 74 (2011) 014001

[GAL11] A. Gal and D. J. Millener, *Shell-model predictions for* $\Lambda\Lambda$ *hypernuclei*, Phys. Lett. B 701 (2011) 342

[GAL12] A. Gal and D. J. Millener, *Consistency of* $\Lambda\Lambda$ *hypernuclear events*, Hyperfine Interact. 210 (2012) 77

[GAL13] A. Gal, *Comment on recent Strangeness -2 predictions*, arXiv:1301.1241v1 [nucl-th] (2013)

[GEANT] R. Brun, F. Carminati and S. Giani, GEANT – detector description and simulation tool, CERNW5013 (1993)

[GEL64] M. Gell-Mann, *A Schematic model of baryons and mesons*, Phys. Lett. 8 (1964) 214

[GLA53] R. J. Glauber, *Cross Sections in Deuterium at High Energies*, Phys. Rev. 100 (1955) 242

[GOL86] E. Golowich, *Weak decays of the H dibaryon*, AIP Conf. Proc. 150 (1986) 952

[GOL92] E. Golowich and T. Sotirelis, $O(\alpha_s^2)$ *to the H dibaryon in a truncated bag model*, Phys. Rev. D 46 (1992) 354

[GRE99] C. Greiner und J. Schaffner, *Physics of Strange Matter*, in *Heavy Elements and Related New Phenomena*, Editors R.K. Gupta und W. Greiner, World Scientific Publications (1999), also arXiv:nucl-th/9801062

[GRO73] D. J. Gross, F. Wilczek, *Ultraviolet Behavior of Non-Abelian Gauge Theories*, Phys. Rev. Lett. 30 (1973) 1343

[GYU90] M. Gyulassy and M. Plümer, *Jet quenching in dense matter*, Phys. Lett. B 243 (1990) 432

[HAI07] J. Haidenbauer *etal.*, *The Hyperon-Nucleon Interaction: Conventional Versus Eective Field Theory Approach*, Lect. Notes Phys. 724 (2007) 113

[HAI10] J. Heidenbauer and U.-G. Meiner, *Predictions for the strangeness S =3 and 4 baryonbaryon interactions in chiral effective field theory*, Phys. Lett. B 684 (2010) 275

[HAI11] J. Heidenbauer and U.-G. Meiner, *To bind or not to bind: The H-dibaryon in light of chiral effective field theory*, Phys. Lett. B 706 (2011) 100

[HAI12] J. Haidenbauer and U.-G. Meißner, *Exotic bound states of two baryons in light of chiral effective field theory*, Nucl. Phys. A 881 (2012) 44

[HAI13] J. Haidenbauer, *Baryon-baryon interactions from chiral effective field theory*, arXiv:1301.1141v1 [nucl-th] (2013)

[HAG65] R. Hagedorn, Statistical Thermodynamics of Strong Interactions at High Energies, Suppl. Nuovo Cim. 3 (1965) 147

[HAL11] T. Inoue *et al.*, *Bound H-dibaryon in Flavor SU(3) Limit of Lattice QCD*, Phys. Rev. Lett. 106 (2011) 162002

[HAM00] S. Hamieh, K. Redlich, A. Tounsi, *Canonical description of strangeness enhancement from p–A to Pb–Pb collisions*, Phys. Lett. B 486 (2000) 61

[HEI04] U. W. Heinz, *Concepts of heavy ion physics*, CERN Yellow Report CERN-2004-001 (2004) 165

[HIJING] X.-N. Wang and M. Gyulassy, *HIJING: A Monte Carlo model for multiple jet production in pp, p A, and A A collisions*, Phys. Rev. D 44 (1991) 3501

[HOP50] V. D. Hopper and S. Biswas, *Evidence Concerning the Existence of the New Unstable Elementary Neutral Particle*, Phys. Rev. 80 (1950) 1099.

[HOT12] A. Bazavov et al. (HotQCD Collaboration), *Chiral and deconfinement aspects of the QCD transition*, Phys. Rev. D 85 (2012) 054503

[HUB10] S. Huber, *Ausrichtung des ALICE bergangsstrahlungsdetektors sowie Zweiteilcheninten-sittsinterferometrie identischer Pionen aus p+p Kollisionen bei LHC Energien von 900 GeV und 7 TeV*, Dissertation, TU Darmstadt (2010)

[HYP11] T. Saito *et al.* (HypHI Collaboration), *The first experimental results of HypHI*, invited talk presented at the NUFRA2011

[HYP12] T. Saito *et al.* (HypHI Collaboration), *Recent Results from the HypHI Project at GSI* invited talk presented at the Riken-BNL workshop 2012 conference

[INO12] T. Inoue, private communication

[IWA88] Y. Iwasaki, T. Yoshie, Y. Tsuboi, *The H Dibaryon in Lattice QCD*, Phys. Rev. Lett. 60 (1988) 1371

[JAF77] R. L. Jaffe, *Perhaps a Stable Dihyperon*, Phys. Rev. Lett. 38 (1977) 195 and erratum ibid. 38 (1977) 617

[JAM75] F. James and M. Roos, *Minuit: A System for Function Minimization and Analysis of the Parameter Errors and Correlations* Comput. Phys. Commun. 10 (1975) 343

[JAM80] F. James, *Interpretation of the shape of the likelihood function around its minimum*, Comput. Phys. Commun. 20 (1980) 29

[JSB00] J. Schaffner-Bielich, R. Mattiello and H. Sorge, *Dibaryons with Strangeness: Their Weak Nonleptonic Decay Using SU(3) Symmetry and How to Find Them in Relativistic Heavy-Ion Collisions*, Phys. Rev. Lett. 84 (2000) 4305

[JSB12] J. Schaffner-Bielich, private communication

[KAH96] D. E. Kahana et al., *Modeling cluster production at the BNL Alternating Gradient Synchrotron*, Phys. Rev. C 54 (1996) 338

[KMR86] P. Koch, B- Müller and J. Rafelski, *Strangeness in relativistic heavy ion collisions*, Phys. Rep. 142 (1986) 167

[KLE96] I. R. Klebanov and K. M. Westerberg, *Simple description of strange dibaryons in the Skyrme model*, Phys. Rev. D 53 (1996) 2804

[KLE07] E. Klempt and A. Zaitsev, *Glueballs, hybrids, multiquarks. Experimental facts versus QCD inspired concepts*, Phys. Rep. 454 (2007) 1

[KOC97] V. Koch, *Aspects of Chiral Symmetry*, Int. J. Mod. Phys. E 6 (1997) 203

[KOR01] A. A. Korsheninnikov *etal.*, *Superheavy Hydrogen* ^5H, Phys. Rev. Lett. 87 (2001) 092501

[KRI82] M. I. Krivoruchenko and M. G. Shchepkin, *Dilambda decays*, Sov. J. Nucl. Phys. 36 (1982) 769

[LEA12] R. Lea for the ALICE Collaboration, *Light Hypernuclei Production in PbPb Collisions at* $\sqrt{s_{\mathrm{NN}}} = 2.76$ *TeV with ALICE at LHC*, Act. Phys. Pol. B Proc. Supp. 5 (2012) 599

[LIU82] K. F. Liu and C. W. Wong, *MIT Bag Model with Center-of-Mass Correction*, Phys. Lett. B 113 (1982) 1

[LHC08] L. Evans and P. Bryant (Editors), *LHC Machine*, JINST 3 (2008) S08001

[MAR85] M. L. Marshak et al., *Evidence for Muon Production by Particles from Cygnus X-3*, Phys. Rev. Lett. 54 (1985) 2079

[MAR00] C. Markert, $\Lambda(1520)$*-Produktion in Proton-Proton- und zentralen Blei-Blei-Reaktionen bei 158 GeV pro Nukleon*, Dissertation, Frankfurt, 2000

[MAR03] C. Markert, G. Torrieri and J. Rafelski, *Strange hadron resonances: Freezeout probes in heavy ion collisions*, in H. T. Elze, E. Ferreira, T. Kodama, J. Letessier, J. Rafelski and R. L. Thews, *New states of matter in hadronic interactions. Proceedings, Pan-American Advanced Study Institute, PASI 2002*, Campos do Jordao, Sao Paulo, Brazil, January 7-18, 2002, AIP Conf. Proc. 631 (2003) 533

[MAR11] N. A. Martin, *Investigation of light (anti-)nuclei and (anti-)hypernuclei with ALICE at the LHC (CERN)*, Master Thesis, Darmstadt, (2011)

[MAR14] N. A. Martin, *Correlations of (multi-)strange baryons and search for hypothetical bound states with ALICE at the LHC*, Dissertation, Darmstadt, (2014) to be published

[MOS99] U. Mosel, *Fields, Symmetries, and Quarks*, Springer (1999)

[MÜL85] B. Müller, *The Physics of the Quark-Gluon Plasma*, Springer (1985)

[MUL83] P. J. Mulders and A. W. Thomas, *Pionic corrections and multi-quark bags*, J. Phys. G 9 (1983) 1159

[NAK10] K. Nakazawa (for KEK-E176, E373 and J-PARC E07 collaborators), *Double-*Λ *Hypernuclei via the* Ξ^- *Hyperon Capture at Rest Reaction in a Hybrid Emulsion*, Nucl. Phys. A 835 (2010) 207

[NAK10a] K. Nakazawa and H. Takahashi, *Experimental Study of Double- Hypernuclei with Nuclear Emulsion*, Prog. Theo. Phys. Suppl. 185 (2010) 335

[NAM60] Y. Nambu, *Axial Vector Current Conservation in Weak Interactions*, Phys. Rev. Lett. 4 (1960) 380

[NAR04] S. Narison, *QCD as a Theory of Hadrons*, Cambridge University Press (2004)

[NPL11] S. R. Beane *et al.* (NPLQCD Collaboration), *Evidence for a Bound H Dibaryon from Lattice QCD*, Phys. Rev. Lett. 106 (2011) 162001

[NPL12] S. R. Beane *et al.* (NPLQCD Collaboration), *Deuteron and exotic two-body bound states from lattice QCD*, Phys. Rev. D 85 (2012) 054511

[NPL12a] S. R. Beane *et al.* (NPLQCD Collaboration), *Light Nuclei and Hypernuclei from Quantum Chromodynamics in the Limit of SU(3) Flavor Symmetry*, arXiv:1206.5219v2 [hep-lat] (2012)

[NEY37] J. Neyman, *Outline of a Theory of Statistical Estimation Based on the Classical Theory of Probability*, Phil. Trans. Roy. Soc. London. A 236 (1937) 333

[PBM04] P. Braun-Munzinger, K. Redlich and J. Stachel, *Particle Production in Heavy Ion Collisions*, Invited Review, in: R. C. Hwa, X. N. Wang (Eds.), Quark Gluon Plasma Vol. 3, World Scientific Publishing, 2004

[PBM07] P. Braun-Munzinger and J. Stachel, *The quest for the quark–gluon plasma*, Nature 448 (2007) 302

[PBM09] P. Braun-Munzinger and J. Wambach, *Colloquium: Phase diagram of strongly interacting matter*, Rev. Mod. Phys. 81 (2009) 1031

[PDG12] J. Beringer et al. (Particle Data Group), *Review of Particle Physics*, Phys. Rev. D 86 (2012) 010001; http://pdg.lbl.gov/

[POL73] H. D. Politzer, *Reliable Perturbative Results for Strong Interactions?*, Phys. Rev. Lett. 30 (1973) 1346

[PRO66] D. J. Prowse, $_{\Lambda\Lambda}He^6$ *Double Hyperfragment*, Phys. Rev. Lett. 17 (1966) 782

[PSW04] P. Braun-Munzinger, J. Stachel and C. Wetterich, *Chemical freeze-out and the QCD phase transition temperature*, Phys. Lett. B 596 (2004) 61

[PYT06] T. Sjöstrand,a S. Mrenna and P. Skands, *PYTHIA 6.4 physics and manual*, JHEP 05 (2006) 026

[QUI83] C. Quigg, *Gauge Theories of the Strong, Weak, and Electromagnetic Interactions*, Benjamin Cummins (1983)

[RAF82] J. Rafelski and B. Müller, *Strangeness Production in the Quark-Gluon Plasma*, Phys. Rev. Lett. 48 (1982) 1066 and erratum: Phys. Rev. Lett. 56 (1986) 2334

[RAW00] R. Rapp and J. Wambach, *Chiral Symmetry Restoration and Dileptons in Relativistic Heavy-Ion Collisions*, Adv. Nucl. Phys. 25 (2000) 1

[RED02] K. Redlich and A. Tounsi, *Strangeness enhancement and energy dependence in heavy ion collisions*, Eur. Phys. J. C 24 (2002) 589

[ROB47] G. D. Rochester and C. C. Butler, *Evidence for the Existence of New Unstable Elementary Particles*, Nature 160 (1947) 855

[ROL01] W. A. Rolke and A. M. López, *Confidence intervals and upper bounds for small signals in the presence of background noise*, Nucl. Inst. Meth. A 458 (2001) 745

[ROL05] W. Rolke, A. Lopez, J. Conrad and F. James, *Limits and Confidence Intervals in presence of nuisance parameters*, Nucl. Instr. Meth. A 551 (2005) 493

[ROOT] http://root.cern.ch

[ROS86] J. L. Rosner, *SU(3) breaking and the H dibaryon*, Phys. Rev. D 33 (1986) 2043

[ROT05] H. J. Rothe, *Lattice Gauge Theories - An Introduction*, World Scientific Publishing (2005)

[SAF12] K. Safarik, plenary talk, QM2012 conference, Washington, D.C., Aug. 2012

[SAK00] T. Sakai, K. Shimizu and K. Yazaki, *H Dibaryon*, Prog. Th. Phys. Supp. 137 (2000) 121

[SAV12] M. J. Savage, *Nuclear physics from lattice QCD*, Prog. Part. Nucl. Phys. 67 (2012) 140

[SCH93] E. Schnedermann, J. Sollfrank and U. Heinz, *Thermal phenomenology of hadrons from 200-A/GeV S+S collisions* , Phys. Rev. C 48 (1993) 2462

[SCH99] R. Scheibl and U. W. Heinz, *Coalescence and flow in ultrarelativistic heavy ion collisions*, Phys. Rev. C 59 (1999) 1585

[SCH03] S. Scherer, Introduction to Chiral Perturbation Theory, Adv. Nucl. Phys. 27 (2003) 277

[SCH12] K. Schweda and J. Thome. Private communication.

[SCO94] N. N. Scoccola and G. L. Thomas, *Dibaryons as axially symmetric skyrmions*, Nucl. Phys. A 575 (1994) 623

[SHA11] P. E. Shanahan, A. W. Thomas, R. D. Young, *Mass of the H-dibaryon*, Phys. Rev. Lett. 107 (2011) 092004

[STE12] J. Steinheimer et al., *Hypernuclei, dibaryon and antinuclei production in high energy heavy ion collisions: Thermal production vs. Coalescence*, Phys. Lett. B 714 (2012) 85

[STO99] V. G. J. Stoks and Th. A. Rijken, *Soft-core baryon-baryon potentials for the complete baryon octet*, Phys. Rev. C 59 (1999) 3009

[SZY12] M. P. Szymański (for the ALICE Collaboration), *Meson and baryon femtoscopy in heavy-ion collisions at ALICE*, arXiv:1211.3288 [nucl-ex] (2012)

[TAK01] H. Takahashi et al., *Observation of a* ${}^{6}_{\Lambda\Lambda}$*He Double Hypernucleus*, Phys. Rev. Lett. 87 (2001) 212502

[TAK03] H. Takahashi et al., *Observation of double-hypernuclei and* Λ–Λ *interaction*, Nucl. Phys. A721 (2003) 951c

[THO71] G. ’t Hooft, *Renormalization of massless Yang-Mills fields*, Nucl. Phys. B 33 (1971) 173

[TOU03] A. Tounsi, A. Mischke and K. Redlich, *Canonical aspects of strangeness enhancement*, Nucl. Phys. A 715 (2003) 565c

[TSC14] J. Tscheuschner, *Feasibility study of multi-strange baryon correlation measurements with ALICE at the LHC*, Master Thesis, Darmstadt, (2014) work in progress

[WET03] I. Wetzorkea and F. Karsch, *The H dibaryon on the lattice*, Nucl.. Phys. B (Proc. Suppl.) 119 (2003) 278

[WIL74] K. G. Wilson, *Confinement of quarks*, Phys. Rev. D 10 (1974) 2445

[YAG05] K. Yagi, T. Hatsuda and Y. Miake, *Quark-Gluon Plasma*, Cambridge University Press (2005)

[YAM02] T. Yamazaki and Y. Akaishi, *(K^-,π^-) production of nuclear $\overline{K}$ bound states in proton-rich systems via $\Lambda^\star$ doorways*, Phys. Lett. B 535 (2002) 70

[YAM04] T. Yamazaki, A. Doté, Y. Akaishi, *Invariant-mass spectroscopy for condensed single- and double-$\overline{K}$ nuclear clusters to be formed as residues in relativistic heavy-ion collisions*, Phys. Lett. B 587 (2004) 167

[YND06] F. Ynduráin, *The Theory of Quark and Gluon Interactions*, Springer (2006)

[YOO07] C. J. Yoon et al. (KEK-PS E522 Collaboration), *Search for the H-dibaryon resonance in $^{12}C(K^-, K^+\Lambda\Lambda)$*, Phys. Rev. C 75 (2007) 022201(R)

ACKNOWLEDGMENTS

I would like to thank Prof. Dr. Peter Braun-Munzinger who always encouraged me and helped with the right words also in difficult times.
I also would like to thank Prof. Dr. J. Wambach who accepted being my Co-Referent.

Many thanks go to the ALICE GSI group who supported me in many useful discussions at very different levels. Namely Dr. Anton Andronic, Dr. Ralf Averbeck, Dr. Silvia Maschiocchi and Dr. Dariusz Miskowiec. I only mention some names but the whole group provided a solid ground to work from.

For the technical part of my work I would like to especially acknowledge people from Frankfurt, Heidelberg, Münster and CERN. Only highlighting two names here, both from Heidelberg: Dr. Venelin Angelov and Dr. Kai Schweda who helped in detailed questions in several matters.

Very special thanks go to Dr. Alexander Kalweit who helped in different ways. Especially coffee breaks with him generated a good atmosphere. I really miss those. Also special thanks to Nicole Martin for useful discussions.
Special thanks go also to Dr. Helmut Oeschler, who helped to focus on the necessary things when too much was pressing and many useful discussions.

I also have to acknowledge many good discussions with Prof. Dr. Jürgen Schaffner-Bielich who helped me to develop an overview on the whole hyper-matter field.

I have to thank the ALICE collaboration. Especially the conveners of the Physics Working Group I am connected with, namely Dr. Boris Hippolyte, Dr. Michele Floris, Prof. Dr. Christina Markert, Dr. Angela Badalà, Dr. Alberto Pulvirenti, Dr. Lee Stuart Barnby, Dr. Domenico Elia and Dr. Roberto Preghenella.

I would like to thank the Helmholtz Research School H-QM for providing an useful environment and the necessary money. Special thanks here go to Prof. Dr. Henner Büsching for his support and encouraging me.
Connected to this I would like to thank Prof. Dr. Bengt Friman for his patience in my PhD commitee as long as we discussed technical issues and for his support and questions in the analysis part.

I also would like to thank our secretary Sandra Schecker, who helped me with all the bureaucratic parts connected to my work. Also the women of H-QM and HGS-HIRe have to be noticed here.

This work has been supported by EMMI, GSI, BMBF (Forschungschwerpunkt FSP 201) and H-QM which carried the costs of my travels. I especially acknowledge H-QM for providing the scholarship for my studies and EMMI for jumping in for the final two months. This work was supported by the Helmholtz Alliance Program of the Helmholtz Association, contract HA216/EMMI ”Extremes of Density and Temperature: Cosmic Matter in the Laboratory”.

I am also very grateful to the (proof-)readers and commenters who helped to minimise mistakes of different kinds: Anton, Antonin, Alex, Caro, Christian, Jan, Kai, Nicole, Ralf and Steffen!

Last but not least I would like to thank my parents who provided me the chance to this. Even if one of you passed away while this work was ongoing, it would not have been possible without you anyway! And finally I have to still thank my fiancée Caroline for her trust, for believing in me and surviving this long journey together with me.

ERKLÄRUNG ZUR DISSERTATION

(gemäss §9 Abs. 1 der allgemeinen Promotionsordnung)

Hiermit versichere ich, die vorliegende Dissertation ohne Hilfe Dritter nur mit den angegebenen Quellen und Hilfsmitteln angefertigt zu haben. Alle Stellen, die aus den Quellen entnommen wurden, sind als solche kenntlich gemacht worden. Diese Arbeit hat in gleicher Form noch keiner Prüfungsbehörde vorgelegen.

Babenhausen, 22. Januar 2013

(Benjamin Dönigus)

DECLARATION OF PERSONAL PROPERTY

This work utilises ALICE data and the analyses have been carried out within the ALICE Collaboration, but only the figures carrying the ALICE logo and a label (ALICE performance or ALICE preliminary) are official ALICE results. All other figures, not taken from articles, are the personal property of the author.

Curriculum vitae

Contact information:

Name:	Benjamin Dönigus
Date of birth:	August 2, 1979
Martial status:	Engaged (with Caroline Kühnle)

Education:

2007 - today	PhD Student at Technical University of Darmstadt (Physics Department) working at GSI Helmholtzzentrum für Schwerionenforschung GmbH and Helmholtz Research School H-QM Working title of the PhD Thesis: Investigation Of Baryons With Strangeness And Search For Weakly Decaying Exotics At The LHC
2000 - 2007	Technical University of Darmstadt (Physics Department) Diploma Thesis: Assembly and tests of the first supermodule of the ALICE transition radiation detector (TRD)
1997 - 2000	Occupational grammar school (Landrat-Gruber-Schule Dieburg) Baccalaureate
1990 - 1997	Comprehensive school (Joachim-Schumann-Schule Babenhausen)
1986 - 1990	Primary school (Markwaldschule Langstadt)

Teaching Experience:

2007 – 2011	Co-Supervision of three students on ALICE TRD electronics
2007 – 2009	Co-Supervision of three students on ALICE TRD pre-trigger development and commissioning
2002 – 2006	Tutor for practical exercises in experimental physics at TU Darmstadt
2005 – 2006	Tutor for exercises in solid state physics (Solid state physics I + II) at TU Darmstadt

Membership in Professional Societies:

Deutsche Physikalische Gesellschaft, Gesellschaft Deutscher Chemiker

Research interests:

Production of resonances and search for exotica in pp and Pb-Pb collisions at the LHC
Measurement of and triggering on light nuclei in pp and Pb-Pb collisions
Production of open and hidden charm and beauty in high-energy collisions
Detector development and construction of the ALICE TRD
Detector control system for the TRD

Publications:

51 publications signed as member of the ALICE Collaboration, therefore only publications are shown with a significant contribution:

B. Dönigus (for the ALICE collaboration), (Anti-)matter and hyper-matter production at the LHC with ALICE, to appear in Nucl. Phys. A
J. Lehnert et al., Status of the Pretrigger System for the ALICE Transition Radiation Detector, GSI Report 2010-1, 341
B. Dönigus (for the ALICE collaboration), Heavy flavour capabilities of the ALICE transition radiation detector, Prog. Part. Nucl. Phys. 62 (2009) 323
B. Dönigus et al., The Pretrigger System for the Transition Radiation Detector in ALICE, GSI Report 2008-1, 240
K. Oyama et al., Installation and Commissioning of the Transition Radiation Detector for ALICE, GSI Report 2008-1, 238
C.Adler et al., Construction of the First ALICE TRD Super Module, GSI Report 2007-1, 236

Contributions at international conferences and workshops:

B. Dönigus for the ALICE collaboration, (Anti-)matter and hyper-matter production at the LHC with ALICE, Talk at the Quark Matter Conference, 2012, Washington D.C.
B. Dönigus for the ALICE collaboration, Resonance production and search for exotica with ALICE at the LHC, Talk at the Workshop On Hyperon-Hyperon Interactions and Searches for Exotic Di-Hyperons in Nuclear Collisions, 2012, BNL
B. Dönigus and A. Karasu Uysal for the ALICE collaboration, Measurement of Baryonic Resonances in pp Collisions at the LHC with ALICE, Poster at Quark Matter 2011, Annecy
B. Dönigus for the ALICE collaboration, Heavy flavour capabilities with the ALICE TRD, Talk at the International School of Nuclear Physics 2008, Erice
B. Dönigus & Silvia Masciocchi for the ALICE collaboration, Feasibility study of heavy baryon measurements with the ALICE detector at the LHC, Poster at the 417th WE-Heraeus Seminar “Characterization of the Quark-Gluon Plasma with Heavy Quarks” 2008, Bad Honnef

Contributions at national conferences and workshops

B. Dönigus for the ALICE collaboration, Measurement Of The Baryonic Λ(1520) Resonance With The ALICE Apparatus At The LHC, Talk at the DPG Frühjahrstagung 2012, Mainz
B. Dönigus for the ALICE collaboration, Resonance production and search for exotica with ALICE at the LHC, Talk at the XLIII. Arbeitstreffen Kernphysik Schleching 2012, Schleching
R. Romita, B. Dönigus and R. Grajcarek for the ALICE collaboration, Reconstruction of open charm hadrons with the ALICE experiment at the LHC, Talk at the DPG Frühjahrstagung 2010, Bonn

Computing skills

Unix/Linux, Windows, Mac OS, Bash-Shell, Perl, C++, ROOT, AliRoot, Geant3, PYTHIA, Hijing, Oracle, MySQL

Languages:

German: Native (both spoken and written)
English: Fluent (both spoken and written)